Helsinki University of Technology
Dissertations in Computer and Information Science
Espoo 2006 Report D17

Compaction of C-Band Synthetic Aperture Radar Based Sea Ice Information for Navigation in the Baltic Sea

Juha Karvonen

Dissertation for the degree of Doctor of Science in Technology to be presented with due permission of the Department of Computer Science and Engineering for public examination and debate in Auditorium T2 at Helsinki University of Technology (Espoo, Finland) on the 8th of December, 2006, at 12 o'clock noon.

Helsinki University of Technology
Department of Computer Science and Engineering
Laboratory of Computer and Information Science
P.O.Box 5400
FIN-02015 HUT
FINLAND

Distribution:
Helsinki University of Technology
Laboratory of Computer and Information Science
P.O.Box 5400
FIN-02015 HUT
FINLAND
Tel. +358-9-451 3272
Fax +358-9-451 3277
http://www.cis.hut.fi

Available in pdf format at http://lib.hut.fi/Diss/2006/isbn9512284723/

ISBN-13 978-951-22-8471-9 (printed version)
ISBN-10 951-22-8471-5 (printed version)
ISBN-13 978-951-22-8472-6 (electronic version)
ISBN-10 951-22-8472-3 (electronic version)
ISSN 1459-7020

Otamedia Oy
Espoo 2006

Karvonen, J. (2006): **Compaction of C-Band Synthetic Aperture Radar Based Sea Ice Information for Navigation in the Baltic Sea**. Doctoral thesis, Helsinki University of Technology, Dissertations in Computer and Information Science, Report D17, Espoo, Finland.

Keywords: synthetic aperture radar, SAR, sea ice, classification, pulse-coupled neural network, PCNN, wavelets, image compression, independent component analysis.

ABSTRACT

In this work operational sea ice synthetic aperture radar (SAR) data products were improved and developed. A SAR instrument is transmitting electromagnetic radiation at certain wavelengths and measures the radiation which is scattered back towards the instrument from the target, in our case sea and sea ice. The measured backscattering is converted to an image describing the target area through complex signal processing. The images, however, differ from optical images, i.e. photographs, and their visual interpretation is not straightforward. The main idea in this work has been to deliver the essential SAR-based sea ice information to end-users (typically on ships) in a compact and user-friendly format. The operational systems at Finnish Institute of Marine Research (FIMR) are currently based on the data received from a Canadian SAR-satellite, Radarsat-1.

The operational sea ice classification, developed by the author with colleagues, has been further developed. One problem with the SAR data is typically that the backscattering varies depending on the incidence angle. The incidence angle is the angle in which the transmitted electromagnetic wave meets the target surface and it varies within each SAR image and between different SAR images depending on the measuring geometry. To improve this situation, an incidence angle correction algorithm to normalize the backscattering over the SAR incidence angle range for Baltic Sea ice has been developed as part of this work. The algorithm is based on SAR backscattering statistics over the Baltic Sea.

To locate different sea ice areas in SAR images, a SAR segmentation algorithm based on pulse-coupled neural networks has been developed and tested. The parameters have been tuned suitable for the operational data in use at FIMR. The sea ice classification is based on this segmentation and the classification is segment-wise rather than pixel-wise.

To improve SAR-based distinguishing between sea ice and open water an open water detection algorithm based on segmentation and local autocorrelation has been developed. Also ice type classification based on higher-order statistics and independent component analysis have been studied to get an improved SAR-based ice type classification.

A compression algorithm for compressing sea ice SAR data for visual use has

been developed. This algorithm is based on the wavelet decomposition, zero-tree structure and arithmetic coding. Also some properties of the human visual system were utilized. This algorithm was developed to produce smaller compressed SAR images, with a reasonable visual quality. The transmission of the compressed images to ships with low-speed data connections in reasonable time is then possible.

One of the navigationally most important sea ice parameters is the ice thickness. SAR-based ice thickness estimation has been developed and evaluated as part of this work. This ice thickness estimation method uses the ice thickness history derived from digitized ice charts, made daily at the Finnish Ice Service, as its input, and updates this chart based on the novel SAR data. The result is an ice thickness chart representing the ice situation at the SAR acquisition time in higher resolution than in the manually made ice thickness charts. For the evaluation of the results a helicopter-borne ice thickness measuring instrument, based on electromagnetic induction and laser altimeter, was used.

PREFACE

This work has been performed at the Finnish Institute of Marine Research (FIMR) during the years 2000–2005. I want to thank FIMR for an interesting research field, and especially Markku Similä and Prof. Jouko Launiainen for their support and collaboration. Also thanks to Istvan Heiler from FIMR, Jouni Vainio, Ari Seinä, Hannu Grönvall, Simo Kalliosaari and Patrick Eriksson from the Finnish Ice Service (FIS). The good co-operation with FIS has made this work possible. Also thanks to all the people somehow involved to these sea ice studies at the HUT laboratory of space technology and at the Technical Research Centre of Finland (VTT) for their co-operation in our joint sea ice projects, especially to Marko Mäkynen (HUT), Prof. Martti Hallikainen (HUT), Robin Berglund (VTT), Ville Kotovirta (VTT). And also thanks to the FINSTASHIP ice breaker staff who has been involved in this research as test users.

I would like to thank the supervisor of my thesis, Prof. Erkki Oja and Doc. Jorma Laaksonen, the instructor of my work, for their execellent guidance. I also thank the pre-examiners Dr. Markku Hauta-Kasari (InFotonics Center, Joensuu, Finland) and Prof. Matti Leppäranta (University of Helsinki, Finland) work and their constructive comments on my manuscript. And many thanks to prof. Torbjørn Eltoft from the University of Tromsø, Norway, for agreeing to be my opponent.

And many thanks to Eila Aronen, my parents Sirkku and Kauko, for their support, and also to my aunt Rauha Karvonen for her support.

Helsinki, November 7th, 2006.

Juha Karvonen

Contents

List of Abbreviations and Acronyms

ALOS Advanced Land Observing Satellite

ALP Adaptive Laplacian Pyramid, an image compression technique

ANSI American National Standards Institute, an organization that administers and coordinates the U.S. voluntary standardization and conformity assessment system

ASAR Advanced Synthetic Aperture Radar, the SAR instrument of the Envisat satellite

ASCII American Standards Committee for Information Interchange, a standard for coding characters

AVHRR Advanced Very High Resolution Radiometer, a space–borne remote sensing instrument of NOAA

CCRS Canada Centre for Remote Sensing

CGI Common Gateway Interface

CI Consolidated Ice, concentration 90–100 %

CLI Close Ice, concentration 70–80 %

CQF Conjugate Quadrature Filter

CR Compression Ratio

DCRS Danish Centre for Remote Sensing

DEM Digital Elevation Model

EM Expectation-Maximization algorithm

ENL Equivalent Number of Looks

Envisat ENVIronment SATellite of ESA, carrying many instruments also the ASAR

ERS European Remote Sensing Satellite, the currently operating satellite with a SAR instrument is ERS-2, successor of ERS-1

ESA European Space Agency

EOS End Of Sequence

FBI Frozen Brash Ice

FI Fast Ice

FIMR Finnish Institute of Marine Research

FINSTASHIP A state owned shipping company (e.g. ice breakers are owned

by Finstaship)

FIR Finite Impulse Response digital filter

FIS Finnish Ice Service, an operational part of FIMR

FMA Finnish Maritime Administration

FTP File Transfer Protocol, an Internet protocol for file transfer

FYI First Year Ice, ice developed during the same year, Baltic Sea ice is all FYI

GLCM Gray Level Co-occurrence Matrix, a matrix computed to describe the local image texture

GSM Global System for Mobile Communications, originally Groupe Special Mobile which was changed to Global System for Mobile Communications later

HDI Highly Deformed Ice

HEM Helicopter-borne Electromagnetic Induction, an instrument for measuring sea ice thickness based on electromagnetic induction, operated from helicopter

HH Horizontal-Horizontal, the instrument is transmitting horizontally polarized radiation and receiving horizontally polarized radiation

HUT Helsinki University of Technology

HUTSCAT Helsinki University of Technology Scatterometer. A device developed at HUT LST

HV Horizontal-Vertical, see HH

HVS Human Visual System

IC Independent Component

ICA Independent Component Analysis

ICM Iterated conditional Modes algorithm

IEEE Institute of Electrical and Electronics Engineers

IEM Integral Equation Model, a (SAR) backscattering model

IGARSS IEEE International Geoscience and Remote Sensing Symposium, an annual symposium

JERS Japanese Remote Sensing Satellite

JPEG Joint Photographic Experts Group (development group for lossy image compression also a file extension) image compression standard

JPEG-2000 A wavelet-based updated version of JPEG standard

KNN K Nearest Neighbors algorithm

KSAT Kongsberg Satellite Services AS, A company in Tromsø, Norway, receiving and processing satellite-borne remote sensing instrument data, earlier known as Tromsø Satellite Station (TSS)

LBI Loose Brash Ice

LI Level Ice, contains both SLI and RLI

LST Laboratory of Space Technology at HUT

LVQ Learning Vector Quantization, a training algorithm for vector quantization

MCMC Markov Chain Monte Carlo

MODIS Moderate Resolution Imaging Spectroradiometer, a space-borne remote sensing instrument of NASA. The instrument has 36 frequency bands ranging from optical to infrared bands. The instrument has been mounted on two satellites, Aqua and Terra

MRF Markov Random Field

MYI Multi-Year Ice, ice developed during more than two years, sometimes also division to only FYI and MYI can be seen, and SYI is then included in MYI

NASA National (USA) Aeronautics and Space Administration

NI Nilas Ice

NMT Nordic Mobile Telephone, a cell phone system formerly in use in Scandinavia, NMT-450 operated at the frequency of 450 MHz and NMT-900 at the frequency 900 MHz

NOAA National (USA) Oceanic and Atmospheric Administration

NRT Near-Real-Time

OI Open Ice, concentration 40–60 %

PDF Probability Density Function

PC Principal Component

PCA Principal Component Analysis

PCNN Pulse coupled Neural Network

PE Processing Element, a single processing element in an artificial neural network (e.g. PCNN) corresponding to a neuron in a biological neural network

PBM see PNM

PGM see PNM

PNM Netpbm superformat, a portable image file format, includes portable bit map (PBM) for monochrome images, portable gray map (PGM) for gray tone images and portable pixmap (PPM) for color images

PPM see PNM

POT Physical Optics Theory, a (SAR) backscattering model

PRF Pulse Repetition Frequency

PSNR Peak Signal to Noise Ratio

Radarsat A Canadian SAR-equipped satellite, Radarsat-1 has been orbiting since 1995 and Radarsat-2 will be launched in 2006 or 2007

RCS Radar Cross Section

RLI Rough Level Ice

RMS Relative Mean Square

SAR Synthetic Aperture Radar, an imaging radar instrument

SEM Stochastic Expectation-Maximization algorithm

SFT Smart File Transfer, a reliable mobile file transfer technology developed at VTT

SIR-C/X-SAR Spaceborne Imaging Radar-C / X-Band Synthetic Aperture Radar

SLI Smooth Level Ice

SNN Symmetric Nearest Neighborhood filter

SNR Signal to Noise Ratio

SMHI Swedish Meteorological and Hydrological Institute

SNA Radarsat-1 ScanSAR narrow mode A, refers to an imaging mode of Radarsat-1

SNB Radarsat-1 ScanSAR narrow mode B, refers to an imaging mode of Radarsat-1

SPM Small Perturbation Model, a (SAR) backscattering model, for small surface roughness

SRTM Shuttle Radar Topography Mission

SSM/I Special Sensor Microwave/Imager, a space-borne remote sensing instrument

SWA Radarsat-1 ScanSAR wide mode A, refers to an imaging mode of Radarsat-1

SWB Radarsat-1 ScanSAR wide mode B, refers to an imaging mode of Radarsat-1

SYI Second Year Ice, ice which has developed during two years

TGARS Transactions on Geoscience and Remote Sensing, an monthly IEEE publication

VH Vertical-Horizontal, see HH

VOI Very open ice, concentration 10–30 %

VTT Technical Research Centre of Finland (Valtion Teknillinen Tutkimuskeskus in Finnish)

VV Vertical-Vertical, see HH

WGS-84 World Geodetic System 1984, an earth-fixed global reference frame including a set of earth-related parameters, e.g. shape of an earth ellipsoid and the earth mass

List of Symbols

$\#$ number (count)
$\hat{\alpha}$ estimate of α
α_i scaling coefficient (with subindex i)
α_A absorption constant (of a media)
α_D PCNN decay constant
α_I intensity factor, in ICA-based classification of textures
β (arbitrary) angle
β PCNN linking parameter
$\beta_{\min}$ PCNN linking parameter
γ radar incidence (measurement) angle (local)
Δ difference, e.g. Δt is time difference
Δ_q quantization step increment
δ_p penetration depth
ϵ dielectric coefficient
ϵ' permittivity
ϵ'' dielectric loss
ϵ_r relative (to vacuum) dielectric coefficient
θ phase
θ_E longitude
Θ parameter vector
κ diffusion function (in anisotropic diffusion filtering) adjusting parameter
Λ diagonal matrix
Λ_B Bragg scattering wavelength
λ wavelength
λ_k kth eigenvalue of a matrix, λ_1 is the largest (1st) eigenvalue and so on
μ mean
ρ, ρ_k relative edge densities (processed image value divided by the original image value). Index values (k) refer to different types of edges.
ρ_r reflection coefficient in the interface of two media
Σ sum operator
σ standard deviation
σ^0 radar backscattering coefficient

σ^2 variance
σ_D standard deviation of a wavelet decomposition detail image
σ_{R} radar cross section (RCS)
$\sigma_{\mathrm{between}}$ variance of class means
σ_{within} sum of class variances
σ_{rel} relative standard deviation (std) i.e local std divided by global std
ϕ_E latitude
ϕ_{ref} reference latitude
$\phi(t)$ wavelet scaling function
Φ flow (from neighborhood in anisotropic diffusion)
Π product operator
Π_k likelihood function with subindex k
A area (unit area)
A basis vector matrix
A_{SAR} (SAR) amplitude
a, b factor (parameter) values, used in many context
a_e, b_e ellipse and ellipsoid major axis lengths
a_q quantized wavelet transform approximation image value
B_l basis value in a logarithmic transform
B ICA mapping matrix, matrix consisting of the ICA basis vectors
b_i i:th basis vector
C signal autocorrelation
C_w local wavelet coefficient strength
c wavelet coefficient value
c_j jth clique (in MRF)
$c_k(x, y, t)$ diffusion function (in anisotropic diffusion filtering)
D quantization interval
$D_E(x, y)$ Euclidean distance between vectors x and y
dR_I HVS response to intensity stimulus change
E Entropy
$E[x]$ Expectation operation applied to random variable x
e base of the natural logarithm (Napier's constant)
e_e ellipse (or ellipsoid) eccentricity
$F(x)$ Feature vector computation operator for data set x
$F_{ij}[n]$ feeding output of a PCNN PE (neuron) at pixel location (row,column)=(i, j) and at time step (iteration) n (starting from zero)
f frequency
f_F frequency factor
f_I (SAR) intensity factor
f_T texture factor
f_a factor in PCNN threshold adjusting
f_e focal length for ellipse (ellipsoid)
f_j potential function (in MRF)

f_s, f_i scaling factor (with an integer subindex i)
$\hat{f}_k$ estimate of a PDF f_k
G gain, gain factor
G_A antenna gain
g derivative function of a non-quadratic function
g_0, g_1 high-pass FIR filters
H differential entropy
h smoothing parameter
h_{keel} ice ridge keel height
h_s satellite height from earth surface (perpendicular)
h_{sail} ice ridge sail height
h_r satellite height from the satellite (SAR) measurement on earth surface
h_0, h_1 low-pass FIR filters
I intensity
I_c processed (compressed) image intensity
$I_{\max}$ maximum intensity
I_o original image intensity
I_{SAR} (SAR) intensity
i imaginary unit
K_G Gaussian kernel used in PDF estimation
L PCNN linking
$L_{A_{\min}}$ PCNN linking at minimum of set A
$L_{B_{\max}}$ PCNN linking at maximum of set B
L_c correlation length
$L_{\text{ij}}[n]$ linking output of a PCNN PE (neuron) at pixel location (row,column)=(i,j) and at time step (iteration) n (starting from zero)
l distance, length
M_3 skewness (normalized third moment)
M_4 kurtosis (normalized fourth moment)
m_k kth moment
N total number (count) of elements in a set
N_B number of bits
N_c number of classes
N_{levels} number of wavelet decomposition (resolution) levels
$N_{\min}$, $N_{\max}$ define the allowed interval of quantization steps i.e. minimum number of steps and maximum number of steps
N_q number of quantization steps
N_S number of symbols in a sequence
N_{sc} number of significant wavelet coefficients
n noise, or speckle term
P power
$P(x)$ cumulative PDF of x
p probability density function (PDF), probability

p_i probability of event i

$\hat{p}_k$ estimate of prior probability p_k

P_r received power

P_t transmitted power

q_0 quantization parameter

$r, r_1, r_2, ...$ criterion functions

R distance, radius

R^2 coefficient of determination

R_{ref} earth radius at reference latitude

r_i criterion values used in vector selection, i is an integer index

$r(x)$ Bayes classification criterion for a data set x

$s_{\mathrm{k,l}}$ state of pixel at location (k,l)

S quantization step

S_d quantization step closest to the minimum in an uneven quantization scheme

$S_i(x, b_i)$ Similarity measure between vectors x and b_i

$S_{\mathrm{k,l}}$ set of states in the neighborhood of pixel at location (k,l)

T, T_k threshold, k is a subindex (can be either number or letter)

T_{hi} higher (autocorrelation) threshold used in open water detection

$T_{\mathrm{ij}}[n]$ threshold value of a PCNN PE (neuron) at pixel location (row,column)=(i, j) and at time step (iteration) n (starting from zero)

T_{ice} ice thickness

T_{lo} lower (autocorrelation) threshold used in open water detection

T_m threshold value for class with index m (between classes with indices m and $m-1$)

T_{max} maximum ice thickness over an area

T_{mean} mean ice thickness over an area

T_{min} minimum ice thickness over an area

t time

$U_{ij}[n]$ internal activity of a PCNN PE (neuron) at pixel location (row,column)=(i, j) and at time step (iteration) n (starting from zero)

v_{br} fraction of brine volume (between 0 and 1)

$W(t)$ wavelet function

w weight matrix or weight value, also indexed versions e.g. w_{ij} can appear in the text

x, y, z 3-D Cartesian coordinates

x_m, y_m Mercator projection easting and northing coordinates (in meters)

Z_s scaling factor (in MRF)

$\mathrm{Y_{ij}}[n]$ binary output of a PCNN PE (neuron) at pixel location (row,column)=(i, j) and at time step (iteration) n (starting from zero)

Chapter 1

Introduction

1.1 Overview

About 90 % of the Finnish export and 70 % of the import is transported by sea [40]. Because of this and the fact that all the Finnish harbors are ice-surrounded for several months during a usual ice winter, navigation in the Baltic Sea ice is very important. Ice breakers and other ships need to be aided and remote sensing data can be used for this purpose. Synthetic aperture radar (SAR) data plays an important role in the winter navigation in the Baltic Sea. SAR data over the sea can be acquired also during dark hours and through cloud cover, which are obvious advantages compared to conventional optical and infrared frequency passive instruments. Finnish Ice Service (FIS) is an operative part of Finnish Institute of Marine Research (FIMR), and the role of FIS is to produce and deliver sea ice information products to the end-users in the Baltic Sea.

Due to the limited bandwidths to the ships, data compression to transmit the original SAR data is necessary. Because expertise is required to correctly interpret SAR data, automated interpretation of the SAR data has been developed to make the data more user-friendly for operational use in the Baltic Sea area. The term *compaction* in this thesis' context stands for compressing the data, without losing any or losing only a little of the important sea ice information. In the extreme, compaction means producing an interpreted data product, which is more user-friendly and as a byproduct also the data size is reduced. This reduction is due to ignoring the navigationally useless information. The aim is also that the end-user will get the data in a compact and useful format. The main ideas of SAR data compaction are presented for Radarsat-1 ScanSAR narrow and ScanSAR wide mode data, which are the main operational SAR data types at FIMR. Radarsat-1 is a Canadian space-borne SAR instrument [1] used by FIMR for operational remote sensing of the Baltic Sea.

In this work, three SAR-based sea ice products, i.e. sea ice information combined to its geological location, have been developed. First the existing sea ice classification [108] has been further developed. Second a compression algorithm for compress-

ing sea ice SAR data has been developed. Third a new sea ice product, SAR ice thickness estimation, has been developed. The products (compressed original SAR images, ice thickness charts, ice classifications) are typically delivered to end-users as thematic maps, which can be viewed in their navigation and information systems on-board. The SAR compression algorithm was developed to address the requirement of an efficient data compression to make it possible to deliver SAR data in high resolution to end-users.

1.2 Goals and Contributions of the Work

Sea ice classifications based on Radarsat-1 SAR data have been delivered operationally since 1998 by the Finnish Ice Service. The algorithms were developed and the system was implemented at FIMR [108]. However, the first version of the operational system only produced ice type classification. In most cases the classification could distinguish between navigationally easy areas (open water or thin ice) and navigationally difficult areas (deformed ice, fast ice), but it still had several drawbacks. The goal of this work has been to improve the operational sea ice SAR products and develop new useful products for winter navigation purposes in the Baltic Sea. The main objective has been to produce and deliver sea ice information in compact and informative form to the end-users, and to produce and deliver this information automatically with a minimum delay after a SAR image has been received. Scientific contributions of this work can be summarized as follows:

1. The operational sea ice SAR classification system, developed at FIMR by the author with colleagues, has been updated using the methods developed and tested in this work.

2. A new sea ice product, the SAR-refined ice thickness chart, has been developed.

3. For SAR image preprocessing an iterative incidence angle correction algorithm has been developed. This is a necessary step before classifying typical operational SAR scenes with a relatively large incidence angle range.

4. Compression of SAR data has been developed significantly from the earlier and has been integrated in the user-program run on board the vessels, making delivery of higher-resolution SAR data to the end-users possible.

5. Pulse-Coupled Neural Network (PCNN) based segmentation algorithm has been developed as a part of the work and it gives reasonable segmentations in applicable execution time for our data. Its performance for our Radarsat-1 data is comparable or better than some other segmentation methods typically used.

6. Distinguishing open water and sea ice from each other has been developed from the earlier pixel-wise method to a segment-wise classification. According to our tests this improves the classification performance.

7. Higher-order statistical methods have been developed and tested for sea ice SAR classification. The Independent Component Analysis (ICA) based texture classification gives extra information about the SAR texture compared to the standard SAR texture statistics (mean, variance) approach or the roughness statistics (relative number of edges in a segment). The geophysical interpretation and combining it to certain sea ice classes seems, however, to be a difficult task and still requires further research.

8. The evaluation and validation of SAR-based sea ice products has been developed. Typically the classification results are only compared either to a very few point-wise field measurements or visual interpretation of the SAR data. We use digitized ice charts from FIS and electromagnetic induction based ice thickness measurements to evaluate and validate our algorithms. Digitized ice charts are drawn by FIS sea ice experts based on many data sources, including field observation and multiple remote sensing data sets. This kind of evaluation scheme covers large areas and makes statistical comparison of the data sets feasible.

The techniques and methods developed and described in this work make it possible to produce and deliver better SAR-based sea ice products than earlier. One significant improvement is also the higher spatial resolution. Our operational ice typing algorithm has been updated based on these results, and the SAR-refined ice thickness is also currently in operational use.

1.3 Organization of the Work

This thesis consists of an introductory part, giving a summary of the problem and main results of the research work, together with a set of original publications covering details. Some of the introductory part also extends the content of the publications.

The introduction consist of different sections, whose common denominator is the aim to develop and to deliver Near-Real-Time (NRT) sea ice information to end-users in a user-friendly format. These SAR-based sea ice products are typically thematic maps compatible with the end-users' navigation and information systems.

First the basic properties of SAR and Baltic Sea ice are presented in Section 2. In section 3 an overview of the earlier related work is presented. Then the preprocessing stages of SAR data are shortly presented in Section 4, including rectification into a geographical projection, and correcting the radar measurement (incidence) angle for sea ice. Also some speckle filtering techniques are presented.

Our wavelet-based sea ice SAR compression algorithm is presented in Section 5. Use of this algorithm enables transmission of large SAR images to end-users on ships with relatively narrow communication bandwidths.

In Section 6 a combined SAR image segmentation and classification method based on Pulse Coupled Neural Networks (PCNNs) is presented. In Section 7 a selection of texture based methods for the same purpose are presented. All the presented

methods can be used to refine the sea ice classification based on the SAR backscattering level only.

In Section 8 ice thickness history is combined with a novel SAR image, and sea ice thickness estimates are generated based on this information. The digitized ice charts (including thickness information) of the earlier days are used as the history information, and the pixel intensity segment averages for a segmented SAR image are used together with the history information to generate segment-wise ice thickness estimates.

Validation of the sea ice SAR data products which contain parameters (such as ice thickness) estimated from SAR data, are difficult to evaluate and validate. These validation and evaluation questions are addressed in the end of the sections describing the methods. Finally the work is summarized with some concluding remarks in Section 9.

An overview of earlier related work on SAR image compression is presented at the end of the Section 5. An overview of SAR classification, including ICA-based classification, is presented at the end of Section 7. This selection was made because the overviews utilize much terminology presented in these sections. On the other hand it is very difficult to distinguish between intensity-based segmentation or classification and texture-based classification, because they are typically used in combination.

The parts extending the publications are the section describing speckle filtering (Section 4.3.), the section dealing with PCNN and perfect segmentation (Section 6.4), the section comparing SAR segmentation methods (Section 6.5), the section describing the fast ice detection (Section 6.7), the section describing the pixel-wise ICA-based classification (Section 7.6) and the section describing ICA-Based classification of known textures (Section 7.7).

1.4 List of Original Publications

1. J. Karvonen, M. Similä and M. Mäkynen, An Iterative Incidence Angle Normalization Algorithm for Sea Ice SAR Images, *Proc. IEEE International Geoscience and Remote Sensing Symposium 2002 (IGARSS'02)*, vol. III, pp. 1524–1528, 2002.

2. J. Karvonen, M. Similä, A wavelet transform coder supporting browsing and transmission of sea ice SAR imagery, *IEEE Transactions on Geoscience and Remote Sensing*, vol. 40, n. 11, pp. 2464–2485, 2002.

3. J. Karvonen, Baltic Sea Ice SAR Segmentation and Classification Using Modified Pulse Coupled Neural Networks, *IEEE Transactions on Geoscience and Remote Sensing*, vol. 42, n. 7, pp. 1566–1574, 2004.

4. J. Karvonen, M. Similä, M. Mäkynen, Open Water Detection from Baltic Sea Ice Radarsat-1 SAR Imagery, *IEEE Geoscience and Remote Sensing Letters*, vol. 2, n. 3, pp. 275–279, 2005.

5. J. Karvonen, Feature Detection from Preprocessed Sea Ice SAR Data Based on Higher-Order Statistics, *Proc. IEEE International Geoscience and Remote Sensing Symposium 2003 (IGARSS'03)*, vol. VI, pp. 3450–3452, 2003.

6. J. Karvonen and M.Similä, Independent Component Analysis for Sea Ice SAR Image Classification, *Proc. IEEE International Geoscience and Remote Sensing Symposium (IGARSS'01)*, vol. III, pp. 1255–1257, 2001.

7. J. Karvonen, M.Similä, ICA-Based Classification of Sea Ice SAR Images, *Proc. 23rd European Association of Remote Sensing Laboratories (EARSeL) Annual Symposium*, Gent, Belgium, pp. 211–217, 2003. Millpress 2004.

8. J. Karvonen, M. Similä, I. Heiler, Ice Thickness Estimation Using SAR Data and Ice Thickness History, *Proc. IEEE International Geoscience and Remote Sensing Symposium 2003 (IGARSS'03)*, vol. I, pp. 74–76, 2003.

9. J. Karvonen, M. Similä, J. Haapala, C. Haas, M. Mäkynen, Comparison of SAR Data and Operational Sea Ice Products to EM Ice Thickness Measurements in the Baltic Sea, *Proc. IEEE International Geoscience and Remote Sensing Symposium (IGARSS'04)*, vol. V, pp. 3021–3024, 2004.

1.5 Author's Contribution

In publication 1, correction, or normalization, of the radar incidence (or measuring) angle, which varies in SAR images and in different parts of each SAR image is studied. The SAR backscattering is dependent on this angle. An incidence angle normalization algorithm is presented. The statistical work which forms the basis of the publication 1, was done at Helsinki University of Technology Laboratory of Space Technology (HUT/LST) by Mr. Marko Mäkynen [154]. The iterative algorithm was mainly developed by the author, based on the statistical analysis made at HUT/LST, and the algorithm was implemented by the author.

In publication 2, a wavelet-based sea ice SAR compression is presented and performance evaluations and comparisons to other existing algorithms are performed. The compression algorithm was mainly developed by the author. The statistical analysis, aiding to define algorithm parameters, was mostly made by Mr. Markku Similä, the writing of the publication was done in co-operation, and the algorithm was implemented by the author.

In publication 3, sea ice SAR segmentation and classification based on a simplified pulse-coupled neural network are studied. Also some empirical results for Radarsat-1 data over the Baltic Sea ice are presented. The idea to use pulse-coupled neural networks in SAR segmentation and classification was by the author. The author is the sole author of this publication.

Publication 4 is about distinguishing between open water and sea ice in SAR data over the Baltic Sea. It was mainly written by the author and the implementation, testing and comparisons were also made by the author. The idea to utilize signal autocorrelation in distinguishing open water from sea ice was adopted from ref. [210]. In references [209] and [210] the discrimination problem is formulated using a

Gaussian mixture model for the backscattering intensity values and the contextual information is based on the Markov Random Field formalism in which the strength of the contextual information is based on the autocorrelation value.

Publication 5 is about locating edge-like and spot-like features in sea ice SAR images using higher-order moments. These features can then be utilized in classification of ice areas. The method can also be utilized in detecting targets, e.g. ships, in open water regions. The author is the sole author of this publication.

In publications 6 and 7, texture-based classification of sea ice SAR imagery, using basis generated by ICA as texture primitives, is studied. The idea of applying ICA to our SAR data was by the author, and most of the writing work of the publications 6 and 7 was done by the author.

In publication 8, an algorithm for estimating sea ice thickness in the Baltic Sea using ice thickness history data and novel SAR data is presented. The publication 8 was written in co-operation with two other authors. The ideas of the algorithm were developed by the author and Mr. Markku Similä. The algorithm implementation and testing were made by the author.

In publication 9, SAR data and our sea ice products (i.e. geographically localized sea ice information in form of thematic maps) are compared to ice thickness measurements conducted in the Baltic Sea during the winter 2002/2003. The ice thickness measurements were made with a helicopter-borne electromagnetic induction (HEM) based instrument. The publication 9 was written in co-operation with four co-authors. The statistical analysis and comparisons were mainly made by the author. The ice thickness measurements were made by the Alfred Wegener Institute (AWI, Bremerhafen, Germany) using their HEM instrument, mostly by Dr. Christian Haas.

Most of the data processing and all the operational implementations were programmed using standard ANSI C-language to maintain portability between different operating system platforms in use at FIMR and our co-operators (product co-developers and end-users). All of these programs were written by the author, likewise the Unix shell-scripts making automation of computation and data transmission at the FIMR server possible. Also the web-pages, interactive web feedback form and CGI scripts to collect user feedback about the sea ice SAR compression, were implemented by the author.

Chapter 2

Synthetic Aperture Radar and Baltic Sea Ice SAR Data

2.1 Introduction

In this chapter basic concepts of synthetic aperture radar (SAR), some characteristic properties of Baltic Sea ice, and the delivery of sea ice products derived from SAR data to end-users are presented.

Finnish Institute of Marine Research (FIMR) and its operational part Finnish Ice Service (FIS) provide sea ice information for navigational purposes in the area of the Baltic Sea, especially in the Gulf of Bothnia and Gulf of Finland. During winters a daily ice chart (see Fig. 2.1) is made at FIS. The ice charts are based on several sources of information, e.g. NOAA (National Oceanic and Atmospheric Administration) AVHRR (Advanced Very High Resolution Radiometer) images, Radarsat-1 (a Canadian base-borne C-band SAR instrument) images and field observations.

In addition to the daily ice charts FIS produces ice reports in text or oral formats, and digital versions of the ice chart in several formats. FIS also provides some other digital products which are delivered to customers. FIS is in close co-operation with Finnish Maritime Administration (FMA) and with the ice breakers hosted by FINSTASHIP, a shipping company owned by the state. The operational digital products derived from SAR data are the automated sea ice SAR interpretation and an ice thickness map which is based on SAR data and an earlier digital ice chart. Also compressed Radarsat-1 and NOAA AVHRR images are available and transmitted to ships. Additionally ice forecasts based on an ice dynamics model and sea weather forecasts are provided by FIS. For more details about the services and operation of FIS see references [77, 78, 191, 238, 239].

FIMR, together with the Swedish Meteorological and Hydrological Institute (SMHI), buys each winter about 100 Radarsat-1 ScanSAR narrow mode and ScanSAR wide mode images, with a range of about 300×300 km^2 and 500×500 km^2, respectively,

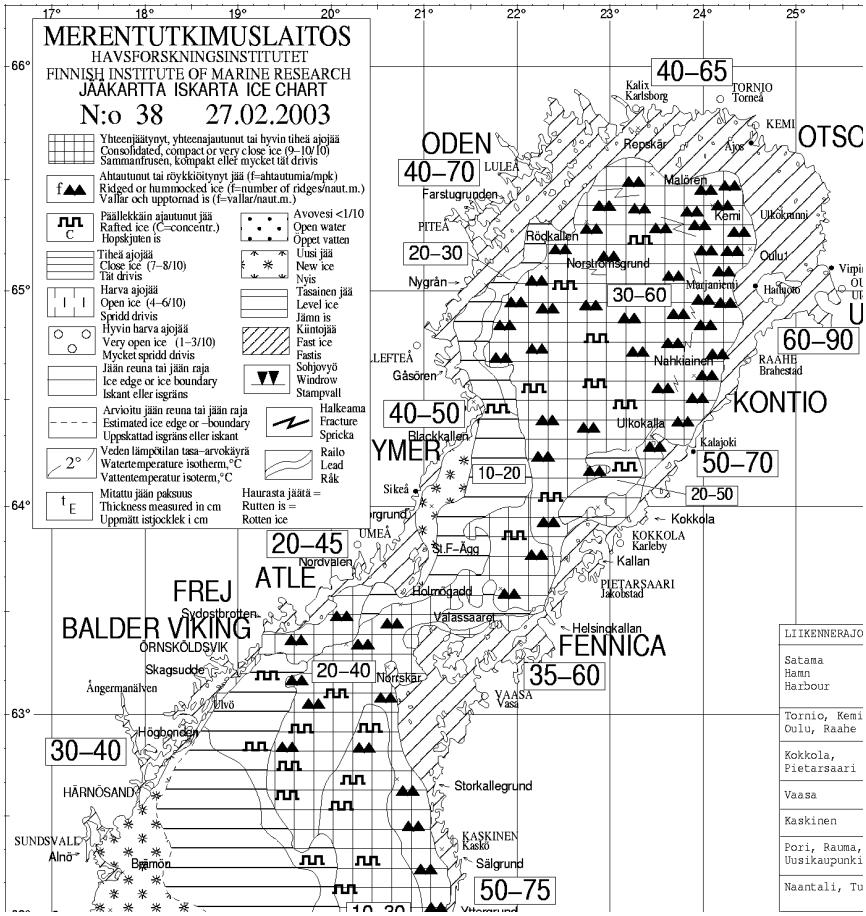

Figure 2.1: A part of an ice chart, covering the Bay of Bothnia, Feb 27th 2003. Ice charts over the Baltic Sea are produced daily during the ice period every winter.

over the Baltic Sea. These images are used in making ice charts and producing an automated sea ice classification. Because of the dark and cloudy winters, Radarsat-1 images are a very important source of sea ice information in the area of the Baltic Sea. The images are received from Radarsat-1 in Tromsø, Norway by Kongsberg Satellite Services AS (KSAT). The images are then sent by File Transfer Protocol (FTP) to FIS, where they are rectified and processed into the Mercator projection, and a land mask is applied to them. The rectified and land-masked images are again sent to FIMR by FTP. At FIMR an automated classification and a SAR-refined ice thickness chart are produced immediately after receiving a SAR image. The produced thematic maps are sent back to FIS in a custom format, readable by the on-board client software. From FIS the resulting thematic maps can then be sent to the end-users. Also the rectified Radarsat-1 images can be sent to end-users for their visual interpretation.

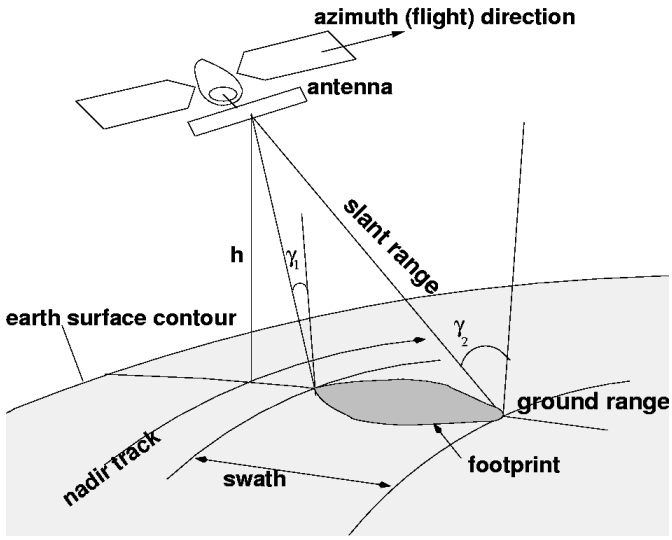

Figure 2.2: Simplified SAR measuring geometry. The azimuth and ground range directions are perpendicular to each other at nadir and the incidence angle varies between γ_1 and γ_2, h is the satellite track height from the earth surface. The instrument makes measurements in slant range which is then usually converted to the ground range, from which it can then be further processed to a desired projection (Mercator projection in our case). The nadir track is the projection of the flight track (in azimuth direction) on the earth surface.

2.2 Synthetic Aperture Radar

Radar instruments are active instruments i.e. transmitting electromagnetic radiation of a certain frequency (frequency band), and then measuring the signal backscattered from targets, in our case Baltic Sea ice. Radars typically transmit pulses of radiation with a constant repetition time interval. The inverse of this time is known as the pulse repetition frequency (PRF).

Synthetic aperture radar (SAR) is a radar instrument moving over the object area to be measured. Synthetic aperture comes from the fact that the measuring resolution in the azimuth direction (i.e flight direction, see Fig. 2.2) is improved by utilizing the Doppler effect, and producing a larger "synthetic aperture" compared to the real aperture. The utilization of the Doppler effect is based on the fact that the instrument has slightly different velocity with respect to the different parts of the object area because the distance from the instrument to the different parts of the object area differ. These Doppler shifts can then be used to localize the backscattering more precisely within the antenna footprint in azimuth direction. More detailed descriptions of SAR operation and signal processing can be found e.g. in [132] and [5].

SAR resolution in the ground range direction (see Fig. 2.2) is dependent on the

PRF and the pulse length. Short pulses with a high PRF produce high ground range resolution, but short pulses require high transmission power. In SAR the ground range resolution is improved by using a technique called range pulse compression. In this technique, instead of a single-frequency pulse, a so-called "chirp" is transmitted. A chirp is a short-time pulse in which the frequency varies from higher to lower frequency and then back to higher frequency again (e.g. linear frequency modulation). Matched filtering of the received signal with the complex-conjugated, time-reverted function of the SAR system response of a point target, i.e. the range reference function is applied to compress the pulse. Pulse compression technique is used to resolve targets which have overlapping radar returns. This is possible because of the frequency modulated ("chirp") signal. In practice the image reconstruction is divided into range and azimuth compression (the frequency in azimuth direction is varied because of the Doppler effect) which perform compression of signals spread over a larger area (over multiple desired resolution points) in both the range and azimuth directions into a point signal. The compression is usually carried out by adopting Fourier transform to calculate convolution of received signals and a *reference function*. The reference function of range compression is the complex conjugate of the transmitted signal, while the reference of azimuth compression is a complex conjugate of the chirp modulated signal. Therefore the process in the azimuth direction is similar to that in the range direction because the Doppler-shift of different locations along the azimuth direction causes similar kind of frequency altering. The azimuth reference function, however, differs depending on the range.

Radar cross section (RCS, denoted by σ_R) is a property of a single target, describing how well the target reflects the radar energy. RCS is the energy received by the sensor relative to the energy received in the case of an isotropic (i.e. scattering equal to all directions) scatterer. The backscattering coefficient, σ^0, is the average scattering cross section per unit area

$$\sigma^0 = E[\frac{\sigma_i}{A_i}] \tag{2.1}$$

where σ_i and A_i describe the RCS and area of a single scatterer inside the resolution cell (image pixel), and E is the expectation operator. Backscattering coefficient is a normalized version of the radar cross section, describing the backscatter properties of a pixel area, probably containing several different backscatterers.

The backscattering coefficient is usually expressed in logarithmic scale and in decibels (dB)

$$\sigma^0{}_{\text{dB}} = 10 \log_{10} \sigma^0. \tag{2.2}$$

For the isotropic case $\sigma^0{}_{\text{dB}} = 0$ dB. If the scattering is focused toward the receiving antenna then $\sigma^0{}_{\text{dB}} > 0$ dB, and if the scattering is focused away from the receiving antenna then $\sigma^0{}_{\text{dB}} < 0$ dB. Typically a very high backscattering, e.g. from urban areas or very rough surfaces is higher than $-5dB$, and high backscatter from rough surfaces (e.g. dense vegetation) is between $-10dB$ and $0dB$. Smooth surfaces (e.g. calm water or level ice) produce low backscatter, typically below $-20dB$.

The relation between the transmitted and received power is defined by the radar equation [232]

$$P_r = \frac{P_t {G_A}^2 \lambda^2}{(4\pi)^3 R^4} \sigma, \tag{2.3}$$

Table 2.1: Typical microwave frequency bands.

Band	λ (mm)	f (GHz)
Ka	8–11	40–26.5
K	11–17	26.5–18
Ku	17–24	18–12.5
X	24–38	12.5–8
C	38–75	8–4
S	75–150	4–2
L	150–300	2–1
P	300–1000	1–0.3

where σ is the RCS, P_r is the received power, P_t is the transmitted power, G_A is the antenna power gain, λ is the wavelength and R is the distance to the object.

The backscattering of a SAR resolution cell typically consists of multiple scatterers. If there are N scatterers in a resolution cell, the received amplitude A_{SAR} and phase θ can be expressed as a sum of the N scatterers [170]

$$A_{\mathrm{SAR}} e^{i\theta} = \sum_{k=1}^{N} A_k e^{i\theta_k}, \tag{2.4}$$

where A_k are the amplitudes and θ_k the phases of the scatterers.

Both the real and imaginary parts of the backscattering are normal-distributed with zero mean and variance of $\sigma_R/2$, while the phase θ is evenly distributed between π and $-\pi$. The amplitude is Rayleigh distributed and intensity (power) $I_{\mathrm{SAR}} = A_{\mathrm{SAR}}^2$ has negative exponential distribution. From these a product model for the measured intensity can be derived [170]:

$$I_{\mathrm{SAR}} = \sigma_{\mathrm{R}} n, \tag{2.5}$$

where n is a noise term, also known as *speckle*. The received and averaged intensity is K-distributed [170]. K-distribution is derived from the gamma distribution. Because the phase is, according to the model, evenly distributed noise, its information content is usually considered insignificant, and only amplitude or intensity are used in most SAR products. However, phase information has significance e.g. in SAR interferometry applications.

The common microwave frequency bands used e.g. in radar applications are shown in Table 2.1. Typically the SAR-instruments used for sea ice monitoring are C-band instruments (Radarsat-1, Envisat ASAR), and the wavelength is around 5 cm. The history of space-borne SAR-instruments is listed in Table 2.2. The SIR-C/X-SAR and SRTM mission were on the space shuttle and only operated for the durations of the shuttle flights. In addition to the space-borne instruments SAR-campaigns with air-borne instruments have been performed typically for preparing a space-borne mission.

Table 2.2: Space-borne SAR missions, history and near future.

Mission	Country	Band	Time
SEASAT	USA	L	1978
ERS-1	Europe (ESA)	C	1991–2000
J-ERS-1	Japan	L	1992–1998
SIR-C/X-SAR	USA	L, C, X	1994
Radarsat-1	Canada	C	1995–
ERS-2	Europe (ESA)	C	1995–
SRTM	USA	C, X	2000
ENVISAT ASAR	Europe (ESA)	C	2002–
ALOS PALSAR	Japan	L	2005–
TerraSAR-X	Germany	X	2006
SAR-Lupe	Germany	X	2006
CosmoSkymed	Italy	X	2006
Radarsat-2	Canada	C	2007

The current satellite-borne SAR instruments for operational sea ice monitoring covering reasonably wide areas of the Baltic Sea are the above mentioned C-band instruments. The widest area in range can be achieved using the ScanSAR mode of the instruments. In this mode the antenna beam is steered such that a larger swath (extend in range direction) can be covered, in a lower resolution. Radarsat-1, which is our main operational data source, has two ScanSAR modes, ScanSAR narrow mode and ScanSAR wide mode. ScanSAR narrow mode has a swath width of about 300 km, and ScanSAR wide mode about 500 km. ScanSAR narrow mode has the resolution of 50 m/pixel and ScanSAR wide mode 100 m/pixel. However, FIMR has used both in the resolution of 100 m.

Typically several SAR intensity values over the same area are averaged to reduce speckle. Because the speckle components of these samples are independent, the speckle variance is reduced in the averaging. The *number of looks* is the number of measurements over the same pixel area averaged in the SAR processing. SAR with only one measurement over one pixel is a single look SAR. The number of independent single look (complex) components over a pixel can also be non-integer if the measuring areas overlap only partially. In the SAR processing some adjacent measurements are often averaged to further reduce the speckle, in the cost of resolution, increasing the number of looks in such products. The statistics of the speckle are usually described in terms of the *effective (or equivalent) number of looks* (ENL). This is intended to represent the speckle component of the observed intensity. Normally, of course, the intensity combines both speckle and RCS fluctuations. However, if the underlying RCS is uniform then ENL can be defined as

$$\mathrm{ENL} = \frac{\mu^2}{\sigma^2}, \tag{2.6}$$

where μ and σ^2 are the local mean and variance, respectively. In general estimating the looks measure yields values which are smaller than the true ENL because additional RCS fluctuations are included. Only if the RCS is constant, or if the observed intensity is divided by the true underlying RCS, would the looks measure correspond to the ENL.

We are receiving Radarsat-1 SAR data from KSAT in Tromsø, Norway, and they have built a SAR processor, i.e. a system converting the raw SAR data received from the satellite into SAR images, of their own. For this data the backscattering coefficient can be computed as

$$\sigma^0 = \left(\frac{{B_l}^P}{G} \right)^2 \sin\gamma, \tag{2.7}$$

where P is the 8-bit image pixel value we receive, logarithmic scale $B_l = 1.024$, gain factor $G = 0.16$, and γ is the local incidence angle (communication with KSAT) between γ_1 and γ_2 in Fig. 2.2.

According to our research [publications 3 and 5] the data distributions in uniform areas of such logarithmic images are very close to Gaussian distributions. This gives some advantages in data processing compared to more complex distribution families in modeling the data.

2.3 Backscattering

Backscattering of electromagnetic radiation from a medium is defined by the geometry of the medium and by the electrical features of the medium. Assuming that we have two uniform media and a boundary surface between them, the backscattering is then described by the geometry of the boundary surface and by the electrical properties of the two media. The boundary surface geometry is typically described by two parameters, slope and roughness. The electrical features are described by the dielectric constant, ϵ_c, for each medium:

$$\epsilon_c = \epsilon' - i\epsilon'', \tag{2.8}$$

where the real part ϵ' is the permittivity and the imaginary part ϵ'' is the dielectric loss of the medium. Permittivity describes how easily energy passes across the dielectric interface, and the loss term describes how much energy is absorbed in the volume while passing through the dielectric interface. A large difference in permittivity between two media causes larger scattering at the media surface, and when the difference is small scattering from the volume is dominating. The permittivity is very high for conductors, like metals, for dry natural materials it is typically in the range 3–8. For water permittivity is around 80, and thus dampness increases the permittivity of natural materials. Usually a value relative to the permittivity of the vacuum is used

$$\epsilon_r = \frac{\epsilon_c}{\epsilon_0}. \tag{2.9}$$

Penetration depth δ_p is defined as

$$\delta_p = \frac{1}{2\alpha_A}, \tag{2.10}$$

where α_A is the absorption coefficient of the media. Absorption coefficient is dependent of the dielectric constant, for details see e.g. [231]. The penetration depth indicates the maximum depth of the medium that contributes to the backscattering coefficient. The loss tangent

$$\tan \delta_r = \frac{\epsilon''}{\epsilon''} \tag{2.11}$$

is directly related to the attenuation of the radar signal (i.e. penetration depth) in the medium. First-year sea ice is a mixture of pure ice, air baubles and brine and its dielectric properties can vary significantly. A review of the dielectric and extinction properties of sea ice and snow can be found in [83].

Backscattering is typically divided into surface backscattering, i.e. backscattering from the boundary surface, and volume backscattering, i.e. backscattering from the media (in our case sea ice) volume. Backscattering from the Baltic Sea ice depends on ice and snow surface small-scale roughness, large-scale ice deformation, snow wetness, density and thickness, ice density, temperature, salinity and size and distribution of air bubbles in the ice. The main scattering mechanisms measured by the SAR instruments in the case of Baltic Sea ice are shown in Fig. 2.3. The measured scattering is also contributed by multiple scattering (e.g. the scattering from the ice/water interface can scatter further from the ice volume or water/snow interface). Radar scattering occurs when there is an abrupt change in the value of ϵ_r within the distance of a wavelength, which indicates that the backscattering is dependent on the wavelength. The reflection coefficient ρ_r is related to the dielectric constant as

$$\rho_r = \frac{\sqrt{\epsilon'} - 1}{\sqrt{\epsilon'} + 1}. \tag{2.12}$$

The scattering thus comes from the air/ice interfaces, ice/water interfaces, (if the losses are low enough to permit penetration), snow/ice interfaces and inhomogeneities in snow and ice.

In scattering modeling, surface scattering of a homogeneous surface is modeled by terms of deviation of the relative means square (RMS) height and correlation length L_c. L_c is defined as the distance l where the autocorrelation $C(l) = \frac{1}{e} \approx 0.37$. For small surface roughness the small perturbation model (SPM) [232] can be applied. In this case the roughness is noticeably less than the wavelength and the slope is less than one. The backscattering is proportional to that height profile component which is in resonance with the transmitted wave. The corresponding surface roughness wavelength Λ_B is

$$\Lambda_B = \frac{\lambda}{2 \sin \gamma}. \tag{2.13}$$

This mechanism is called the Bragg scattering [232]. Scattering from surfaces with a larger roughness comes from the surfaces perpendicular to the SAR signal. These surfaces reflect the radiation back towards the instrument. For larger surface roughness the integral equation model (IEM) [67] is typically used. IEM is based

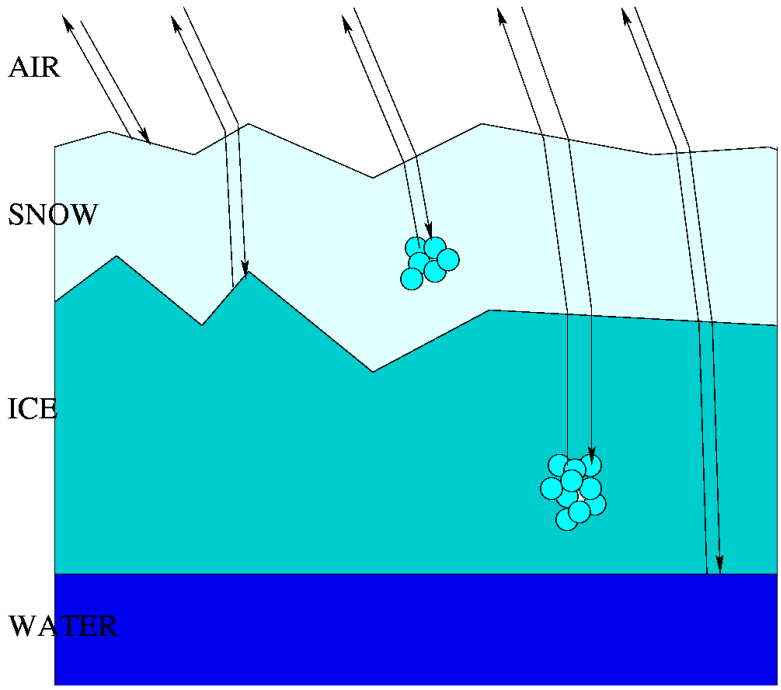

Figure 2.3: Basic scattering mechanisms contributing the measured backscattering of the Baltic Sea ice. From left to right: Scattering from snow surface (snow/air boundary), scattering from the snow/ice surface, scattering from the snow volume, scattering from the ice volume, and scattering from the ice/water surface.

on approximative iteration of surface integral equations with the physical optics theory model (POT) [232] as its starting point. Also more elaborated scattering models based on multi-resolution surface roughness have been developed, e.g. [162, 163]. Deformed ice has high surface roughness and IEM is not suitable for modeling deformed ice. Deformed ice is typically modeled by scattering blocks of different shape and orientation distributions [26, 161].

Volume scattering comes from inside the ice, and typical volume scattering models assume the volume to contain air bubbles and brine pockets. Statistical distributions for the brine pockets and air bubbles are also required [29]. However, surface scattering is the dominant scattering mechanism for the Baltic Sea ice at C–band and volume scattering has only minor importance [26].

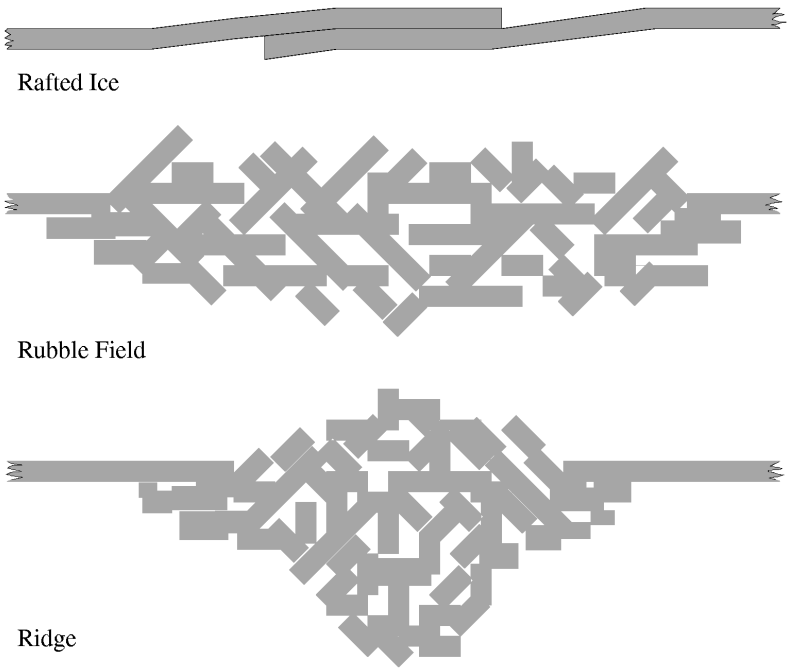

Figure 2.4: Rafted ice (upper) is formed when two ice layers are rafted over each other, rubble fields (middle) and ridges (stripe-shaped, lower) are more deformed ice types.

2.4 Baltic Sea Ice

Based on ice surface structure sea ice can be divided into level ice, which is formed by thermal growth, and deformed ice which is caused by ice dynamics, i.e. motion. The motion can be diverging, compacting or shearing, where rotational forces are present. Divergent motion causes leads or fractures in the ice, and thinner level ice is formed in these leads. Thicker level ice is originated from the initial freezing. Convergent motion in the sea ice causes deformations: rafted ice, rubble fields, ridges and hummocks. A schematic cross-sectional view of rafted ice, rubble field and ice ridge is shown in Fig. 2.4. It should be noted that the ridge keel (the underwater part of the ridge) height is significantly larger than the height of the ridge sail (the part above water). According to [106] the keel height h_{keel} is related to the sail height, h_{sail} as

$$h_{\mathrm{keel}} = 6.35 h_{\mathrm{sail}} - 0.02\ m. \tag{2.14}$$

Sea ice can be divided into different types in multiple ways, e.g. by concentration, stage of development, form, or the ice thickness [168, 240]. The Baltic Sea ice is all first-year ice, i.e. all the Baltic Sea ice melts every year. In the polar areas there are also second-year and multi-year ice (this is a classification based on stage of development). The research at FIMR is mainly concentrated on the classification

of the forms of the Baltic Sea ice distinguishable in the SAR images. Here are some divisions of first-year sea ice into different ice classes, according to [240]:

1. Stage of development

   - *New ice*, recently formed ice, composed of ice crystals only weakly frozen together.
   - *Shuga*, an accumulation of spongy white ice lumps, whose size is a few centimeters across.
   - *Nilas Ice*, a general term for recently formed ice which is usually less than 10 cm thick. Nilas ice is a thin elastic crust of ice, easily bending on waves and swell and under pressure, thrusting in pattern of interlocking "fingers" (*finger rafting*). It has a matt surface.
   - *Ice rind*, a brittle shining crust of ice formed on a quiet surface by direct freezing or from new ice, usually in water of low salinity, thickness up to about 5 cm.
   - *Pancake ice*, predominantly circular pieces of ice from 30 cm to 3 m in diameter, thickness up to about 10 cm.

2. Concentration

   The concentrations here are given in tenths which is typical in ice charting.

   - *Compact ice*, concentration 10/10, no open water visible,
   - *Consolidated ice*, concentration 10/10, floats frozen together.
   - *Very close ice*, concentration 9/10 but less than 10/10.
   - *Close ice*, concentration 7/10–8/10.
   - *Open ice*, concentration 4/10 – 6/10.
   - *Very open ice*, concentration 1/10–3/10.
   - *Open water*, concentration $< 1/10$, freely navigable water.
   - *Ice-free*, no ice at all present.

3. Forms of fast ice

   Fast ice is ice which remains fast along the coast. It is attached to the shore or between shoals.

   - *Grounded ice*, ice which is aground in shoal water.
   - *Stranded ice*, ice which has been deposited on shore during high water.
   - *Grounded hummock*, hummocked grounded ice formation.

4. Forms of floating ice

   - *Ice floe*, any relatively flat piece of sea ice, 20 cm or more across.
   - *Ice cake*, a relatively flat piece of sea ice, less than 20 cm across.
   - *Floeberg*, a massive piece of sea ice composed of a hummock or group of hummocks frozen together and separated from any ice surroundings.

- *Floebit*, a relatively small piece of ice, normally not more than 10 m across, composed of hummocks or part of ridges frozen together and separated from any ice surroundings.
- *Brash ice*, accumulations of floating ice, made up of fragments not more than 2 m across. The pieces are wreckage of other forms of ice.

5. Deformation processes
   - *Fracturing.*
   - *Rafting.*
   - *Ridging.*
   - *Hummocking.*
6. Openings in sea ice
   - *Fracture*, a general term.
   - *Crack*, all fractures which have not parted.
   - *Fracture zone*, area which has many fractures.
   - *Lead*, a fracture or passage way through sea ice navigable by surface vessels.
7. Ice surface features (large scale)
   - *Level ice.*
   - *Deformed ice.*
   - *Snow-covered ice.*
   - *Bare ice, no snow cover.*

Additionally classification can be made by the stage of melting, during the melting period. Melting period is, however, difficult for SAR-based sea ice monitoring because of wet snow or water on the ice surface. Yet another division is division by the shape or arrangement of the ice fields (large, medium and small ice fields depending on their size, ice belts and ice strips). The term *ice edge* refers to interfaces between ice and open area, and *ice boundary* to interfaces between different ice areas.

Navigationally the most important sea ice parameters are ice thickness, ice concentration i.e. the relative amount of ice per unit area, locations and sizes (distributions) of the deformations like ice ridges and rubble fields, and locations of the leads.

Because many of the classes presented above are much smaller than SAR resolution (in our case 100 m), many of the single features can not be distinguished or classified based on SAR data. However, even a single such feature can contribute to backscattering, and multiple features more probably have their contributions on the backscattering. Because of these facts a coarser classification of sea ice types is required in studies with Radarsat-1 SAR data. A division of the Baltic Sea ice types into classes is based on the classification operationally used for the

Finnish ice charts, and also on the Baltic Sea ice code in [203]. We have used this classification in evaluation of some of our SAR classification schemes. The ice type classes used are:

1. *Nilas ice* (NI).
2. *Smooth level ice* (SLI) is almost unaffected by deformation, only cracking or finger rafting may occur.
3. *Rough level ice* (RLI) has protruding ice blocks and floe edges and low uneven surface areas and it has typically broken and frozen several times.
4. *Slightly deformed ice* (SDI) consists of ice ridges, uneven surfaces and level ice areas, the sizes of which are usually larger than the pixel size in SAR images.
5. *Highly deformed ice* (HDI) is such that the average size of level ice areas is usually smaller than the SAR pixel size and the proportion of level ice areas is smaller than in SDI, i.e. the degree of deformation is higher. Visual discrimination of SDI from HDI (e.g. from video imagery) is often difficult and subjective.
6. *Brash ice* consists of accumulations of ice fragments not more than 2 m across. They are wreckage of other forms of ice. Their surface is very rough in scales of about 10–30 cm. Brash ice is further divided into *loose brash ice* (LBI) and *frozen brash ice* (FBI).

In this classification most of ridged ice, hummocked ice and rubble fields are all included in the HDI class, and rafted ice is in the SDI class.

Also the inner structure of the sea ice varies depending on the amount of air bubbles and brine pockets in the ice. This inner structure affects the volume scattering. The ice salinity is defined by the brine volume which affects to the electrical and also the structural properties, e.g. ice strength. Baltic Sea ice is brackish water whose salinity varies depending on the location, typical salinities are 0.2–2 ‰. Experiments show that if the salinity is over 0.5 ‰ and RMS height is over 1.5 mm, surface backscattering is fully dominant at C-band. In practice only when the salinity is less than 0.2 ‰ the volume scattering plays a role in the Baltic Sea ice scattering process [26]. According to [26] for the Baltic Sea ice

$$\epsilon' = 3.05 + 7.2 v_{\mathrm{br}}, \tag{2.15}$$

$$\epsilon'' = 0.001 + 3.3 v_{\mathrm{br}}, \tag{2.16}$$

where 0.001 is ϵ'' for saltless water and v_{br} is the brine volume fraction, i.e. $v_{\mathrm{br}} \in (0, 1)$.

Two typical smoothed ice thickness distributions, measured by the HEM instrument in March 2004, in the Baltic Sea are shown in Fig. 2.5, these distribution correspond to two different Radarsat-1 backscattering levels (-20 dB and -10 dB). Actually there is also a peak at zero thickness (open water), i.e. the ice concentration is typically less than 100 %, but it has been removed from the distributions.

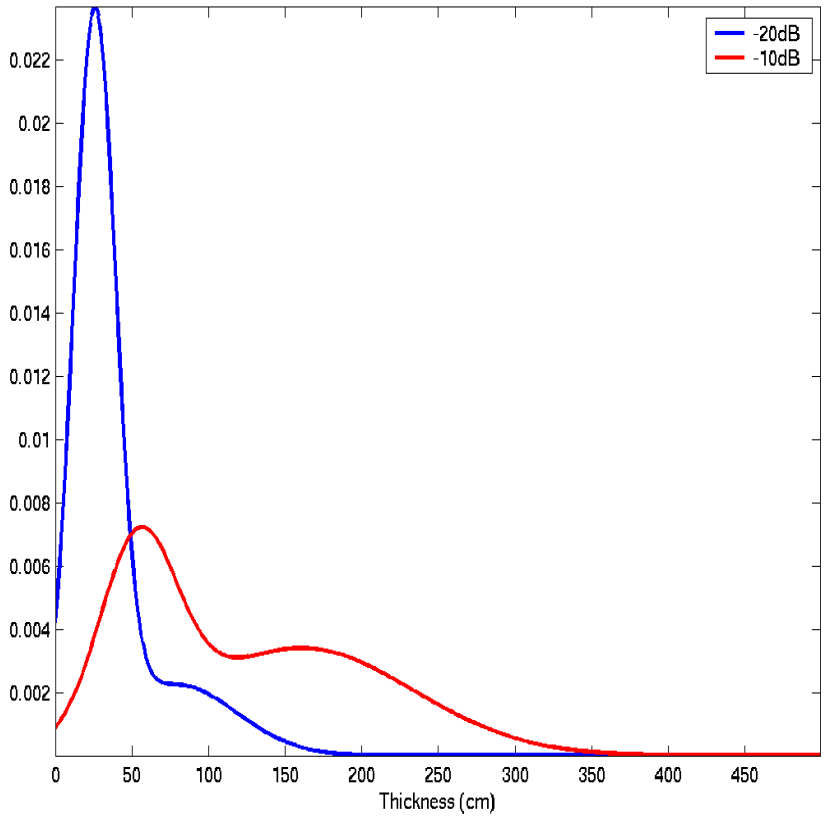

Figure 2.5: Two smoothed ice thickness distributions at different backscattering levels, based on Radarsat-1 and HEM ice thickness data.

It can be seen that typically the distribution has a heavier tail and lower peak as the backscattering level increases. This can also be seen in Fig. 2.6 where the distributions are interpolated for a range of ice thickness and backscattering values based on the Radarsat-1 data and HEM ice thickness measurements.

Also the effects of the snow cover to the backscattering must be taken into account because Baltic Sea ice is typically snow covered. At C-band dry snow cover is in practice meaningless, it only slightly changes the incidence angle because of refraction at the air-snow boundary. Wet snow instead is problematic because dampness attenuates the backscattering, and very wet snow is even the dominant backscatterer, masking off most of the sea ice information. Actually the penetration depth in snow decreases rapidly as a function of snow wetness for wetness values below 1 % and the decerase is lower for higher wetness [82].

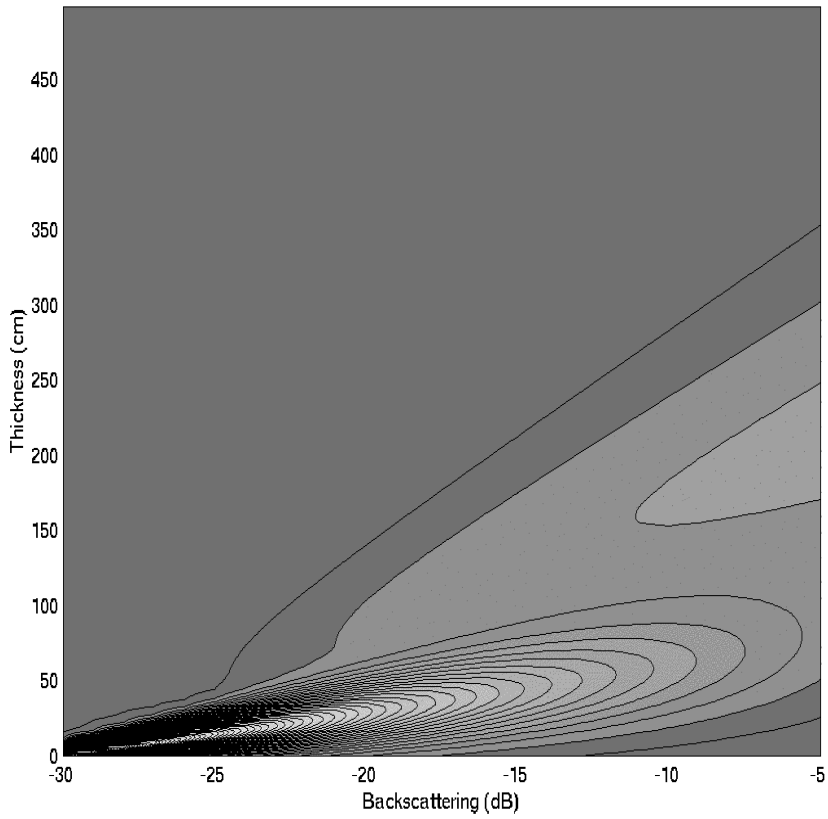

Figure 2.6: Contour plot of estimated ice thickness distributions as a function of the Radarsat-1 backscattering coefficient σ^0. The distributions shown in Fig. 2.5 are cross sections of this distribution at -20 dB and -10 dB.

2.5 Backscattering Models and Scatterometer Measurements over the Baltic Sea

Modeling of the surface backscattering plays an important role for the Baltic Sea ice because surface scattering is the dominant scattering mechanism for the Baltic Sea ice. For open water the volume scattering is always practically nonexistent. The surface backscattering from a homogeneous surface is typically modeled with RMS height and correlation length. RMS height is the standard deviation of a Gaussian distribution when the surface height profile is described as a zero-mean stationary process and correlation length is the distance where the autocorrelation is $e^{-1} \approx 0.37$. Models typically used for surface scattering are SPM (small perturbation model) [232], POT (physical optics theory) [232] IEM (integral equation model) [67]. The multi-scale surface roughness models [162, 163, 164, 165, 50, 66] are based on the assumption that the RMS height and correlation length are dependent on the measurement length. Natural surfaces are often close to the behavior of

Brownian surfaces, i.e. the correlation length L_c is linearly dependent on the measurement length x, $L_c = k_0 x + b$, where k_0 is a constant, and the logarithm of the RMS height is linearly dependent on the logarithm of x, $\sigma = cx^b$. From these conditions, using commonly used surface correlation functions (e.g. Gaussian, exponential, isotropic exponential, transformed exponential), the backscattering coefficient can be derived using the IEM. These models are, however, valid only for level ice.

Deformed sea ice (ice ridges) has been modeled using randomly oriented circular scatterer blocks [26], or using 3-D cylindrical scatterer blocks [29] and dihedrals [161]. Typically applicable wavelengths for these block models are significantly less than the dimension of the scatterer blocks. The volume scattering is usually modeled using radiation transfer theory, i.e. transportation of energy through a medium containing particles, and iterative and numerical methods. Wave theory based on Maxwell's equations is too complicated. Typically for co-polarized SAR only single scattering is considered, and multiple scattering is more significant for the cross-polarized case. Volume scattering modeling is important in the arctic areas where multi-year ice exist. Also some inversion models have been developed for the sea ice. A simple inversion model for the Baltic Sea ice was presented in [25]. An overview of inversion techniques for sea ice backscattering can be found in [73].

We have been able to make only some relative comparisons to scattering models and scatterometer results because we do not have absolutely calibrated Radarsat-1 data. However, it is possible to get useful information about the order of the backscattering signatures from these models. The scatterometer results for the Baltic Sea ice we have used have been measured by the HUTSCAT (Helsinki University of Technology Scatterometer) [84] which is a helicopter-borne non-imaging scatterometer having two bands (C at 5.4 GHz and X at 9.8 GHz) and all four polarization combinations. The instrument has been developed at HUT Laboratory of Space Technology (LST). The incidence angle can be adjusted between 0 and 45 degrees. We have utilized the C-band HH-polarized measurements of the instrument [152, 153, 155]. The instrument is equipped with a video camera which records the flight line. This video data is then used for visual ice type classification and based on this information e.g. backscattering distributions for sea ice classes can be computed. Scatterometer measurement based Baltic Sea ice class distributions for C-band HH-polarization and for incidence angles of 23 and 45 degrees are shown in Fig. 2.7.

We have made some relative comparisons to the Baltic Sea ice model results [26, 163] and the scatterometer results of HUT LST [153, 155]. These comparisons have been useful in defining the ice classes of our algorithms, but no absolute comparison is possible until we have absolutely calibrated data.

2.6 SAR Interferometry

In SAR interferometry the same target area is measured from two slightly different orbits. Based on the phase difference of these two SAR measurements an

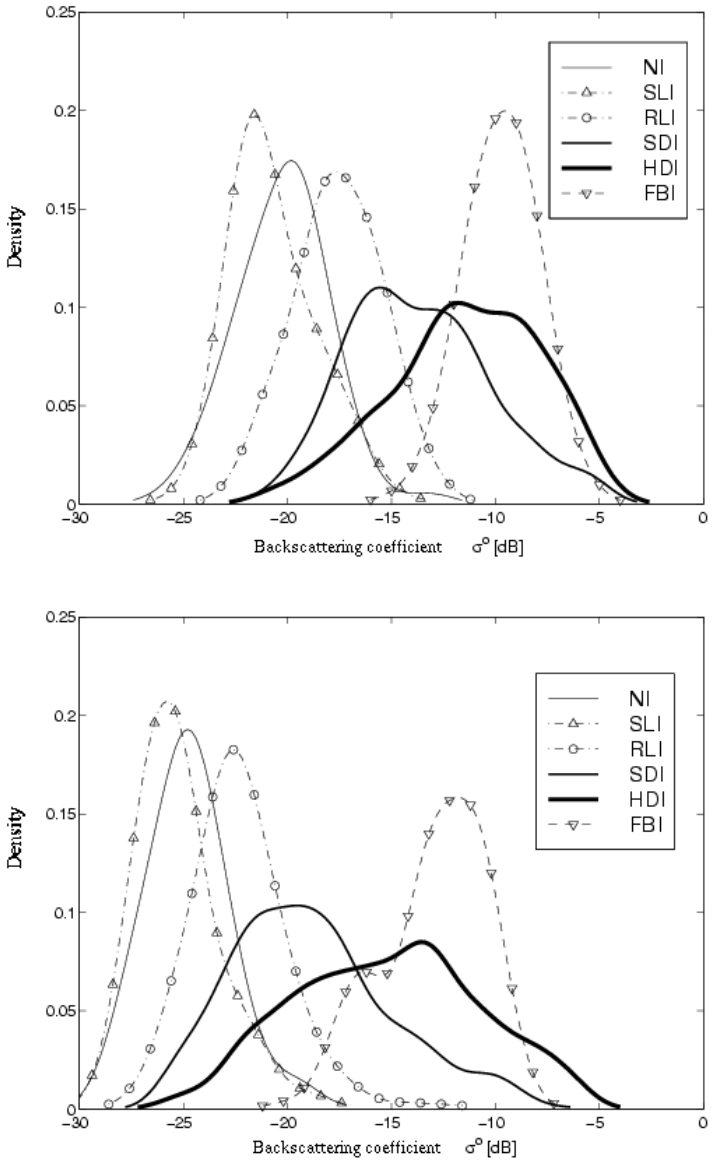

Figure 2.7: Estimated probability density functions of Baltic Sea ice classes based on visual classification and HUTSCAT scatterometer C-band (5.4GHz) HH-polarization measurements [153] for two incidence angles (23 degrees upper, 45 degrees lower) and dry snow conditions. The classes of higher deformation, i.e. deformed ice classes (see Section 2.4, the sea ice classes shown in the figure legends are roughly ordered by increasing deformation from top to bottom), have higher backscattering value, and the backscattering for these classes at different incidence angles differs significantly.

interference image can be computed, and from the interference data a digital elevation model (DEM) of the object area can be formed. This requires very accurate locating of the instrument and the image pixels. Interferometry can be either single-pass, i.e. the instrument has two separate receiving antennas separated by some distance called baseline, or repeat-pass, where the same instrument measures over the same area from different orbits. For repeat-pass interferometry the baseline can be relatively large, making more accurate DEMs possible. SAR Interferometry for the Baltic Sea ice has also been studied in [41] where repeat-pass interferometry using ERS data was applied. A problem with the Baltic Sea ice is that it is difficult to distinguish between the sea ice surface topography and sea ice movement from the interferograms.

2.7 SAR Polarimetry

In SAR instruments the transmitted radiation is plane polarized, either horizontally or vertically. Also the receiving antennas receive either horizontally or vertically polarized radiation. In a fully polarimetric SAR the instrument is capable to transmit and receive both horizontally and vertically polarized radiation. This SAR measurement, containing the amplitude and phase information for HH, HV, VH, and VV combinations of transmitted/received polarization, contains all the necessary polarimetric information, which makes it possible to interpret the scattering mechanisms better.

The current operating instruments, however, only have one polarization combination in their wide swath mode, producing a reasonably large coverage for operational sea ice monitoring. For Radarsat-1, which is our main operational SAR data source, the HH-combination is available. Also the Envisat ASAR instrument of the European Space Agency (ESA) has the same polarization combination in its wide swath mode.

2.8 Sea Ice Data and Delivery to End-Users

Fast delivery of satellite images to ice breakers has been studied and tested by FIMR and VTT since 1985. The test transmissions to ships were based on the mobile phone network (NMT-450, NMT-900) [150]. Also satellite-based communication, using the INMARSAT system was studied. The workstations in use on the ships were developed from the first transmission tests made in 1986 [126] for the tests made in 1989. The images used in the tests were NOAA/AVHRR data. The current data transmission system has been further developed from the system tested then. In the present system the GSM mobile phone network or satellite connection can be used, and there also exist other optional data compression schemes, in addition to the ALP compression already present in the 1989 tests, including JPEG and the wavelet compression scheme developed as part of this work.

After an overflight of Radarsat-1 in a suitable track, the Radarsat-1 data is first received and SAR processing is done by KSAT in Tromsø, Norway. The processed

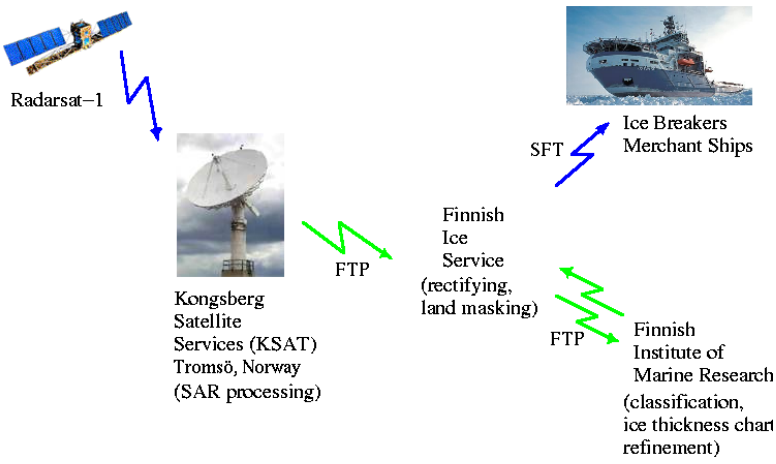

Figure 2.8: The Radarsat-1 data based Baltic Sea ice product chain from Radarsat-1 to end-users. The final products are transmitted to ships by SFT. Air links are blue and earth links green in the figure.

SAR data is then received using FTP at FIS where the data is rectified into a map projection and a land area mask is applied. Then the rectified and land-masked data are sent to FIMR by FTP, where the data are classified produced into data products, which are then sent back to FIS by FTP, and from there to the end-users by a technique called smart file transfer (SFT) developed by the Finnish Research Centre (VTT). SFT is a mobile-based reliable file transfer technology [130]. The whole operational data transmission chain is illustrated in Fig. 2.8. The transmissions between FIMR and FIS are also shown because FIMR and FIS are situated physically apart from each other.

This work mainly describes the part of this operational chain run at FIMR. There are two operational products which are produced automatically at FIMR, the SAR information refined ice thickness chart and the SAR-based sea ice classification. The SAR-refined ice chart uses the latest available digitized ice thickness chart, received from FIS daily, as a starting point and the recently received SAR data to adjust the thickness area boundaries and local thickness values. This process is schematically described if Fig. 2.9. The classification consists of multiple stages, including segmentation and classification based on the backscattering strength (SAR pixel intensity), texture based classification, open water and fast ice detection. As a result a thematic map describing the ice types is produced. The classification scheme is shown in Fig. 2.10. All the separate stages of the classification algorithm are designed to be independent modules which can easily be replaced by new versions. The modules exchange information by ASCII text files and PNM (Netpbm super image format) binary graphics files.

These sea ice products are produced automatically on a Linux server at FIMR and also delivered automatically back to FIS from where they are further sent to end-users. The automation at FIMR has been implemented as a Unix script, which polls the incoming FTP directory to check whether new SAR images have been received from FIS by FTP. If new SAR images have been received the scripts

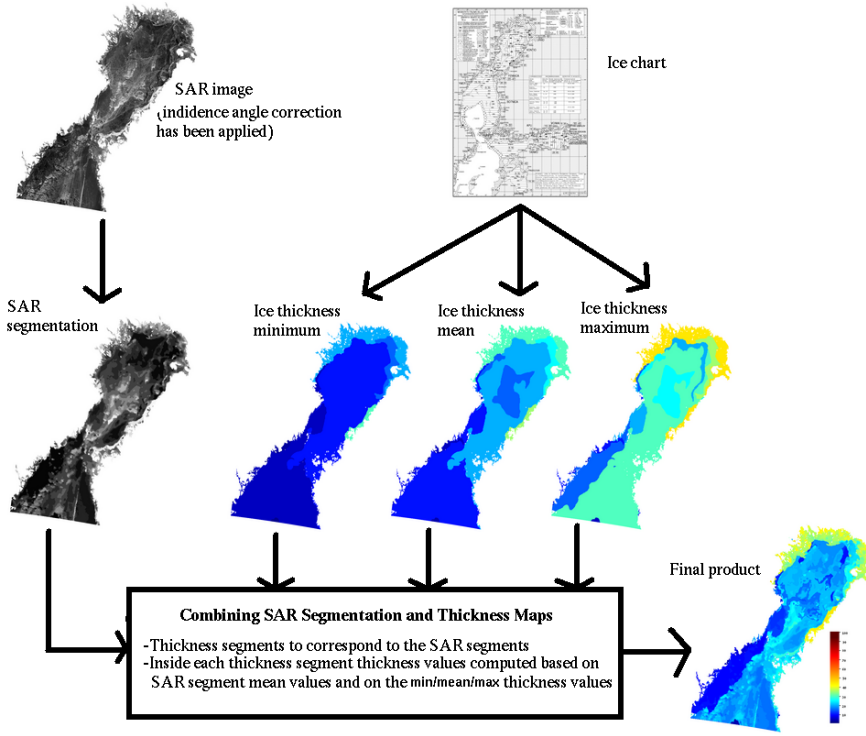

Figure 2.9: Generating SAR-refined ice thickness chart.

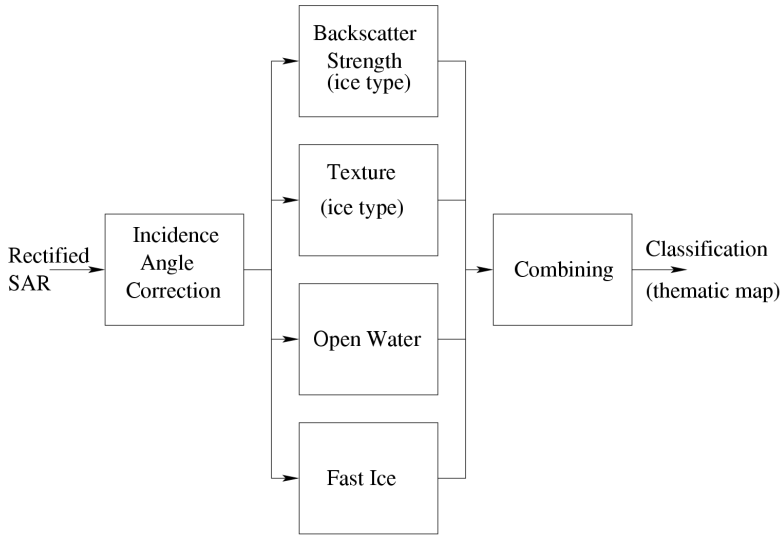

Figure 2.10: The FIMR SAR classification scheme.

producing and sending the end products to FIS are called.

2.9 Evaluation and Validation of SAR-Based Sea Ice Products

Because the Baltic Sea ice is moving and deforming continuously, evaluation and validation based on in-situ measurements is very difficult. The traditional sea ice measuring techniques include measuring ridge heights by hand and ice thickness by drilling. Evaluation and validation of our SAR-based methods would require a large number of such in-situ measurements simultaneously with the SAR data acquisition, which is practically impossible.

The main data sets for evaluation have been the digitized ice thickness charts and ice type charts, and since the winter 2003 we have also had some ice thickness measurements based on helicopter-borne electromagnetic induction sensor (HEM) measurements. Unfortunately these measurements have been concentrated on short periods related to some field experiments, and we only have a few simultaneous Radarsat-1 scenes. However, in the future more HEM data over the Baltic Sea ice will be collected, hopefully also enabling comparisons to our operational data. No funding for separately collecting HEM data for evaluation and validation of the operational Radarsat-1 based algorithms will be available in the near future. A cheaper alternative compared to helicopter flights would be to mount an electromagnetic induction sensor on some ship operating in the Baltic Sea ice, e.g. an ice breaker.

One alternative way is to compare visual interpretation of the SAR data to the automatic SAR classification. Additionally we have used some data measured by a scatterometer operating at the same frequency band as the space-borne instruments. The scatterometer measurements have been compared to visual ice type interpretation from simultaneous video recording [152, 153, 155]. Also some scattering models have been studied and comparisons with sea ice backscattering measurements have been performed [156].

Because making enough simultaneous in-situ measurements with the SAR image acquisition using traditional measuring techniques for validation purposes is practically impossible, advanced automated measuring techniques would be required for validating the SAR-based sea ice algorithms.

Alfred Wegener Institute (AWI) has performed HEM measurements in Gulf of Bothnia and Gulf of Finland in 2003 and 2004. The HEM instrument measures the distance to the water below sea ice based on low-frequency electromagnetic induction from the sea water. Sea ice is typically resistive and water is conductive and electromagnetic induction from the water occurs. The ratio between the measured HEM field (also know as secondary field) and the transmitted (primary) HEM field, depends on the distance between the EM system and the conductive media, and on the electrical conductivity of the media. Main part of the secondary magnetic field comes from the sea water, and the instrument's distance to the sea water can be derived from the measured secondary field strength. Then the ice (plus snow) thickness is the distance to the sea water, measured by the HEM instrument, subtracted by the distance to the surface measured by a laser altimeter included in the instrument. The HEM measurement principle is shown in Fig. 2.11. The HEM instrument and the field measurements made in the Baltic Sea

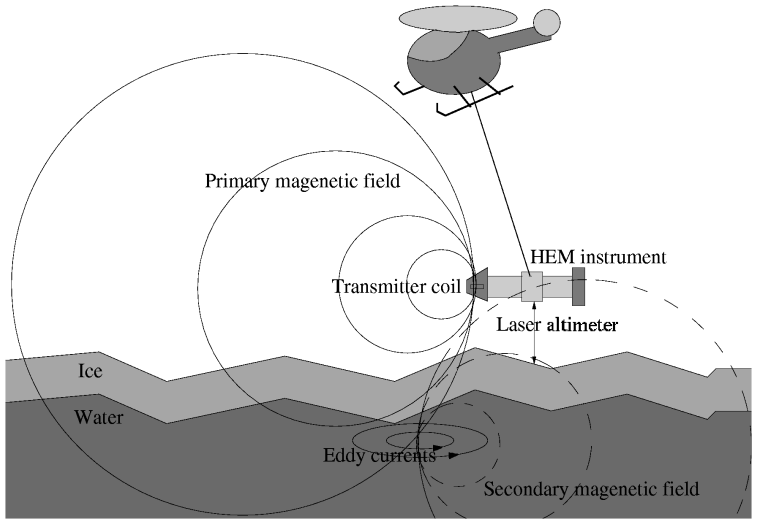

Figure 2.11: The HEM measurement principle.

are described in more detail in references [79, 80, 81].

It has been assessed that for level ice the accuracy of HEM measurements is about 10 cm [79] whereas for ridged ice the accuracy is weaker due to water appearing between ice blocks. However, the occurrence of an ice ridge can almost always be detected.

Chapter 3

Comparison with Earlier Related Works

The compression and classification of SAR data have been widely studied. In many cases the compression of SAR data is, however, performed using methods developed for optical image compression, without taking into account the special nature of SAR data. SAR-based classification and target detection has also been studied a lot. Classification of land areas, e.g. fields and forests, has been studied more widely than classification of sea ice. The ground truth in the land areas is typically more easily available and more stable compared to the dynamic sea ice. The development of sea ice measuring methods has made possible to study the relations between sea ice measurements and SAR signatures and to develop more accurate sea ice algorithms. This section describes the earlier work done in the fields of sea ice SAR compression and classification, especially in the area of the Baltic Sea.

3.1 SAR Compression

The wavelet transform has been applied with great success to numerous image compression problems, see [160]. However, only relatively few articles utilizing transform coding for SAR compression exist. Operational Radarsat-1 data has been compressed using Adaptive Laplacian Pyramid (ALP) compression [151], originally presented by Burt and Adelson [19]. Some recent contributions are [10, 18, 244, 250]. In [244] three different orthogonal wavelet filters were tested in SAR compression, and in [18] wavelet packet type decomposition was used for SAR compression. Baxter [10] used the Gabor transform and utilized in his work results related to the human visual system (HVS) processing. The publication by Zeng and Cumming [250] was published during revision of this work [publication 2]. Their approach relies on the tree-structured wavelet transform, which is closely related to wavelet packet decomposition. Some ideas similar to our approach are presented in [250], e.g., division into homogeneous sets (in our terminology: textureless area)

and target sets (in our terminology: textured area). The approach in [250] also contains several adjustable parameters. We have also noticed that interesting ideas for using the tree structure in the pruning or classification of the wavelet coefficients have been presented in [204]. We at FIMR have studied the use of fractal coding for our sea ice SAR images [109], but the results for the fractal methods tested have not been very convincing.

3.2 SAR Segmentation and Classification

3.2.1 Overview

The previous sections have already shown that sea ice SAR classification is a very difficult task. The classification is dependent on many factors, e.g. on instrument properties and data processing, current weather and weather history. Backscattering from open water can cover the whole dynamic range of the sea ice backscatter, depending on sea waves (wind speed) and local incidence angle. In most cases there is no ground-truth available and visual classification based on either the SAR data or some additional remote sensing instrument measurements is used in place of ground truth. Backscattering from sea ice and open sea at different incidence angles can vary significantly. Direct inter-comparison of classification methods and results is thus impossible, unless exactly the same data sets were in use.

Most of the research in SAR-based sea ice classification has been done for the arctic sea ice, where the distinguishing between open water, first-year ice and multi-year ice is important. Some efforts to classify the Baltic Sea ice have also been made. C-band has been used in most of the classification studies because most of the available operational instruments, like ERS-1 and ERS-2, Radarsat-1 and Envisat ASAR are C-band instruments.

In earlier works typically SAR-backscatter mean and some measure of deviation, typically standard deviation, are used as the features in sea ice SAR classification. These values are computed in a data window around each pixel. According to these earlier works it is clear that ice classes with higher degree of deformation produce higher backscattering but also that most of the sea ice classes have large standard deviations and overlap each other. The measure of deviation is typically used as a measure of texture. Such window based methods perform a low-pass filtering and reduce the output resolution. Applying segmentation, such as in our method, and computing segment-wise features reduces the low-pass filtering effect and also reduces the class overlapping because the class boundaries are better taken into account.

3.2.2 Methods Based on First-Order Statistics

The basic approach is to use the value of the backscattering coefficient or local backscatter coefficient mean and variance (so-called first-order statistics) for classification. Such studies for the arctic sea ice are made e.g. in [225, 61, 129, 220,

207, 148]. In [147] also locational and meteorological data were utilized in the classification. The result is that first-year ice (FYI) and multi-year ice (MYI) can mostly be distinguished, but the different FYI classes have much overlap and are difficult to distinguish. Also the occasional appearance of frost flowers (about the effect of frost flowers to backscattering see e.g. [237]) in nilas ice makes the distinguishing of nilas ice from other ice types more difficult [225].

Studies utilizing the ERS-1 data have been also been made, especially as part of the Baltic Experiment for ERS-1 (BEERS) [236]. The radar signatures for seven classes were compared during data from three winters (1992-94). The classes were smooth level ice, rough level ice, slightly deformed ice, ridged ice, hummocked ice, rubble field and jammed brash barrier. The backscattering coefficient and texture coefficient [183] were computed for samples of these classes. the results show that in general the backscattering coefficient increases as the ice deformation increases, but the texture coefficient values for most of the classes cover quite a wide range and overlap significantly. Based on assumption of dominant surface backscattering an empirical model for relating backscattering to ice surface roughness and incidence angle was presented for C-band. In [144] the fuzzy C-means algorithm has been applied to ERS data over the Baltic Sea ice using first-order statistics.

3.2.3 Context-Based Methods

Contextual segmentation is based on the magnitude of the backscattering coefficient, also taking into account the context to reduce the effect of speckle. Such approaches include the ICE algorithm [179] utilizing Markov chains after scanning the 2-D image into 1-D signal using the Hilbert-Peano scan. In [46] the classification is based on 4-parameter Pearson's system of distributions and the ICE algorithm. In our algorithm [publication 7] a Gaussian mixture and PCNN were used for contextual classification. This was because experimental studies show that our data in uniform segments are very close to Gaussian data (see, e.g. [publication 6] and [publication 7]).

3.2.4 Texture-Based Methods

Some classification schemes also try to utilize the *texture* in the SAR image. The most typical measure of texture are computed based on the gray-level co-occurrence matrix (GLCM) [87]. GLCM has been used in e.g. in [7, 8, 9, 33, 105, 206, 248]. In [169] the GLCM was compared with standard first order statistics (mean, variance, range) for sea ice classification, and the classification based on standard statistics clearly outperformed GLCM classification. Also Markov random fields (MRF) have been used in texture classification, in [248] and [33] they are compared with GLCM features. In [33] these two texture classification methods are compared to Gabor-filter [60, 68] based texture classification. Based on these studies the Gabor-filter based and GLCM based classification outperform MRF based classification. Still, MRF brings some additional information to the classification and can thus be used in combination with either GLCM features or Gabor features. The results of using texture features in SAR classification are somewhat contradic-

tory: some publications report about improvements in classification using texture features [9, 206] and some do not see any significant improvement [220] [169]. This disagreement can, at least partly, be explained by different data, due to different instrument properties, data processing and ice, snow and weather conditions.

3.2.5 Methods Utilizing Data Fusion

Most of the practical classifiers use other data sources in addition to the SAR data to improve the classification. Two such systems are worth mentioning. First, the ARKTOS classification system, which classifies the sea ice into five categories (MYI, FYI, fast ice, open water/new ice, unknown) using a SAR-based expert system with ancillary data, e.g. land mask SSM/I based satellite data concentration classification, climatology data [89, 223]. Second, the ARTIST classifier [105] using multiple features computed from ERS-2 SAR data and SSM/I data, using the NASA team algorithm [228]. This latter approach uses the Learning Vector Quantization (LVQ) [123] algorithm for training.

3.2.6 Studies Utilizing C-Band SAR Data in Sea Ice Classification

The backscattering from the Baltic Sea ice has been studied in [26] in the sense of modeling and to define which backscattering mechanisms produce the backscatter for level ice and deformed ice. The volume scattering is significant only for level ice, and the surface scattering is the dominant scattering mechanism at C-band for rough level ice and deformed ice. In [162, 163, 164] more precise models based on multi-scale roughness were developed and validated.

Open water and sea ice discrimination in the Baltic Sea has been studied in [209] and [210]. The discrimination problem is formulated using a Gaussian mixture model for backscattering intensity values and the contextual information is based on the Markov Random Field formalism in which the strength of the contextual information is based on the autocorrelation value.

In [147] a large set (over 100) of ERS SAR images from arctic areas were used for studying the separability of sea ice and open water. Additionally also meteorological data (temperature, wind speed) were utilized in the classification. Ground truth was replaced by visual classification of 5 km by 5 km data windows, then SAR backscattering mean and standard deviation in these windows were computed. A multivariate regression analysis was then applied to this SAR statistics complemented with meteorological and locational information. This method gave results comparable to other studies in open water classification.

In [71] a semi-automated sea ice classification method for Radarsat-1 data is presented. It is based on three features computed from the SAR data, power-to-mean ratio, estimated gamma parameter of the gamma distribution and entropy (derived from GLCM), in addition to the pixel amplitude. The classification is based on fuzzy rules, which classify the data into four classes: calm water, turbulent water, low and high concentration sea ice. These four classes are classified differently in

the near range and far range, thus yielding a total of eight classes.

In [148] the derivation of the Baltic Sea ice concentration from Radarsat-1 SAR data was studied, based on local mean backscatter thresholds. The method is similar to the one in [53]. However, using only a method based on thresholding of backscattering coefficients, one does not achieve very good results in open water classification (because of backscatter dependence on sea waves, and also on air temperature history).

The C-band HH-polarization scatterometer data of the Baltic Sea ice is also used in [215], where the posterior distribution of a mixture parameter describing the surface roughness is empirically approximated using Markov Chain Monte Carlo (MCMC) method. These results were compared to video classification. The results were promising and their geophysical interpretation is possible. Also some suggestions to extend the method for 2-D images were given.

In [211] the wavelet transform was utilized to characterize the local statistics typical of different ice deformation categories using ERS SAR data. The distribution of the wavelet coefficients was modeled using the mixture of three normal distributions. The class parameters were estimated applying a stochastic version of the EM-algorithm [30, 31]. The ice classification map was generated using the maximum likelihood classification. An operative sea ice classification system based on ERS-1 data was developed by adding open water identification based on block-wise autocorrelation [212]. The algorithm was made operational in 1995 [76]. It consisted of image rectification, land area masking and generating a classification map. The algorithm was run at FIS each time after receiving of an ERS SAR image. Because of the relatively narrow swath width, about 100 km, of ERS images acquired by ERS-1 (operational in 1991–2000) and ERS-2 (1995–), the ERS-data were not very suitable for practical near-real-time operational use. There also existed some data delivery problems from ERS satellites to ice service. This situation was improved after the launch of Radarsat-1 in 1995. The swath width of the Radarsat-1 ScanSAR Narrow mode images is 300 km, and the swath width of the ScanSAR Wide mode images varies from 440 km to 500 km. An operational SAR classification algorithm was then developed for Radarsat-1 data at FIMR [108, 192], and this algorithm is still in operational use and run for each received Radarsat-1 scene at FIS. The operational Baltic Sea ice SAR classifier, using Radarsat-1 ScanSAR narrow mode images in classification, was made operational in 1998 at FIMR and FIS. This classifier is based on simple experimental incidence angle correction, intensity-based segmentation, and some additional texture features to locate deformed ice and open sea. The algorithm classifies the Baltic Sea ice into open water, three level ice classes, and two deformed ice classes (slightly deformed ice and highly deformed ice), and fast ice. An example of a Radarsat-1 ScanSAR narrow mode SAR image and its classification result are shown in Fig. 3.1. The classification result (a thematic map) is given in 500 m resolution.

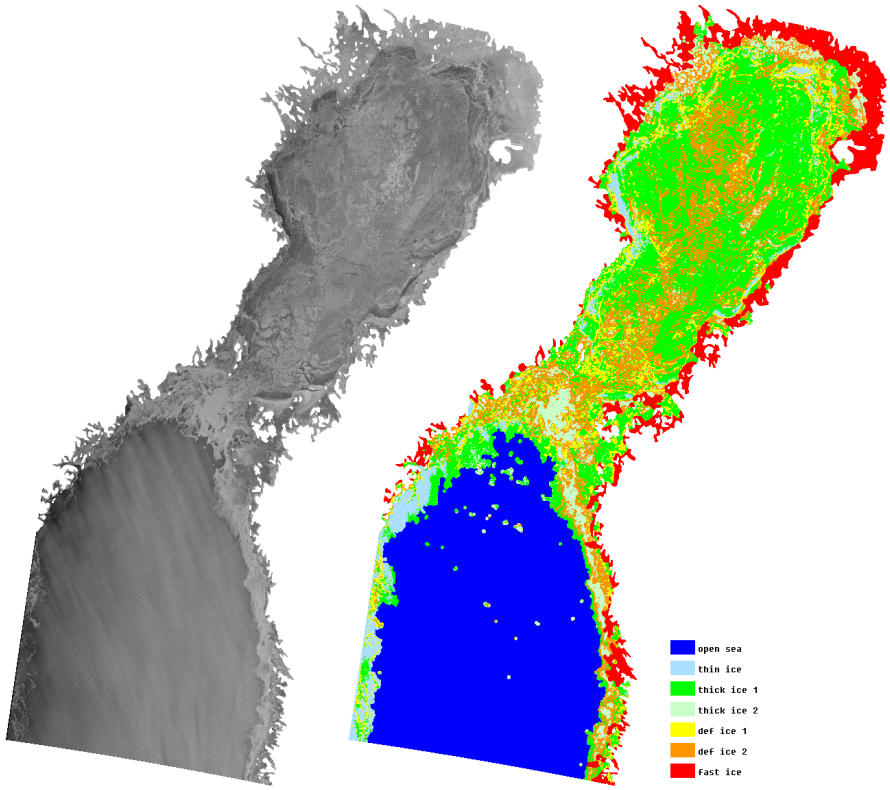

Figure 3.1: A Radarsat-1 ScanSAR wide mode image, Feb 18th 1998, ©Canadian Space Agency (CSA), left, and its classification based on the algorithm of [108].

3.2.7 Studies with Multi-Channel SAR and Scatterometer Data

In [226, 227] sea ice classification capabilities of ERS-1 SAR data over the sea ice in Gulf of Bothnia were studied using airborne and simulated SAR data. The frequency channels were those corresponding to the ERS-1 SAR channels, i.e. C- and X-bands. The best performing of the compared methods was based on segmentation [219] and backscattering mean and texture values (computed as backscatter standard deviation divided by the backscatter mean) in these segments. In a four-class (open water, level ice, rubble fields, brash ice) classification, about 80 % classification accuracy was achieved, compared to visual interpretation of aerial photographs.

Some studies have also been made in the area of the Baltic Sea. The Bothnian Experiment in Preparation for ERS-1 (BEPERS) was performed in 1988. In BEPERS an airborne SAR instrument, whose frequencies and polarizations were similar to the coming ERS-1 frequencies, was used. C-band and X-band data at the four dif-

ferent polarization combinations [138, 139, 140] were collected using the airborne CCRS (Canada Centre for Remote Sensing) SAR. The studies mostly concentrated on X-band data, but the results probably are quite similar for C-band because these two frequency bands are close to each other. The affect of incidence was reported to be quite similar for the studied ice types, indicating that a linear model could be used to model the decrease of the logarithmic backscattering as a function of the incidence angle. Also the potentials of SAR data for sea ice classification were studied. On the basis of the validation the ice was divided into eight categories: open water, bare smooth ice, patchy (ice-snow) level ice, snow-covered ice, frozen uneven ice, old ridges, young ridges and brash ice [120]. Discriminating between open water and undeformed ice, and between brash ice and ridged ice were the most problematic cases. The standard deviations in the classes were typically quite high and also other class pairs had mutual overlap.

In the European Multi-Sensor Airborne Campaign (EMAC) also snow and ice experiments in the Baltic Sea were included, the tests were made in 1995. Fully polarimetric C- and L-band SAR-data were acquired over the Baltic Sea ice using the EMISAR instrument of the Danish Centre for Remote sensing (DCRS) [85, 86, 213, 216]. Also multifrequency scatterometer measurements were made [51]. This experiment compared the use of L- and C-band SAR data in sea ice monitoring, and also the use of polarimetric SAR-data at these channels was studied. Space-borne fully polarimetric SAR instruments do not exist yet, but also multiple polarization combinations and even fully polarimetric modes are available in the future instruments, e.g. in Radarsat-2. It was reported that L-band would potentially give more information about the sea ice, because it penetrates deeper giving more information about the ice volume. Also some new ice areas, which produce high backscattering because of small-scale roughness, can better be distinguished at L-band, and the masking effect of moist snow is weaker at L-band.

In [155] the C-band and X-band signatures based on scatterometer measurements were studied, and compared to a visual classification from simultaneous video recordings. These studies were made for HH- and HV-polarization combinations and for two incidence angle values (23 and 45 degrees), and both dry and wet snow conditions. In this study distributions for six Baltic Sea ice classes are given for calibrated backscattering coefficients, and these distributions can be used as a basis for classifying calibrated data. In [155] the incidence angle dependence of the Radarsat ScanSAR data were studied for the Baltic Sea ice, and incidence angle dependencies for level ice and deformed ice were given. These dependencies can be used to correct the effects of incidence angle e.g. in classification.

Repeat-pass SAR interferometry for the Baltic Sea ice has been studied [41], but because of the ice movement and deformation, it is impossible to generate a realistic surface elevation model. Fully polarimetric classification of sea ice has also been studied, e.g. in [136, 194, 195, 196, 197, 198, 202], based both on airborne and some space-borne test instruments. However, currently there does not exist any fully polarimetric space-borne instruments suitable for operational sea ice classification. The Radarsat-2 SAR will have dual polarization mode (one co-polarized and one cross-polarized channel) in its wide swath and ScanSAR modes. Unfortunately the use of dual-polarization for sea ice classification has not been studied very much. In [173] a sea ice classification study for dual-polarization at Ku-band

is presented, and in [199, 200, 201] possibilities to use C-band dual-polarized SAR-data in sea ice classification are studied. These C-band studies are made to prepare for Radarsat-2. The data used in the experiments has been Envisat ASAR alternating polarization (APP) mode data. Unfortunately the ASAR APP image areas are too small for typical operational sea ice monitoring. Based on the studies it seems that using dual-polarization, i.e. adding information from a cross-polarized channel to the co-polarized channel information, slightly improves the sea ice classification. Using fully polarimetric information further improves the classification giving more detailed information about the scattering mechanisms from the sea ice.

3.2.8 Application of Independent Component Analysis to Feature Detection

Classification of optical images based on independent component analysis (ICA) has been studied e.g. in [131, 137, 102]. The basic idea is to use image data windows to generate a set or sets of typical basis vectors, or filters, for the training data. Then this set of basis vectors (or filters) is used in the analysis of the image data. For natural (optical) images the resulting basis vectors correspond to edge filters [172], but for images containing only some specific features, e.g. for textures, very specific basis vectors describing the training data, can be generated by ICA [102, 131]. As a result, images or image windows can be classified based on how they are projected on the ICA basis vectors.

In [102] some Brodatz textures [16] are classified based on ICA, and also compared to use of Gabor filters. In [131] the ICA-based classification is compared to classification based on a PCA basis. These results show that ICA-based classification, with large enough number of filters (basis vectors), outperforms Gabor-based and PCA-based classification. Also [137] shows that ICA-based classification can improve the classification accuracy compared to standard Gaussian mixture models.

ICA has also been applied to multichannel SAR data. Computing the independent channel components, which are linear combinations of the original channel images, have been used to improve visual and automated data interpretation, e.g. in [62].

Chapter 4

Data Preprocessing

Some preprocessing steps are typically required before utilizing the SAR data in operational products. The preprocessing at FIMR consists of three stages: (1) SAR image rectification into a suitable map projection compatible with the information system used by the end-users, (2) incidence angle correction and, possibly, (3) some kind of a speckle filtering. Also re-sampling to some lower resolution before delivering the data to end-users can be done, but the re-sampling procedure is straightforward and not discussed here.

4.1 SAR Image Rectification

The image measured by the instrument is in the coordinate system where the columns coincide with the azimuth directions, and each row contains the evenly-spaced measurements in slant range, see (Fig. 2.2). For utilization of the data it is necessary to convert this measuring instrument specific imaging geometry to some map projection.

Usually the image is first converted into the latitude-longitude projection. This can be done based on the 3-D geometry, i.e. each pixel is first converted to the Cartesian 3-D coordinate system, where the origin is located at the center of the earth ellipsoid, and the coordinates are denoted by the vector (x, y, z). The coordinates in the latitude-longitude coordinate system are denoted by (latitude,longitude)=(ϕ_E, θ_E). For the earth surface an ellipsoid model is used in the sea areas. In the land areas, due to local altitude variations, an elevation model describing the terrain is typically used to improve the mapping. For images covering relatively small areas, a locally spherical earth model can be used. In the spherical model the local earth radius R_{ref} computed from the ellipsoidal earth model is used as the radius of the sphere. The ellipsoid parameters are the major axis (x-axis) radius a_e, the minor axis (y-axis) radius b_e, the ellipsoid flattening $f_e = \frac{a_e - b_e}{a_e}$, and the ellipsoid eccentricity $e_e = \sqrt{2f_e - {f_e}^2}$. The local earth radius at latitude ϕ_E can be defined from

the ellipsoid parameters a_e and b_e:

$$R_{\text{ref}} = \sqrt{\frac{b_e^2 \cos^2(\phi_E) + a_e^2 \sin^2(\phi_E)}{a_e^2 b_e^2}}. \tag{4.1}$$

The (x, y, z)-coordinate system origin is located at the center of the sphere, the x-axis is from west to east, y-axis is from south to north, and the z-axis is perpendicular to x- and y-axes. The conversion from latitude-longitude (ϕ_E,θ_E) coordinate system can in this simple model be written as

$$(x, y, z) = (R_{\text{ref}} \cos(\phi_E) \sin(\theta_E), R_{\text{ref}} \sin(\phi_E), R_{\text{ref}} \cos(\phi_E) \cos(\theta_E)), \tag{4.2}$$

and the inverse relation can be derived from equation (4.2).

We use the Mercator projection [157] as our map projection. The Mercator projection is a cylindrical projection which makes meridians straight lines. The scaling is correct at the reference latitude ϕ_{ref}, at which the projection is computed. Typically the equator (0^o) is used as the reference latitude. However, we use the reference latitude $\phi_{\text{ref}} = 61^o 40'$, which is more suitable for the Baltic Sea, and the scale distortion is not very noticeable. The conversion from latitude-longitude grid to the Mercator projection, i.e. to the Mercator easting and northing coordinate values x_m and y_m, can be performed using the equations

$$k_0 = \frac{\cos \phi_{\text{ref}}}{\sqrt{1 - e_e^2 \sin^2 \phi_{\text{ref}}}}, \tag{4.3}$$

$$x_m = a_e k_0 \phi_E, \tag{4.4}$$

$$y_m = a_e k_0 \ln \left(\tan \left(\frac{\pi}{4} + \frac{\phi_E}{2} \right) \left(\frac{1 - e_e \sin \phi_E}{1 + e_e \sin \phi_E} \right)^{e_e/2} \right), \tag{4.5}$$

where k_0 is a scaling factor dependent on the reference latitude. We use the Hayford ellipsoid with $a_e = 6378388.000$ m and $b_e = 6356911.946$ m as our reference ellipsoid. For the more recently defined WGS84 ellipsoid, which is used in many maps today, $a_e = 6378137.000$ m and $b_e = 6356752.314$ m.

The inverse for the Mercator easting, x_m, is obvious, but the Mercator northing, y_m, for an ellipsoid model does not have a closed form inverse. However, a serial expansion can be used to compute the latitude approximately:

$$\begin{aligned} \phi_E \approx & \left(\frac{1}{2} {e_e}^2 + \frac{5}{24} {e_e}^4 + \frac{1}{12} {e_e}^6 + \frac{13}{360} {e_e}^8 \right) \sin(2\tau) + \\ & \left(\frac{7}{48} {e_e}^4 + \frac{29}{240} {e_e}^6 + \frac{811}{11520} {e_e}^8 \right) \sin(4\tau) + \\ & \left(\frac{7}{120} {e_e}^6 + \frac{81}{1120} {e_e}^8 \right) \sin(6\tau) + \\ & \left(\frac{4279}{161280} {e_e}^8 \right) \sin(8\tau), \end{aligned}$$

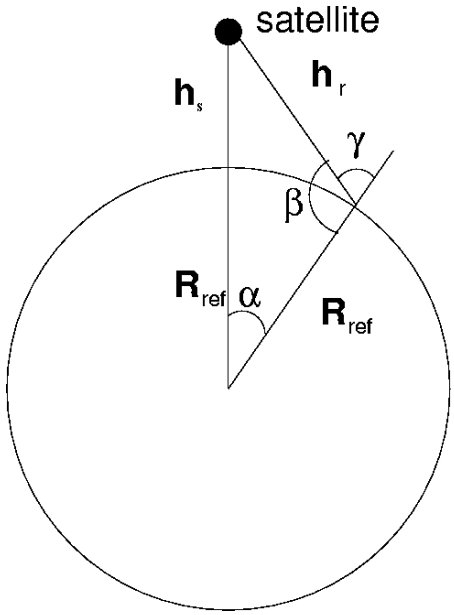

Figure 4.1: Range geometry of the spherical earth model.

where $\tau = \frac{\pi}{2} + -2\arctan\left(\exp\left(-\frac{y_m}{a_e k_0}\right)\right)$.

We first re-sample the image into a grid corresponding to the minimum resolution of the input image (the resolution varies depending on the pixel location), and then it can be down-sampled to the desired resolution applying a suitable low-pass filter. In re-sampling from projection to another we use bilinear interpolation.

The local incidence angle γ, which is required in our computations, can be computed from the geometry of Fig. 4.1, by using the local radius R_{ref} at the reference latitude as the spherical earth model radius. Based on the law of cosines we have

$$\cos\beta = \frac{{h_r}^2 + {R_{\text{ref}}}^2 - (R_{\text{ref}} + h_s)^2}{2h_r R_{\text{ref}}} \tag{4.6}$$

and

$$\gamma = \pi - \beta. \tag{4.7}$$

The satellite height h_s from the earth surface and the distance h_r from the location of the measurement can be derived from the satellite track parameters, or are included in the processed SAR data headers. These local incidence angle values are used e.g. in correcting (normalizing) the effect of the incidence angle variation over SAR images. The rectification geometry and methodology for our data is described in more detail in [90].

4.2 Incidence Angle Correction

The backscattering at different incidence angles from different targets varies and, because of the wide incidence angle range of Radarsat-1 ScanSAR data (20–50 degrees), the incidence angle effect to the backscattering must be taken into account in sea ice classification algorithms using this data. Our approach is to correct the SAR pixel values to correspond to a single incidence angle value. Another approach would be to use incidence angle dependent parameters in the classification. Radarsat-1 ScanSAR images have different modes. First, there are ScanSAR wide and ScanSAR narrow modes. In ScanSAR narrow mode the swath width (image size in ground range direction) is narrower (about 300 km) than for ScanSAR wide images (about 500 km). Both ScanSAR narrow and ScanSAR wide images are further divided into A and B modes, which have different incidence angle ranges. This means that there exist four Radarsat-1 ScanSAR modes, ScanSAR narrow A (SNA), ScanSAR narrow B (SNB), ScanSAR wide A (SWA) and ScanSAR wide B (SWB) modes. The corresponding incidence angles are 20.00–39.55 for SNA, 30.81–46.58 for SNB, 20.00–49.42 for SWA and 20.00–46.58 for SWB [180].

The results in [154] indicate that the decrease of the backscattering is a function of the incidence angle difference and can be modeled in logarithmic (dB) scale by using a linear fit. The performed analysis yielded the slopes of -0.25 dB/degree and -0.21 dB/degree for level ice and deformed ice, respectively. Using this knowledge, the ScanSAR narrow SNA images are normalized to the fixed angle of 29 degrees, the ScanSAR narrow mode SNB images to the fixed angle of 38 degrees, and both the ScanSAR wide image modes (SWA and SWB) to 35 degrees. These values are roughly in the middle of the angle intervals of the ScanSAR narrow SNA and SNB modes and ScanSAR wide mode, thus minimizing the average angle difference. To utilize this different behavior for level ice and deformed ice, a rough classification into these two classes is included in the incidence angle correction algorithm. The classification into the two classes (level ice and deformed ice) is performed iteratively in parallel with the normalization.

The iterative incidence angle normalization algorithm consists of an initialization phase and an iteration phase. In the initialization phase, the decision boundary between the two classes is determined by applying a linear discriminant in a two-dimensional feature space. We use an 11×11 pixel square data window around each pixel for computing two features i.e. mean and standard deviation. The marginal distributions of the logarithmically scaled pixel values in the Radarsat images, for which the estimated value for equivalent number of looks (ENL) varies from 6 to 8 [154], are mostly Gaussian or nearly Gaussian. Hence, the mean and standard deviation are independent, leading to thresholding either of these values by using the linear discriminant. In our discrimination method the direction of the linear discriminant is perpendicular to the first principal component (PC) in the feature space. We first compute the projections of the feature vectors to the first PC vector. Then the initial class boundary is obtained by thresholding the histogram of these projections. Currently we are using an initialization that linearly divides the pixels evenly between the classes in the direction perpendicular to the first PC, see Fig. 4.2. Thresholding either mean or standard deviation did not lead to satisfactory results for our purposes, however. Using window sample mean μ, and

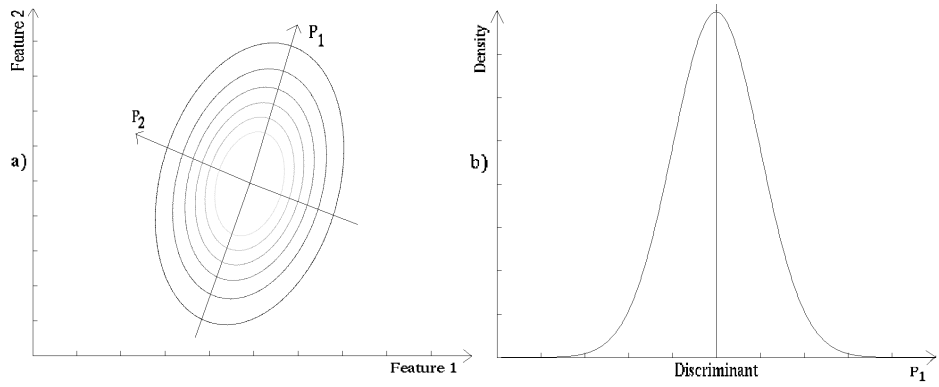

Figure 4.2: A simple example of a contour plot of a correlated 2-D distribution, and axes drawn along its principal components P_1 and P_2 (a). The initial division into two classes is performed perpendicular to the P_1-axis, in this case actually along the P_2-axis because the distributions are symmetric. The discriminant along the P_2-axis is defined from the distribution projected on the P_1-axis (b).

window sample mean multiplied by window sample standard deviation $\mu\sigma$ yielded better results, and we selected to use these features in our algorithm.

We have also studied some alternatives to the current PC approach. Projections to the independent components (ICs) defined by the independent component analysis (ICA) [98] were tested as a substitute to PCs, but it seems that in this case the ICs are typically close to the PCs. We have also tested several algorithms for finding an ideal initial discriminant from the histogram of the features. We have tested the Otsu algorithm [174] and the Expectation-Maximization (EM) and Stochastic Expectation-Maximization (SEM) algorithms [31]. In the last two algorithms the data is modeled as a mixture of two normal distributions. However, the shape of the histogram of the projections is usually not bimodal. Hence, these algorithms often yield unsatisfactory results, e.g., it can happen that only a small proportion of the pixels is allocated to another of the initial classes. Consequently, this leads to a situation where all the pixels are classified to one class after some iterations, even when both classes actually are present in the image, as usually is the case. The current division into halves avoids such anomalies. However, the question of an optimal initial threshold is still open and under research.

The iteration phase consists of normalizing the image using the class dependent slopes and then reclassifying the pixels according to the Bayes rule. Probability density functions (PDFs) for both classes in the 2-D feature space are estimated using a Gaussian kernel estimate, and these PDFs are then used to classify the pixels. According to the Bayes rule the class of a pixel with a feature vector x is the one maximizing

$$\Pi_k(x) = \hat{p}_k \hat{f}_k(x), \quad k = 1, 2 \tag{4.8}$$

over classes k. $\hat{p}_k$ is the estimated prior probability of the class k and $\hat{f}_k(x)$ is the estimated PDF of the class.

The value of the kernel estimate of PDF at point x depends essentially only on the values near the point in question. We write y for intensity values corrected according to the level ice slope value (class 1) and z for intensity values corrected according to the deformed ice slope value (class 2). The operation of computing the feature vector $(\mu, \mu\sigma)$ from the data window x is denoted by $F(x)$. Let us assume that the number of partly overlapping windows belonging to the classes 1 and 2 are n_1 and n_2, respectively. Then the Bayes rule for the window x is: select class 1 if $r(x) \geq 1$, otherwise class 2, where

$$r(x) = \frac{\sum_{i=1}^{n_1} K_G((F(x) - F(y_i))/h)}{\sum_{i=1}^{n_2} K_G((F(x) - F(z_i))/h)}. \tag{4.9}$$

The kernel $K_G(x, y)$ is a product of two one-dimensional Gaussian kernels:

$$K_G(x, y) = \frac{1}{2\pi} e^{\frac{-(x-x_0)^2-(y-y_0)^2}{2h^2}}. \tag{4.10}$$

(x_0, y_0) is the center of the kernel and the smoothing parameter $h = 2$ is common for both features. The kernel is scaled such that it integrates to one. This smoothing kernel was used because of its simplicity. Actually the features are correlated and a kernel including the covariance should rather have been used.

We scaled both features onto the same interval $[0, 255]$. Because the behavior of a kernel estimate depends crucially on the smoothing parameter used, we also tested parameter values $h = 1$ and $h = 4$, but the classification result did not change much. Only about 2% of the pixel classifications differed in comparison between kernels with $h = 1$ and $h = 4$. Using a narrower kernel only changes some minor details in the classification. The bandwidth values larger than $h = 4$ were in our application impractical due to the heavy computational work load in these cases. The decision rule in Eq. (4.9) has some similarity to the majority vote filtering. In the latter approach, all pixels have the same weight whereas in Eq. (4.9) the weights are exponentially decaying.

The incidence angle normalization algorithm proceeds as follows:

1. Initialize classification based on the linear discriminant.
2. Normalize the image based on the previous classification.
3. Perform the classification in the 2-dimensional feature space according to the Bayes rule.
4. If less than a given number of class changes occur or maximum allowed number of iterations has been reached, stop, else go back to step 2.

In practice the classification is performed in steps of half of the window size. An example of the processing can be seen in Fig. 4.3. In Fig. 4.4 the effect of the incidence angle correction on classification can be seen. On the left side of the figure are classifications of two successive SAR images acquired from different flight directions and having different incidence angles in corresponding image locations.

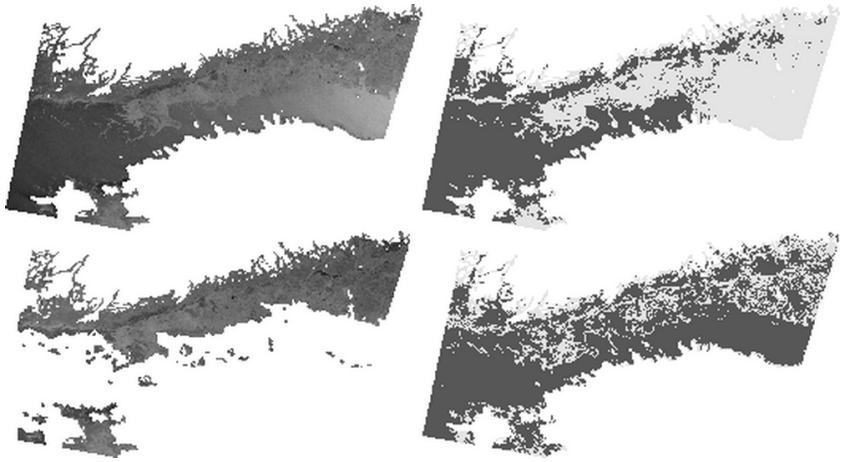

Figure 4.3: A ScanSAR narrow mode SAR image, acquired on Feb 27th 1999 over Gulf of Finland, (©Canadian Space Agency (CSA), upper left), and after incidence angle correction (lower left). On the right are the classification into level ice and deformed ice in the beginning of the iteration (upper) and after the iteration (lower). The open water has been masked off in the incidence angle corrected SAR image (lower left), the correction does not work for open water areas.

The ice fields had not changed much between the images, however the classifications differ significantly. After the incidence angle correction (images on the right) the classifications are more alike. An example of mean SAR pixel values over the incidence angle range of two sea ice SAR images is shown in Fig. 4.5.

4.3 Speckle Filtering

We have tested several speckle filtering methods for our data at FIMR [118]. We have found a method based on anisotropic diffusion useful for our purposes. Here the method is shortly discussed and comparisons to some other methods presented.

The anisotropic diffusion filtering [178] encourages intra-region filtering and inhibits inter-region filtering. Its mathematical formula is

$$\frac{\partial I(x,y,t)}{\partial t} = \nabla \cdot (c(x,y,t)\nabla I(x,y,t)) \tag{4.11}$$

$I(x,y,t)$ refers to the intensity at location (x,y) at time instant t, $c(x,y,t)$ is the diffusion function, monotonically decreasing with the image gradient magnitude. We have used the function

$$c(I,x,y,t) = \exp\left(-\left(\frac{|\nabla I(x,y,t)|}{\kappa}\right)^2\right), \tag{4.12}$$

where κ is an adjustable parameter. The algorithm is implemented as an iteration with constant time increment for each iteration. The method is originated from

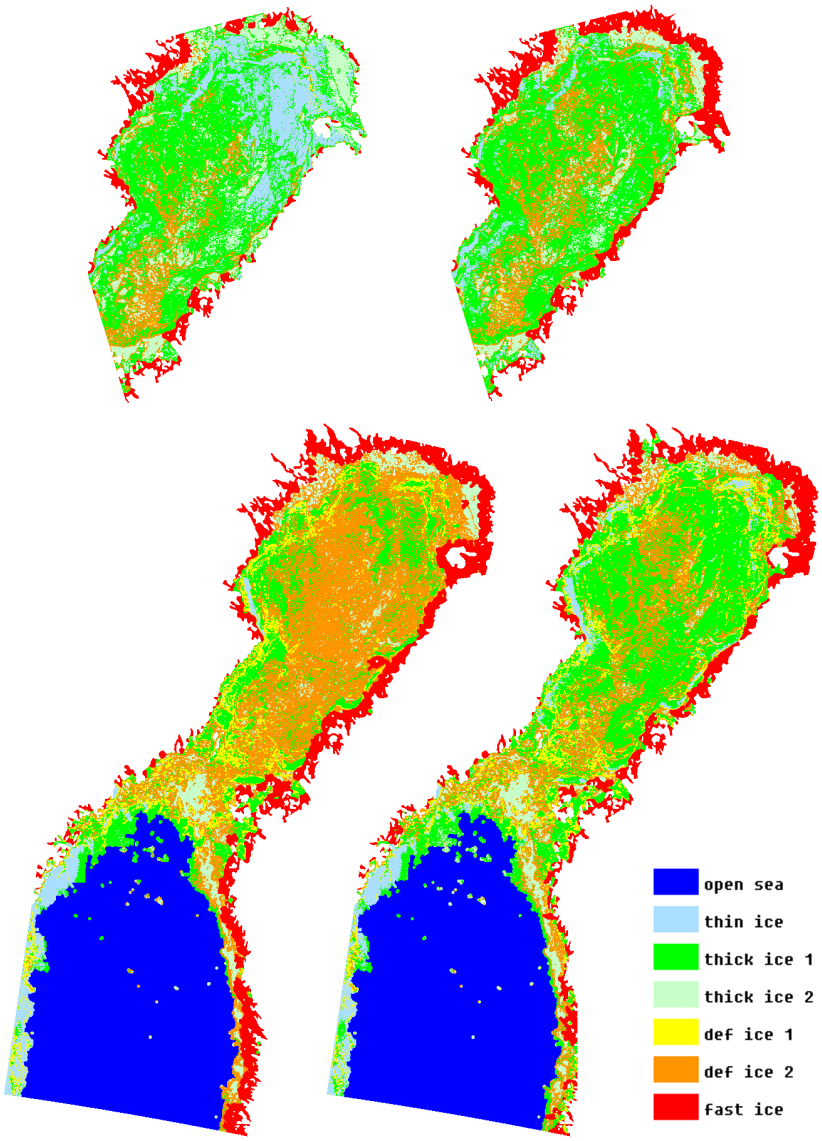

Figure 4.4: An example of the effect of the incidence angle correction on the classification. Two SAR image classifications from adjacent days without incidence angle correction (left side), and with incidence angle correction (right). It can be seen that the classifications of the corresponding image areas of the incidence angle corrected images match each other much better than in the uncorrected versions. There was not much changes in the ice situation between the images. The classification was performed using the algorithm presented in [108].

the principle of heat flow in media. The change of $I(x, y, t)$ is described by the

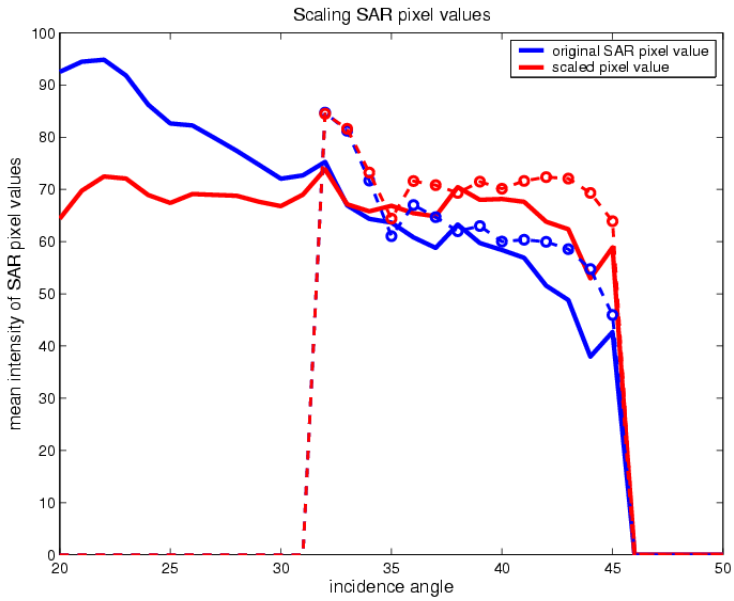

Figure 4.5: Effect of the incidence angle correction for two SAR images, the curves for the two images are drawn with solid line for one image and with dashed lines for the other. The pixel mean values for the different incidence angles (blue) and corrected values (red).

flow Φ, which is the change rate of $I(x, y, t)$ i.e. time derivative of $I(x, y, t)$ and approximated as a difference in the discrete version. In the practical implementation the intensity value $I(x, y, t)$ is iteratively updated in the 8-neighborhood of each pixel as

$$I(x, y, t + \Delta t) \approx I(x, y, t) + \Delta t[\Phi_e + \Phi_w + \Phi_n + \Phi_s + \frac{1}{\sqrt{2}}(\Phi_{ne} + \Phi_{nw} + \Phi_{se} + \Phi_{sw})],$$

where Δt is the time step and Φs are flows from each neighbor, the sub-indices referring to the neighbor location relational to the pixel. These directional flows are proportional to the pixel value difference between the mid-pixel and the neighbor pixel in each direction, respectively. In anisotropic diffusion the amount of the flow is adjusted by the function $c_1(x, y, t)$, and is thus restricted more from directions determined by higher gradients and less from directions determined by lower gradients.

By selecting κ equal to the average gradient produced by noise, the anisotropic diffusion filtering performs a noise reduction filtering. For our data we found that the mean absolute gradient values are around 7 for homogeneous areas i.e. noise. For rough scenes the gradient mean absolute values are higher, typically in the range 10–13. However, the signal-to-noise ratio for our data is quite low, and we experimentally found that the values $\kappa^2 \in [20–30]$ work better for our data than $\kappa^2 \approx 49$ suggested by the theory. A suitable number of iterations for our purposes,

taking into account the execution time limitations in some applications, is about 10.

There are still some slight small-scale fluctuations left in the uniform image areas after anisotropic diffusion. These can be reduced e.g. by running a one-pass median filter, using a 3×3 window for median computation. We also tested some other post-filtering methods after the anisotropic diffusion. One alternative is to use a filter which was designed for smoothing single pixels deviating more than a given threshold from the pixels of their 8-neighborhood. If the minimum difference between the pixel's value and any of its neighborhood pixels is more than the threshold, the pixel is set to the nearest neighbor value, else it is set to the mean of the pixel and its two nearest neighbor values. This algorithm is applied iteratively, for some iterations until convergence, or stopped after a maximum number of allowed iterations.

Because anisotropic diffusion tends to compress the image dynamics, we finally remap the filtered image pixels based on the original image pixel values. In this mapping, for each different pixel value in the filtered image, the mean of the original image pixel values corresponding to those pixel locations, are computed, and the filtered image pixel values are replaced by the mean. Instead of mean e.g. mode or median can also be used.

In order to evaluate the effect of the filtering, we computed statistics based on locating of edges from the original speckled test images and from the filtered images [118]. This was done because the main information, in addition to the intensity value, in the Baltic Sea ice SAR images is the location of the edges. Most of the small edges, i.e. edges whose size in pixels is less than a given threshold T_e, are more likely due to the speckle than larger detected edge segments. We used the value of threshold $T_e = 10$, and the Canny edge detection algorithm [21] for detecting the edges.

For each filtering method we computed five values describing the reduction and preservation of edges in the filtered image. These values are: ρ, the number of edges in the filtered image divided by the number of edges in the original image; ρ_1, portion of the filtered image small edges which are edges in the original image; ρ_2, portion in the filtered image larger edge segments which are edges in the original image. Similar values ρ_3 and ρ_4 were calculated for the original image relative to the filtered image. A good filtering algorithm prunes the edges compared to the original images, i.e. $\rho < 1$, but not all of the edges, i.e. for an image containing edges ρ must be above zero depending on the amount of true edges. Also the edges in the filtered images should correspond to the edges in the original images, i.e. ρ_1 and ρ_2 are closer to one than zero, and more of the small edges are pruned than the larger edges, i.e. $\rho_3 < \rho_4$. These values for the tested filtering methods are tabulated in Table 4.1.

For the median filtered image ρ is small and too many edges are pruned. For the segment mean image ρ is large and too many edges are located. The other algorithms seem to work better, the anisotropic diffusion prunes most (about 99%) of the small edges in the original image, and preserves about 30% of the larger ones.

Table 4.1: Edge statistics comparing the edges in the original and filtered images. References to literature are after the filter names in the first column.

Method	ρ	ρ_1	ρ_2	ρ_3	ρ_4
Kuan [125]	0.339	0.998	0.996	0.0208	0.402
Lee [134]	0.357	0.996	0.885	0.0302	0.383
Segment mean	1.429	0.474	0.532	0.463	0.815
Median	0.0924	0.953	0.955	0.001	0.106
SNN [88]	0.231	0.945	0.773	0.037	0.221
Anisot. diff. [178]	0.283	0.853	0.907	0.011	0.302
Wavelet [55]	0.440	0.751	0.826	0.050	0.417
Kuwahara [128]	0.240	0.848	0.895	0.027	0.249
Gamma MAP [146]	0.762	0.934	0.826	0.577	0.764

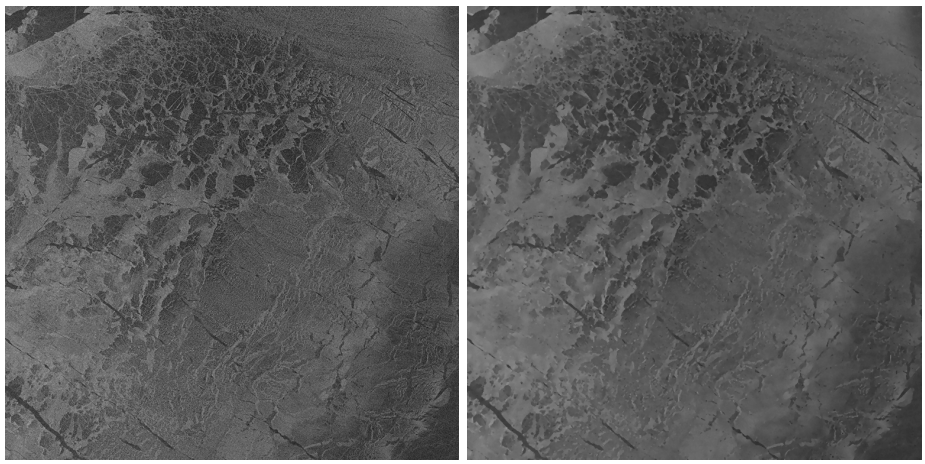

Figure 4.6: A test SAR image (©Canadian Space Agency (CSA), left). Anisotropic diffusion filtering of the test SAR image (right).

We also performed visual inspection of the filtered images and edge images, and noticed that the wavelet filtering causes some artifacts due to the ringing effect near edges. The enhanced Lee filter and the Kuan filter preserve some very small details, some of which may be due to the speckle. After SNN filtering there are still visible fluctuations in areas which in visual interpretation consist of random noise. The noise is suppressed, however. Median filtering and Kuwahara filtering seem to smooth too much. For our purposes, we found the anisotropic diffusion filtering the most suitable of these methods. In Fig. 4.6 an original test SAR image and the speckle-filtered image using the anisotropic diffusion based algorithm described above are shown.

Chapter 5

Wavelet-Based Compression of Baltic Sea Ice SAR Images

This section describes the wavelet-based algorithm designed for compressing Radarsat-1 ScanSAR data for transmission and visual inspection. High compression ratio is necessary because the SAR images are large and bandwidths to end-users on ships are restricted. The contents of this section extend that of Publication 2. The first two subsections describe the wavelet transform and arithmetic coding in general and in the following subsections the implemented coding method is described in detail.

5.1 Wavelets

According to the Heisenberg uncertainty principle [229] it is impossible to obtain exact information on which frequencies exist at a certain spatial location (or time in the case of signals in time). If we denote the spatial (or time) spread around a center spatial location (time) by σ_t and frequency spread around the center frequency by σ_f the Heisenberg inequity can be written as [160]:

$$\sigma_t{}^2 \sigma_f{}^2 \geq \frac{1}{4}. \tag{5.1}$$

In wavelet analysis the spatial (time) resolution increases as the frequency increases, and as the frequency decreases the spatial resolution also decreases. This is unlike in e.g. short-time Fourier analysis, where a fixed-size spatial window is used to compute the local frequency distributions.

The continuous wavelet transform (CWT) for a continuous signal $x(t)$ is defined as

$$CWT\{x(t)\} = X(a,b) = \frac{1}{\sqrt{a}} \int_{-\infty}^{\infty} x(t) W\left(\frac{t-b}{a}\right) dt, \tag{5.2}$$

where a is a scaling parameter and b is a shift parameter. The analyzing function, $W(t)$, is a short oscillatory function, wavelet. CWT can be thought as an inner

product of the original signal with scaled and shifted versions of the wavelet basis function $W(t)$. The scaling and shifting variables are discretized such that the wavelet coefficients can be described by two integers, here denoted by m and n, and then the discrete wavelet transform (DWT) can be written as

$$DWT\{x(t)\} = X(m,n) = \frac{1}{\sqrt{a_0^m}} \sum_{k=0}^{N-1} x(k) W\left(a_0^{-m} k - n\right). \tag{5.3}$$

N is the length of the discretized sequence. In practice usually the value $a_0 = 2$ is used and this is called the dyadic scale. A commonly used technique for the discrete wavelet transform is to use two half-band finite impulse response (FIR) filters, i.e. a low-pass and a high-pass filter in an iterative manner. The relations between the low-pass filter h_0 and the scaling function $\phi(t)$ can be written as

$$\phi(t) = 2 \sum_{k=0}^{N-1} h_0(k) \phi(2t - k), \tag{5.4}$$

and between the high-pass filter $g_0(t)$ and the wavelet function $W(t)$

$$W(t) = 2 \sum_{k=0}^{N-1} g_0(k) \phi(2t - k). \tag{5.5}$$

By replacing $2t$ with $2^j t$ in Eqs. (5.4) and (5.5) a more convenient form for constructing a wavelet basis corresponding to a filter bank is yielded, this is also known as Mallat's algorithm [160].

A two-level filter bank is presented in Fig. 5.1, the analysis filters in the upper part, and synthesis filters in the lower part. For an orthogonal wavelet basis the same filters can be used in analysis and synthesis, i.e. $h_0(n) = h(-n)$, $h_1(n) = h(n)$, $g_0(n) = g(-n)$ and $g_1(n) = g(n)$. In the bi-orthogonal case the analysis and synthesis filters differ. A higher-level filter bank can be constructed by further splitting the low-pass signal into low-pass and high-pass portions by applying the same high-pass and low-pass filters. If the output of the analysis filter bank is directed to the inputs of the synthesis filter bank whose output equals to the original signal, the filter bank is said to have the perfect reconstruction property. If, in addition, the same filters can be applied in both analysis and synthesis (in reversed order) the filters are referred to as conjugate quadrature filters (CQF). Actually every orthonormal wavelet basis associated with a multi-resolution analysis corresponds to a pair of CQF filters [42]. Many different criteria for designing wavelets for different purposes have been used, e.g. the Daubechies wavelets [42] use the maximum number of vanishing moments (in addition to the orthogonality condition) to yield high smoothness.

The orthogonal wavelet transform preserves energy. However, a general shortcoming in using orthogonal compactly supported real-valued wavelet filters for compression is that they are all asymmetric except the Haar filter. This asymmetry blurs edges during quantization because asymmetric filters do not preserve phase. Symmetric filters also make it easier to deal with the boundaries of image [42, Chapters 8, 10]. On the other hand, the bi-orthogonal wavelet filters can be symmetric, compactly supported and real-valued [42, Chapter 8]. In the bi-orthogonal

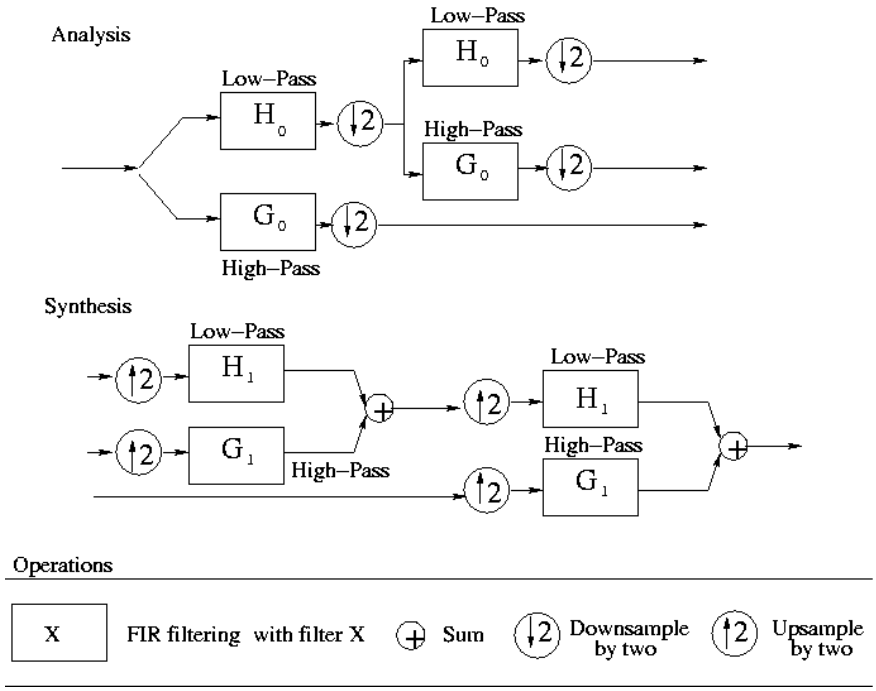

Figure 5.1: A two-level wavelet filter bank.

case the analysis filters (here h_0 and g_0) differ from the synthesis filters (here h_1 and g_1). The wavelet functions associated with the filters h_1 and g_1 are called the dual functions of the wavelet functions associated with the filters h_0 and g_0 (and vice-versa). The dual functions are orthogonal with respect to each other.

We used the 7/9 bi-orthogonal wavelet filters introduced in Antonini et al. in [2]. In addition to symmetry, the Antonini filters have also other attractive properties. They are bi-orthogonal perfect reconstruction filters with the property that both the analysis and synthesis wavelets have the regularity of four vanishing moments. Their dual functions are very similar. Hence the basis associated with the filters is almost orthogonal. The quasi-orthogonality guarantees that they almost preserve energy. The number of vanishing moments gives the filters enough regularity to create small wavelet coefficients for slowly varying domains during the analysis phase and also the reconstruction from the sparse data with quantized values is performed smoothly [160, Chapter 7]. The discrete wavelet transform is implemented by using separable wavelet filters as described e.g. by Mallat in [160]. Hence the two-dimensional convolution can be computed as one-dimensional convolutions along the columns of the image followed by one-dimensional convolutions along the rows:

$$I * \tau(i,j) = \sum_k \tau_2(i-k) \sum_l \tau_1(j-l) I_i(k,l), \tag{5.6}$$

where the pair (τ_1, τ_2) comprises of high- and low-pass filters, variables i, j indicate the pixel coordinates and $I_i(i,j)$ the value of pixel in the location (i,j). The appropriate pairings of the filters in the analysis phase are (g_0, h_0), (h_0, g_0), (g_0, g_0)

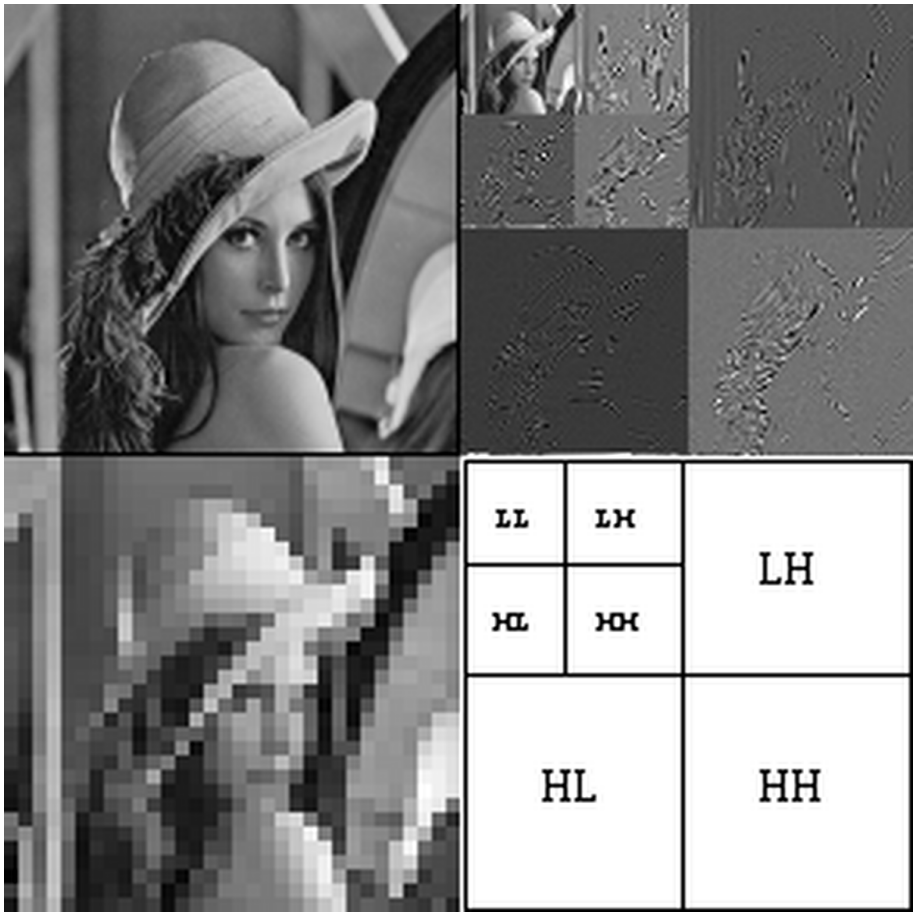

Figure 5.2: An example of a two-level wavelet transform. Upper left: The original image; upper right: the transform; lower left: the approximation image scaled up to the original scale; lower right: a diagram showing how the image is divided in the frequency space. If more levels are used in the wavelet transform, the LL band is recursively divided further into four sub-channels.

or (h_0, h_0). In the synthesis phase one uses the corresponding pairings for the filters h_1 and g_1. The pairing (g_0, h_0) refers to the fact that the high-pass filtering is first applied along the columns, followed by the low-pass filtering along the rows. In Fig. 5.2 this operation is denoted by HL. Each filtering is followed by down-sampling by decimation in the analysis phase and preceded by up-sampling in the synthesis phase. The meaning of the other pairings and their corresponding abbreviations in Fig. 5.2 are obvious. In our algorithm we used five resolution levels.

A wavelet coefficient c is said to be insignificant with respect to a given threshold T if $|c| < T$. The idea of a *zero-tree* is based on the hypothesis that if a wavelet coefficient at a coarse scale is insignificant with respect to a threshold, then all wavelet coefficients of the same orientation in the same spatial location at the

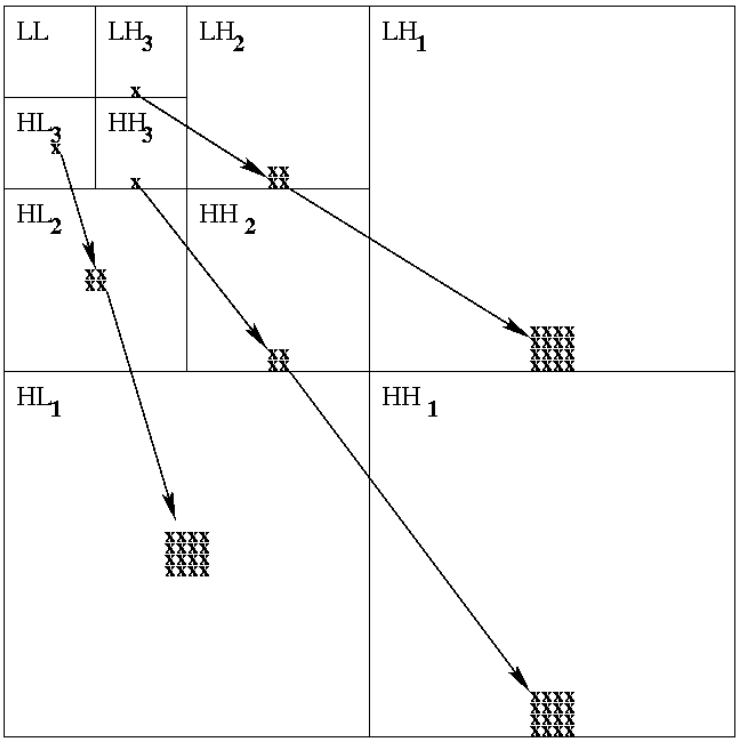

Figure 5.3: An example of the parent-child dependencies shown by the arrows in a three-level wavelet decomposition. The coefficients at the same location and resolution level, but at different frequency sub-bands, are called cousins. For example the shown locations at LH_3 and HH_3 are cousins. The zero-trees are formed as trees of parents and children within one frequency band.

finer scale are likely to be insignificant with respect to the same threshold. More specifically, in a hierarchical sub-band system, with the exception of the highest frequency sub-bands, every coefficient at a given scale can be related to a set of coefficients at the next finer scale of similar orientation. The coefficient at the coarse scale is called the parent, and all coefficients corresponding to the same spatial location at the next finer scale of similar orientation are called its children. Similarly, we can define the concepts of descendants, ancestors and cousins, see Fig. 5.3. Given a threshold T to determine whether or not a coefficient is significant, a coefficient c is said to be an element of a zero-tree for the threshold T if itself and all of its descendants are insignificant with respect to the threshold T. Therefore, given a threshold, any wavelet coefficient could be represented in one of the four data types: zero-tree root (ZTR), isolated zero (IZ) (it is insignificant but its descendant is not), positive significant (PS) and negative significant (NS) [205].

Many of the current wavelet-based image coders, such as the EZW [205] and SPIHT [190] algorithms, are progressive in nature. This means that they divide the quantized integer outputs into bit-planes, starting from the most significant

bits, and transmitting those bits first, and then transmitting the less-significant bits, until the desired accuracy has been reached or the allowed bit-budget has been used.

5.2 Arithmetic Coding

The entropy E of a sequence of symbols from an alphabet of fixed number N of symbols with known probabilities p_i, $i = 1, 2, ..., N$, is

$$E = -\sum_{i=1}^{N} p_i \log_2(p_i). \tag{5.7}$$

Assuming inter-symbol independence in the sequence, the optimal number of bits for encoding such a sequence of symbols would then be

$$N_B = N_S E = -\log_2(p), \tag{5.8}$$

where N_S is the total number of symbols in the sequence, and p is the probability of the sequence, which is the product of the individual symbol probabilities in the sequence.

The arithmetic coding algorithm [133, 186] is an entropy coding method, producing a nearly optimal coding length, i.e. $-\log_2(p)$ bits, for a sequence of symbols with a known probability p. The arithmetic coding algorithm basically works as follows (a more detailed description is given e.g. in [246] or [93]):

1. Begin with a current interval $[L, H)$ initialized to $[0, 1)$.
2. For each symbol of the sequence, we perform two steps:

   Subdivide the current interval into subintervals, one for each available symbol. The size of a symbol's subinterval is proportional to the estimated probability that the symbol will be the next symbol in the sequence, according to the model of the input. This means that if we only have a few zero-tree symbols to be coded, the distributions of the symbols can be computed and included without increasing the encoded sequence length significantly.

   Select the subinterval corresponding to the symbol that actually occurs next in the sequence, and make it the new current interval. After the interval corresponding to the whole sequence has been computed, it uniquely corresponds to the sequence.
3. Use enough output bits to distinguish the final current interval from all other possible final intervals (for details, see the example below).

The length of the final subinterval is equal to the product of the probabilities of the individual symbols, which is the probability p of the particular sequence of symbols in the sequence. The final step uses almost exactly $-\log_2(p)$ bits to distinguish the sequence from all other possible sequences. We need some mechanism to

Table 5.1: A simple arithmetic coding example (from [93]).

Current Interval	Action	Subintervals			Input
		a	b	EOF	
[0.000, 1.000)	Subdivide	[0.000, 0.400)	[0.400, 0.900)	[0.900, 1.000)	b
[0.400, 0.900)	Subdivide	[0.400, 0.600)	[0.600, 0.850)	[0.850, 0.900)	b
[0.600, 0.850)	Subdivide	[0.600, 0.700)	[0.700, 0.825)	[0.825, 0.850)	b
[0.700, 0.825)	Subdivide	[0.700, 0.750)	[0.750, 0.812)	[0.812, 0.825)	EOS
[0.812, 0.825)					

indicate the end of the sequence, either a special end of sequence (EOS) symbol, indicating the end of the sequence, coded just once, or some external indication of the sequence length. The probability of the EOS symbol is selected to be a low value.

Step 1 of the algorithm is just a straightforward initialization of the current interval. In step 2, we need to compute only the subinterval corresponding to the symbol a_i that actually occurs. To do this we need two cumulative probabilities, $P_C = \sum_{k=1}^{i-1} p_k$ and $P_N = \sum_{k=1}^{i} p_k$, The new subinterval is $[L + P_C(H - L), L + P_N(H - L))$.

In Table 5.1 an example encoding of an input containing the symbols bbb adopted from [93] is shown. Using arbitrary fixed probability estimates $p(a) = 0.4$, $p(b) = 0.5$, and $p(EOS) = 0.1$.

The step 2 of the algorithm repeated for each of the symbols in the example sequence are shown in the rows of the Table 5.1. Each row of the table shows the current interval and the subintervals corresponding to each possible symbol (a, b, EOS). The interval corresponding to the symbol appearing in the sequence determines the interval which is further subdivided in the next iterations. In the example the final interval (without rounding) is [0.8125, 0.825), which in binary is approximately [0.11010 00000, 0.11010 01100). We can now uniquely identify this interval by the binary value 1101000 (a value inside the interval). According to the fixed model, the probability p of this particular sequence is $(0.5)^3(0.1) = 0.0125$ (exactly the size of the final interval) and the code length should be $-\log_2(p) = 6.322$ bits. In practice we have to use 7 whole bits.

5.3 Compression Algorithm

The block diagram of the SAR image compression algorithm is presented in Fig. 5.4. The first phase of the algorithm performs a wavelet transform on the image data to yield the wavelet coefficients. To prune the wavelet coefficients, we then use a technique described in Section 5.3.1. The coefficients that are left (i.e. have nonzero values) after the pruning process are called significant coefficients, while the pruned ones are called insignificant coefficients. The zero-tree structure for coding the locations and signs of the significant coefficients is used. The absolute

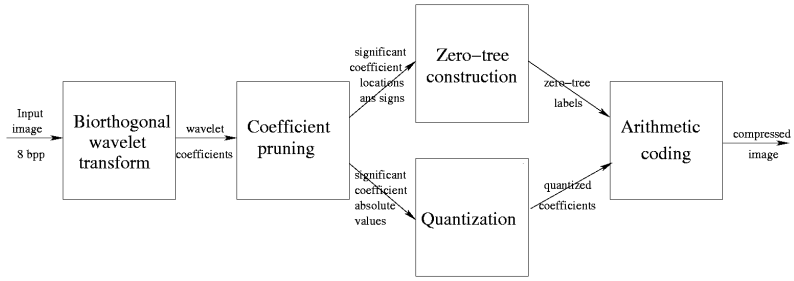

Figure 5.4: Block diagram of the image compression algorithm.

values of the significant wavelet coefficients are quantized as described in Section 5.3.2. Finally, the zero-tree symbols and quantized wavelet coefficients' absolute values are coded using arithmetic coding [133, 186, 246].

We have adopted the zero-tree structure and coding the zero-tree labels from the EZW algorithm [205]. Our algorithm uses the human visual system (HVS) dependent quantization which is different from the successive approximation quantization used in the EZW algorithm. We do not order the wavelet coefficients according to their importance as in EZW, but take their importance to visual perception into account in our quantization scheme. Thus our algorithm also does not use embedding like EZW. Embedding means that a single coded file can used to decode the image at almost any rate less than or equal to the coded rate, to give the best reconstruction possible with the particular coding scheme. This makes progressive coding, i.e. gradually refining the image resolution during the decoding, possible.

In the current operative application the image is compressed with a suitable set of parameters and then transmitted to end-users either via satellite connection or mobile connection, depending on the receiver equipment on board of the receiving vessel. After receiving the image, it is decompressed in the background and only after that the user is notified about the arrival of a new image. Progressive coding could be a useful addition to the algorithm in the future, depending on the development of the operative system.

In our algorithm there are multiple user-defined parameters, which need to be set for a specific set of data (e.g. for a certain SAR instrument) and user requirements. This usually necessitates some expert supervision in the set up phase to adjust the parameters suitably, but it also allows great flexibility for many different kinds of data sets and user requirements. The parameters have now been adjusted for Radarsat ScanSAR data. A future improvement would be to give more exact guidelines for selecting the parameters for different kinds of data.

5.3.1 Wavelet Coefficient Pruning

In our algorithm we are using a 5-level wavelet transform, the levels are numbered such that level 5 corresponds to the coarsest resolution and level 1 to the finest resolution. For the approximation image at level 5, we save all the coefficients. For the wavelet coefficients at resolution levels 3–4, thresholding is used that is

dependent on the detail (high-pass) image statistics, i.e., we prune coefficients whose absolute values are less than a threshold $T_D(x, y)$ defined as

$$T_D(x, y) = T_D(G, l) = f_G(x, y) f_l \sigma_D. \tag{5.9}$$

The index D refers to the detail image with standard deviation σ_D. The resolution-level-dependent factor f_l is given as a parameter to the algorithm. The term $f_G(x, y)$ takes into account the local statistics in the image by applying different thresholding in different areas of the image. We were led to implement this option because of the change in local image statistics in the SAR data caused by the change of the incidence angle [154]. The amount of the local thresholding can be adjusted by a gain parameter G as described by the equation

$$f_G(x, y) = 1.0 + G(\sigma_{\text{rel}}(x, y) - 1.0). \tag{5.10}$$

A single threshold for all the pixel positions is achieved by setting G to zero, which is also the default value. Values above zero cause the local variation to be taken into account proportionally to G. The values of the factor f_G are computed in the centers of local windows and smoothed between adjacent windows. The relative standard deviation $\sigma_{\text{rel}}(x, y)$ at image location (x, y) is computed as

$$\sigma_{\text{rel}}(x, y) = \frac{\sigma(x, y)}{\sigma}, \tag{5.11}$$

where $\sigma(x, y)$ is the local standard deviation, and σ is the global standard deviation for the image. The local standard deviation is computed in a $n \times n$ pixel window, where the value of n is a user-adjustable parameter.

At the two finest scales ($l = 1$ and $l = 2$), we use a thresholding scheme which takes into consideration whether the wavelet coefficient was determined as being significant at a previous scale i.e. inter-scale dependency. We first compute a threshold value T_B using the statistics for the second-finest resolution level

$$T_B = \frac{\sigma_{\text{LH}} + \sigma_{\text{HL}} + \sigma_{\text{HH}}}{3}. \tag{5.12}$$

We then divide the wavelet coefficients at level 2 into two categories, i.e., the *textured area coefficients*, and the *textureless area coefficients*. A coefficient is called a textured area ("cheap") coefficient if the wavelet coefficient at the next lower resolution level at the same location is significant, otherwise it is a textureless area ("expensive") coefficient. The thresholds applied to the two types of coefficients differ from each other.

The coefficient pruning process for the textured area coefficients is as follows. First, we compute a threshold

$$T_1(x, y) = f_G(x, y) f_1 T, \tag{5.13}$$

where $f_G(x, y)$ is as in Eq. 5.10 and f_1 is a user-adjustable parameter. The condition for pruning is

$$\hat{c} = \begin{cases} c, & \text{if } |c| > T_1 \\ 0, & \text{otherwise,} \end{cases} \tag{5.14}$$

where $\hat{c}$ is the new wavelet coefficient value, i.e., the coefficient is pruned if the absolute value is less than or equal to the threshold T_1. After applying the threshold T_1 most of the significant coefficients at resolution level 2 are determined. Let us denote the set of coefficients that satisfy the condition in Eq. (5.14) by A. In addition to set A, some other coefficients, denoted here by set B, will also be included in the set of significant coefficients. A coefficient will be included in set B if the coefficient together with coefficients in A is believed to form an edge in the image. The stepwise procedure, described below, to determine if this is the case can be regarded as a geometric filter.

The test whether a coefficient is in the set B proceeds as follows: we first apply threshold T_2 to exclude very small coefficients from set B. Threshold T_2 is computed as

$$T_2(x, y) = f_G(x, y) f_2 T_B, \tag{5.15}$$

where f_2 is a user-adjustable parameter so that $f_2 < f_1$. Let us suppose that the magnitude of a coefficient exceeds this threshold. Then a 5×5 pixel neighborhood in the wavelet domain is studied for coefficients for which the absolute strength C_w, defined as the sum of the coefficients' absolute values in the three detail images at the same resolution level (the sum of "cousins", see Fig. 5.3),

$$C_w = |c_{\mathrm{LH}}| + |c_{\mathrm{HL}}| + |c_{\mathrm{HH}}|, \tag{5.16}$$

exceeds a third threshold value

$$T_3(x, y) = f_G(x, y) f_3 T_B, \tag{5.17}$$

where f_3 is a parameter. First we study whether in the 3×3 neighborhood there is more than one coefficient who has the same sign as the coefficient studied, whose absolute strength C_w exceeds $T_3(x, y)$. If that condition is fulfilled and, additionally, if in the 5×5 neighborhood there is more than one coefficient for which the same condition holds, then the coefficient c is included in set B. The sign condition is necessary because, in the case of symmetric FIR filters, an edge pixel generates two large wavelet coefficients with different signs.

A similar pruning process is performed for the textureless area coefficients, but using higher values of pruning factors f_4, f_5 and f_6 instead of f_1, f_2 and f_3 (i.e. $f_1 < f_4$, $f_2 < f_5$ and $f_3 < f_6$). All these values are user-adjustable parameters. At the finest resolution level a similar pruning process with textured and textureless areas is performed.

5.3.2 Quantization

The sensitivity of the human visual system (HVS) to changes in the intensity level is dependent on three different factors: the local background intensity level, the local spatial frequency and the local texture content [74, 101, 119, 189]. The first term, sensitivity to the background intensity level, is also known as the Weber-Fechner law :

$$dR_I = \alpha \frac{dI}{I}, \tag{5.18}$$

where dR_I is the change of the HVS response to the intensity stimulus change dI with background intensity I, and α is an experimentally defined constant. After integration, the Weber-Fechner law has the form $R_I = \alpha \log(I/I_0)$. I_0 is the stimulus below which nothing is perceived, and R_I is thus zero for I below I_0.

There have also been several studies on the spatial frequency sensitivity of the HVS [65, 72, 101]. The spatial frequency perceived depends on the pixel size of the image viewed and the viewing distance. Some numerical values can be computed, for example, for a typical viewing distance and a typical monitor or printer resolution. The spatial frequency is typically expressed in cycles per degree. Some formulas for computing the contrast and frequency sensitivity of the HVS are given e.g. in [166].

The quantization model we have used is similar to that presented in [142]. We use a basic quantization step for each wavelet coefficient computed as

$$S_D = q_0 f_I(x,y) f_F f_T, \tag{5.19}$$

where q_0 is a user-adjustable factor, f_F is a spatial frequency factor and f_T is a texture content factor. The background intensity factor $f_I(x,y)$ is computed from the approximation image as

$$f_I(x,y) = 3.0 + \frac{a_q(x,y)}{64}, \tag{5.20}$$

where $a_q(x,y)$ is the quantized approximation image value at image location (x,y), and 64 is the number of quantization steps. For the frequency sensitivity factor f_F we have used the values in Table 5.2, which we have experimentally selected.

Table 5.2: The HVS frequency sensitivity values f used in our algorithm for the different wavelet decomposition bands. Level 1 is the highest resolution level and level 5 the lowest resolution level.

Resolution/Band	LH	HL	HH
1	1.00	1.00	$\sqrt{2}$
2	0.32	0.32	$0.32\sqrt{2}$
3	0.16	0.16	$0.16\sqrt{2}$
4	0.10	0.10	$0.10\sqrt{2}$
5	0.08	0.08	$0.08\sqrt{2}$

The texture factor f_T is a very simple approximation based on the number of significant coefficients at the location and computed as

$$f_T = 1.0 + 0.5\frac{N_{\text{sc}}}{3N_{\text{levels}}}, \tag{5.21}$$

where N_{sc} is the overall number of significant wavelet coefficients at the location and N_{levels} is the number of resolution levels, which is equal to five in our algorithm.

The number of quantization steps N_q is computed from the original step value S as

$$N_q = \begin{cases} \text{round}(l/S), & \text{if } N_{\min} < N_q < N_{\max} \\ N_{\min}, & \text{if } N_q \leq N_{\min} \\ N_{\max}, & \text{if } N_q \geq N_{\max}, \end{cases} \tag{5.22}$$

where $N_{\min}$ and $N_{\max}$ are user-defined parameters that can be used to adjust the number of quantization steps. l is the length of the interval of the wavelet coefficients' absolute values in the detail image in question,

$$l = \max_i |c_i| - \min_i |c_i|. \tag{5.23}$$

The first quantization level is that closest to the minimum, and is now defined as

$$S_0 = \frac{f_q l}{N_q} \tag{5.24}$$

and the quantization step is increased by a value Δ_q at each step toward the band maximum, producing a linearly-increasing quantization step. f_q is a user-adjustable parameter; $f_q = 1$ produces a uniform quantization, while values $f_q < 1$ produce an increasing quantization. The value of Δ_q can be found to be

$$\Delta_q = \frac{2(l - N_q S_0)}{{N_q}^2 - N_q}. \tag{5.25}$$

We found experimentally that the value $f_q = 0.1$ gives quite a good visual quality performance. We also found that this value gave a much smaller quantization error in the L^2 norm than uniform quantization.

The approximation image, i.e., the values of the wavelet coefficients in the LL-band of the lowest resolution level are quantized using similar kind of nonuniform quantization with a fixed number of 64 quantization steps corresponding to six bits.

5.3.3 Coding

The quantized approximation image coefficients are coded using a fixed number of six bits. The wavelet coefficients of the detail images are coded for each detail image separately using arithmetic coding [93, 133, 186, 246]. This also requires a description of the distribution of each detail image's coefficients to be written into the compression output file, but with only a few quantization steps the distribution descriptions do not occupy very much file space. The zero-tree labels, see Section

5.1, are also coded using arithmetic coding. The finest resolution level labels are coded separately from the others because there are only three labels possible, as no isolated zeros can be at the finest resolution level. The other resolution levels can contain all four possible labels.

5.3.4 Open Sea Masking

We have also used an open sea detection algorithm to reduce the compressed file sizes. If we can detect the open sea areas correctly, we can then mask off these areas before compressing the images and get significant reduction in the compressed file size for images with large open water areas. The open sea detection algorithm is similar to that presented in [108], and is based on spatial signal autocorrelation. The open sea detection is not yet totally reliable under all circumstances, especially in wet snow conditions, i.e. there is wet snow or even water on the sea ice. However, the results of the open sea identification are mostly satisfactory as the experiences gathered during the winters of 1999/2000 and 2000/2001 show. Together 147 Radarsat images were classified, the majority of them correctly. In 20 images some ice area was interpreted as open sea, which is a serious error in this context. The classification errors occurred mainly in late springtime. Anyhow, visual verification of the classification result is required before compression. An example of open sea masking is shown in Fig. 5.5. The compression ratio for the image is clearly lower without than with open water masking. The compression ratios naturally depend on the image and the sizes and shapes of the masked (land and open sea) areas. The parameters used in this test were similar to those producing a compression ratio of about 20 : 1 for the test images. The compression ratio for the image without the open water mask is higher than the usual 20 : 1 because also a land mask has been applied to the original image. The masked land area appears white in Fig. 5.5.

5.3.5 Computational and Technical Aspects

The compression program requires a relatively large amount of random access memory (RAM); for typical SAR images of some 8 megabytes (MB), a minimum of 64 MB is required, and 128 MB is recommended. On a 3 GHz PC, currently in operational use, with 1024 MB of RAM and running Linux, the compression and decompression of a typical SAR image takes just a few seconds.

The algorithm parameters can be adjusted to be suitable for visual images, or also for some other type of images, e.g. images produced by a specific sensor. There also exists an RGB color version of the algorithm tested for some visual RGB images. The algorithm first makes a conversion into the YIQ color coordinate system and then uses a coarser compression for the chromatic information (I and Q) than for the luminance information (Y). In the decompression the inverse conversion from YIQ to RGB is performed.

The algorithm has been implemented using the standard C language without any platform-specific code and should work on any platform. Also the microprocessor-dependent byte order of multi-byte data types is tested and taken into account in

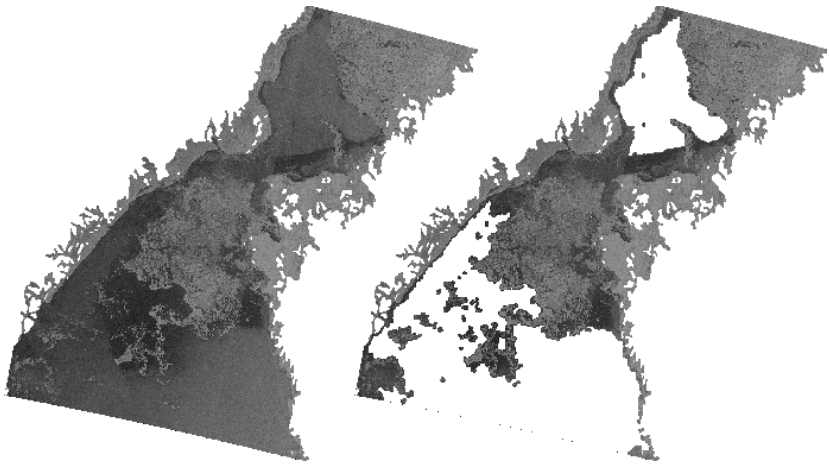

Figure 5.5: A SAR image, April 5th 1999, Gulf of Bothnia, ©Canadian Space Agency (CSA), before (left) and after open sea detection (right). The masked pixels appear white in the image. The compression ratios for the original image was 43.4 : 1 and 54.1 : 1 for the masked image using the default compression parameters.

run-time.

5.4 Some Performance Comparisons

The algorithm performance has been compared to the JPEG algorithm [177], which was the most popular standard image compression method available at the time of the developing of our algorithm. Also comparisons to the SAR image compression algorithm, i.e. the ALP algorithm [151], in use at FIS were made. Both objective image quality measures and subjective evaluation by sea ice SAR experts were made. Also different compression ratios (CRs) using our algorithm were tested to find out useful compression ratios for visual operational use of our SAR data.

5.4.1 Experiments for Parameter Selection

We varied the parameters starting with values selected during our preliminary studies. The compression ratio for typical SAR images using this set of parameters is about 20 : 1. When changing the wavelet coefficient threshold parameters, both the error measures and compression ratio change smoothly. The results for quantization parameters are similar. For details, see [publication 2]. The final adjustment of the parameters can be done using visual inspection of the images.

For objective comparison between an image pair (original and compressed) we use two measures, Peak Signal to Noise Ratio (PSNR) and coefficient of determination, R^2 [242]. The PSNR is defined (for an eight-bit image with a maximum value

$I_{\max}$=255) as

$$\mathrm{PSNR} = 10 \log_{10} \frac{{I_{\max}}^2}{\frac{1}{N} \sum_i \sum_j (I_o(i,j) - I_c(i,j))^2} \tag{5.26}$$

and R^2 is defined as

$$R^2 = \frac{\sum_i \sum_j (I_o(i,j) - \mu)^2 - \sum_i \sum_j (I_o(i,j) - I_c(i,j))^2}{\sum_i \sum_j (I_o(i,j) - \mu)^2}, \tag{5.27}$$

where I_o refers to the original (uncompressed) image, I_c to the compressed image, and μ is the computed mean value of the original image. The sums are computed over whole images, consisting of N pixels.

We used both SAR and optical images in our study. The R^2 values are higher for the optical images, around 0.95, compared to the corresponding values for the SAR data, around 0.60. Because of the nature of the SAR data [publication 2] it is obvious that the reduction of oscillation at the two finest scales has a greater effect on the SAR data than on the Lena image, which was used as one optical comparison image in our experiments.

The number of quantization bins is less significant in SAR image compression than in compression of optical images. When the maximum number of quantization steps was set to three, the PSNR and R^2 values of optical images decreased considerably (PSNR almost 4 dB) compared to the corresponding values for SAR data (PSNR about 0.4 dB). Also our visual observations have shown that using a small number of quantization steps has only a slight effect on the visual image quality of SAR images.

To get higher compression ratios using the proposed algorithm both quantization and wavelet coefficient thresholding can be tightened for SAR images; for optical images increasing the wavelet coefficient threshold values yields better results. The compression ratios with the same set of parameters are generally higher for optical images than for SAR images. It should be noted that the set of parameters has been adjusted for visual compression of SAR images, and it is not optimal for optical images in the sense of the error measures and the compression ratio.

5.4.2 Objective and Subjective Comparisons to ALP and JPEG Algorithms

We computed many objective image quality measures and in Table 5.3 give some PSNR and R^2 values computed from our set of SAR test images. According to our experience the studied objective measures do not directly indicate the visual quality of compressed SAR images very well. For example, there can be a significant visual quality difference between two compressed SAR images with the same PSNR. In the case of SAR images lower PSNR values than for optical images are typically acceptable if the edges are preserved and the speckle is attenuated in the compression. A subjective image quality test was implemented by creating a WWW-page and the feedback was collected using an on-line feedback form and a CGI script. The web pages contained eight 512×512 image windows, one for each of the eight test images, each compressed using six different compression schemes,

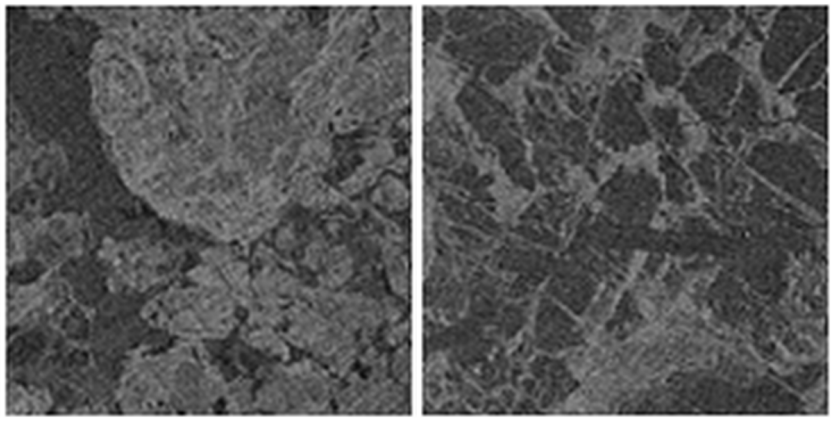

Figure 5.6: Two 512×512-sized windows from SAR images, referred to as SAR1 (left), and SAR2 (right), used as examples of the compression, ©Canadian Space Agency (CSA).

Table 5.3: Some objective quality measures for SAR images compressed with different methods. The values given are medians of the values computed for eight SAR test images.

Method (CR) / Measure	PSNR	R^2
250 m (6.25 : 1)	27.67	0.610
ALP (20 : 1)	27.18	0.564
JPEG (20 : 1)	27.55	0.599
Wavelet (20 : 1)	27.82	0.624
Wavelet (40 : 1)	26.85	0.529

i.e., (1) image down-sampled to 250 meter resolution (typical highest resolution in which the images are delivered to ships, compression ratio is about 6 : 1), (2) ALP compression with a compression ratio of about 20 : 1, (3) JPEG with a similar compression ratio, (4) our wavelet compression with a similar compression ratio, (5) our wavelet compression with a higher compression ratio of about 40 : 1, and (6) JPEG with about similar higher compression ratio. Compression results for the images SAR1 and SAR2, shown in Fig. 5.6 using these methods have been presented in Figs. 5.7 and 5.8. The compression results with the higher compression rate are shown in Fig. 5.9. Some Gaussian noise has been added to the wavelet-compressed image of Fig. 5.9, because it seemed to help the visual interpretation of the images with high compression ratios in our visual tests.

Subjective assessments were given through the WWW-pages by awarding grades from zero (useless) to five (contains practically all the necessary information for navigation) to the images. Totally eight persons gave their assessments, all of them had long experience with using sea ice SAR data (including ice service personnel and ice breaker captains). We have divided the assessments into two categories, one being the overall category containing all the assessments, and the other contain-

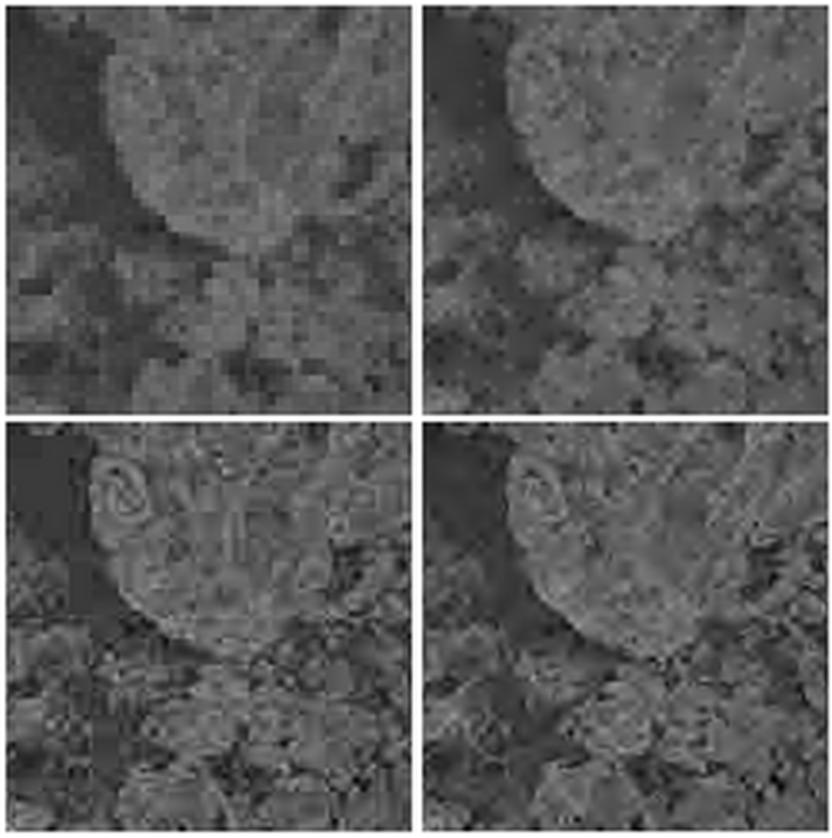

Figure 5.7: The original SAR1 at 250 m resolution (upper-left) and compressed with a compression ratio of about 20 : 1 using three algorithms: ALP compression (upper-right), JPEG compression (lower-left), and wavelet compression (lower-right).

ing assessments from the sea ice specialists at FIS. The FIS category is presented separately because the staff at FIS are specialists in interpreting sea-ice SAR images, and this feedback can therefore be considered to be the most valuable for our purposes. The images were presented in the web pages in random order so that the person giving the numbers could not know from the order of the images which method was used for the compression. The feedback evaluation is presented in Table 5.4. The values in the table are the grading means for the eight test images, and the values in parenthesis are the standard deviations of these appraisals.

It can be seen from the Table 5.4 that the wavelet compression receives the best marks. It should also be noted that the quality of the monitor used for inspecting the images on the WWW-pages can affect the grading. For a reasonable feedback, a monitor capable of showing all the 256 gray levels and with enough resolution to show 512×512 pixel images is required. A problem with the JPEG compression is that the method produces some undesired artifacts at high compression ratios, e.g. JPEG 8×8 pixel block boundaries can produce visible artificial edges in the

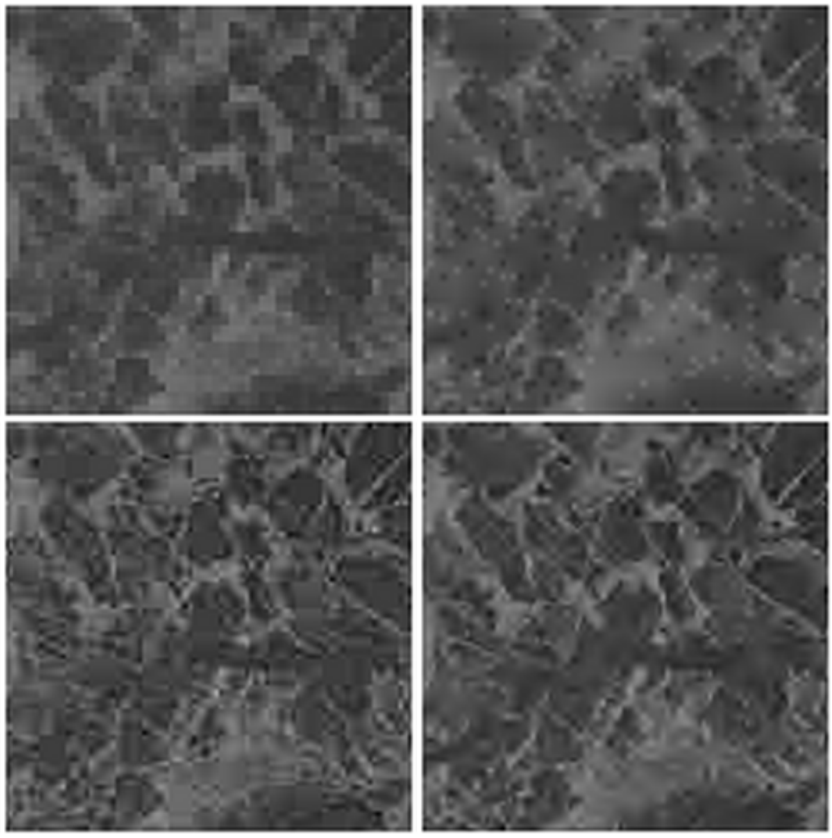

Figure 5.8: The original SAR2 at 250 m resolution (upper-left) and compressed with a compression ratio of about 20 : 1 using three algorithms: ALP compression (upper-right), JPEG compression (lower-left), and wavelet compression (lower-right).

images that can lead to misinterpretations. This blockiness is especially disturbing for high compression ratios, and clearly visible in the JPEG compression example of Fig. 5.9.

Typical end-user comments were that all the essential features can be seen in the wavelet compressed images, but there exist some unsharpness in certain areas. Such unsharpness they called "frog spawn". These are homogeneous areas actually containing very little sea ice information important for navigation. This kind of feedback can partly be explained by the fact that the end-users are used to view speckled SAR-data.

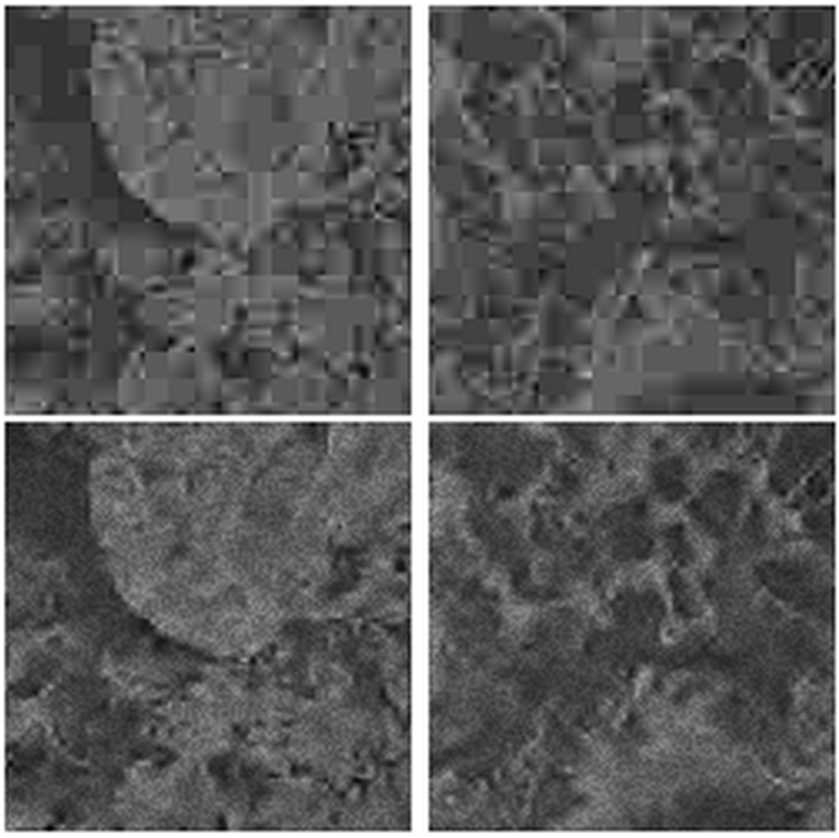

Figure 5.9: The panel displays the original images SAR1 and SAR2 compressed with a compression ratio of about 40 : 1 using JPEG (upper images) and the wavelet algorithm (lower images). The blocking effect is very clearly visible in the JPEG compression. The wavelet compressed images are post-processed as described in the text.

5.5 Some Properties of the Algorithm and Discussion

A wavelet-based compression algorithm for SAR images with many target-dependent features was developed for operational use at the Finnish Ice Service. Sea ice is a very specific target with a lot of strong transitions due to fragmentation of the ice cover on multiple scales. The statistics of SAR images differ significantly from that of optical images, and the special features of the image data to be compressed must be taken into account in the compression. For SAR images compression ratios about 20 : 1 give reasonable results for practical use. In practice, higher compression ratios are achieved for typical images because the land areas are masked off (i.e. coded with a single value) before compression. Also, higher compression ratios are possible depending on the use of the images.

The compression results with the implemented method are visually better than

Table 5.4: Subjective quality evaluation of SAR test images. FIS represents the grades given by the sea ice specialists of the Finnish Ice Service. The values in parentheses after the method names are the approximate compression ratios, and the values in parentheses after the assessment grades are their standard deviations.

Category	All	FIS
Persons	8	3
Images	42	24
250m	1.62 (0.91)	1.29 (0.75)
ALP (CR 20:1)	1.45 (0.86)	1.17 (0.70)
JPEG (CR 20:1)	3.21 (1.18)	3.00 (1.02)
Wavelet (CR 20:1)	3.38 (1.32)	3.50 (1.25)
Wavelet (CR 40:1)	1.79 (1.12)	1.63 (0.88)

ALP or JPEG compressed images with similar compression ratios, though the objective quality measures do not differ very much. A more thorough statistical analysis of user assessments would require a much larger evaluation test and it is practically impossible to implement with our resources. The main point of the user assessments received is that our wavelet compressed images are useful in operational use contain most of the navigationally essential sea ice information and outperform the other tested more standard methods.

Sea ice SAR data transmission to ice breakers and ships has also been implemented by the Canadian Ice Service (CIS). At CIS a commercial wavelet-based compression technique (MrSid by LizardTech, inc. [15]) is used for automatically compressing the Radarsat data with a compression ratio of $15:1$. This software utilizes image tiling, i.e. splitting the image into subsets, or tiles, and applying the wavelet transform to these tiles separately. This technique makes it possible to process very large images because only a part of the image is necessary to be stored in the central memory at a time. The transmission to ice breakers has been accomplished by either satellite (Inmarsat, Msat) or by cellular connection [193]. The possible advantage of our system is that we can integrate the compression more tightly to our sea ice SAR transmission and viewing system and also adjust and further develop the compression. Basically, the transmission systems are quite similar, heavily compressing the data using a wavelet-based scheme, and then transmitting the compressed data via satellite or cellular connection to the ice breakers.

After the implementation of our algorithm the JPEG 2000 still image compression standard [217] has been completed. JPEG 2000 also uses wavelet transform and similar bi-orthogonal filters as in our algorithm. In JPEG 2000 it is possible to select regions of interest which are compressed more accurately than other areas and it is possible to tile the image into rectangular non-overlapping blocks and compress these separately reducing the memory requirements. Image tiling could be useful for large SAR images and considered as an improvement to our algorithm. In our current algorithm the local image statistics can be taken into account by adjusting the user-defined parameters which produce local wavelet

coefficient thresholding. JPEG 2000 also uses visual frequency weighting to take advantage of the human visual perception. In our algorithm we also take into account the background intensity and texture in the HVS dependent quantization. JPEG 2000 supports scalability meaning that it is possible to reconstruct images of more than one quality or resolution simultaneously. Our algorithm does not currently support this kind of progressive coding scheme, but it could possibly be a future improvement if it will be needed in our operational system. In our algorithm the coefficients are handled differently in homogeneous and textured areas and the quantization scheme also differs from that of JPEG 2000. For entropy coding both algorithms use the arithmetic coding.

Through the manipulation of the wavelet coefficients one can control the local regularity of the reconstructed image. Hence, the wavelet-based compression also performs speckle-reduction filtering. One can optimize the performance of the algorithm with respect to this property with properly selected parameters (either without quantization or with very accurate quantization). The wavelet coefficient thresholding presented can also be seen as a despeckling filter. It could be possible to improve this by applying e.g. Wiener filtering in the wavelet domain [70]. Also some kind of image preclassification could be performed to define local wavelet thresholds. These improvements will be considered in the future.

The parameters of the system are easily adjustable. The optimal parameters for a certain class of images, such as SAR images produced by a specific instrument, or optical images of some typical scenery, must be defined experimentally by an expert aware of the importance of the features that should be preserved in the compression. This may be a time-consuming process because of the large number of parameters, but needs to be done only once for a specific set of data and user requirements.

The compression can be further improved by using an open water mask before applying the algorithm. The land and open sea masks can optionally be produced to be smoothly changing at the mask/ice edges to improve the wavelet compression because the smoothed edges do not produce such large wavelet coefficients as sharp edges do. A much larger land mask covering the whole arctic area has also been implemented at FIMR. This land mask is coarser than the mask for the Baltic Sea area, and a small band of the land in the coasts has been left outside the mask to make smoothing in the boundaries possible. This masking and smoothing of the mask boundaries has shown to further improve the compression ratio by even about $10 - 20\%$ compared to the unsmoothed mask boundary. With high compression ratios also some post-processing can improve the visual appearance of the images.

It is not at all obvious that the wavelet transform is the best possible choice for compressing the data in question, although it did give better results than e.g. the cosine transform (JPEG). Especially the new representations (ridgelets and curvelets) developed by David Donoho and his colleagues, see e.g. [20], would be interesting research topics. In these representations it is possible to describe an edge with a few coefficients. In this way we could partly overcome the problem that most of the variation is concentrated at high spatial frequencies in SAR imagery.

Chapter 6

Baltic Sea Ice SAR Image Segmentation and Classification Using Pulse-Coupled Neural Networks

Because of speckle noise present in all SAR data, it is necessary to take the contextual information, i.e. information present in the neighborhood of a single SAR image pixel, into account in SAR image segmentation. Pulse-Coupled Neural Networks (PCNN) [57, 188] are a convenient way to implement contextual image segmentation. PCNNs are based on modeling operations found on mammals' visual cortex. The simplified PCNN algorithm used in this work is relatively easy to implement and it performs adequately for our Radarsat-1 SAR data. When compared to some other tested segmentation methods it gives very good segmentation results for our sea ice SAR data. Also the execution times are reasonable for our operational data delivery in near-real-time (NRT) to the end-users.

Because our operational SAR data is not absolutely calibrated, we can not directly use the relationship between SAR backscattering and different sea ice classes. Instead we define the classes from the data by decomposing the estimated SAR sample distribution into Gaussian distributions. The assumed underlying sea ice classes derived from the estimated total distribution are then described by the Gaussian distributions of the decomposition. According to our studies the distributions estimated from data (e.g. histograms scaled to sum up to one) in uniform areas of our SAR data are very close to Gaussians distributions, and this assumption is justified. By making this assumption we can first decompose a training set into sea ice classes solely based on a training data set and then use this information to segment the image with PCNNs.

6.1 Decomposing Sample Distribution into Class Distributions

To define classes from data, we compute an estimate of the SAR pixel value distribution for the training data set. First, the sample histogram is calculated using all the incidence angle corrected images of the training data set. We make an assumption that the estimated total distribution is a mixture of underlying sea ice distributions, which are additionally assumed to have Gaussian form. To decompose the sample distribution into these class distributions, we first note, that it is practically impossible to find the class distributions from the SAR pixel value distribution computed from the incidence angle corrected training set of 8 bpp SAR data processed by the KSAT SAR processor. This is because the assumed underlying distributions are overlapping very much. However, we can make use of the assumption that in uniform sea ice areas the pixel value data have Gaussian distributions.

We locate fixed size, say $N \times N$ pixels, sample windows in the image, where the sample distribution is close to a Gaussian distribution, and compute the distribution of the means of the pixel values in these windows. Assuming that the total distribution is composed of distributions of sea ice classes, we may now denote the mean of a sea ice class k by μ_k and the variance by σ_k^2. As a consequence of the central limit theorem, the assumed underlying Gaussian class distributions in the pixel value distribution become Gaussian distributions with the same mean μ_k and variance σ_k^2/N in the distribution computed for the window means. To measure the Gaussianity of the sample windows we fit a Gaussian to the sample window distribution and compute the coefficient of determination, denoted by R^2, and use only those sample windows for which R^2 exceeds a given threshold T.

In practice the estimated window mean distribution with suitable window size really shows some peaks, unlike the total pixel value distribution. However, it is still impossible to determine the variances of the assumed classes corresponding to these peaks from this distribution. This is because there are probably some minor classes with low prior probabilities, the incidence angle correction is not perfect for all types of sea ice, and at the used resolution (100 m) also many pixels are mixtures of several sea ice classes. However, the modes of the most probable classes can be determined from this distribution. And from assuming the distributions to be Gaussians follows that the class-wise means are the same as the modes. A simple peak detection algorithm is applied to the sample window mean distribution, after it has been slightly smoothed by applying a Gaussian kernel to reduce the high frequency ripple, which could cause some undesired peaks, in the estimated distributions. We used a Gaussian kernel with standard deviation $\sigma = 1.0$. The peak detection is based on the sign changes of the local difference, i.e. the sign of the difference changes from positive to negative at peaks. Additionally the algorithm only accepts the highest peak within a given neighborhood to filter possible peaks very close to each other. The number of classes is defined by the number of peaks. The peaks (modes) located are then assumed to be the means of the class distributions.

Then the algorithm uses the pixel value distribution to estimate the class distri-

butions. This is accomplished by using a modified version of the EM algorithm [44]. The EM algorithm basically consists of two iterative steps, the expectation (E-step) and maximization (M-step) steps. The E-step finds the expectation of the log-likelihood, given the observed (incomplete) data $\mathbf{x} = (x_1, ..., x_N)$ and the current parameter estimates, and then the M-step maximizes this expectation with respect to the parameters. The x_is are assumed to be independent and identically distributed (i.i.d), i.e. their covariance matrix is diagonal. We use a mixture model of M Gaussians over all the data values y (i.e. SAR pixel values):

$$p(y, \Theta) = \sum_{m=1}^{M} \alpha_m p_m(y|\theta_m), \tag{6.1}$$

where the parameters are $\Theta = (\alpha_1, ..., \alpha_M, \theta_1, ..., \theta_M)$ such that $\sum_{m=1}^{M} \alpha_m = 1$ (prior probabilities of the M Gaussians) and each $p_m(y)$ is a Gaussian density function with parameters $\theta_m = (\mu_m, \sigma_m)$ i.e. mean and standard deviation. Based on the Bayes's rule, we can compute

$$p(m|x_i, \Theta') = \frac{\alpha_m p_m(x_i|\theta'_m)}{\sum_{j=1}^{M} \alpha_j p_j(x_i|\theta'_j)}. \tag{6.2}$$

m is the index of the Gaussian $m = 1, ..., M$, and Θ' and θ'_j refer to the estimated parameters from the previous iteration for the jth Gaussian. Now the iterative update rules of the EM algorithm for the Gaussian mixture become:

$$\alpha_m = \frac{1}{N} \sum_{i=1}^{N} p(m|x_i, \Theta'), \tag{6.3}$$

$$\mu_m = \frac{\sum_{i=1}^{N} x_i p(m|x_i, \Theta')}{\sum_{i=1}^{N} p(m|x_i, \Theta')}, \tag{6.4}$$

$$\sigma^2{}_m = \frac{\sum_{i=1}^{N} (x_i - \mu_m)^2 p(m|x_i, \Theta')}{\sum_{i=1}^{N} p(m|x_i, \Theta')}. \tag{6.5}$$

However, we keep the means μ_m fixed to the peaks computed from the sample mean distribution, i.e. we are not using Eq. (6.4) at all in our version. Instead we only use the variances $\sigma^2{}_m$ and prior probabilities α_m of the class-wise Gaussians are allowed to change during the EM iteration.

The prior probabilities of the Gaussians determined by the EM algorithm are not used in the classification, but the class-wise Gaussians are assumed to be equally probable. This assumption of equiprobability has been made because the probabilities of actual sea ice classes vary depending on the weather conditions and the stage of development of the sea ice, so they can vary a lot between images. Thus, a very large set of data representing different sea ice conditions would be required to define these parameters better, and probably even then different probabilities should be applied for different ice development conditions.

For our training data of four ScanSAR-Wide mode images, the peak detection algorithm located six peaks, see Fig. 6.1. Also the total pixel value distribution can very well be composed of the six resulting distributions, the coefficient of determination was $R^2 = 0.996$.

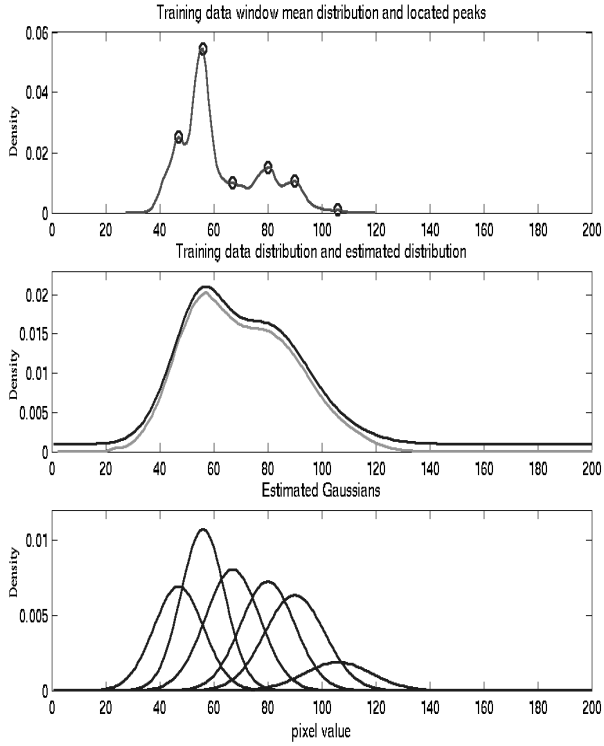

Figure 6.1: Distribution of averaged window means for our training data. Six peaks, shown by dots in the figure, were located by the peak finding algorithm (upper panel). The total pixel value distribution of the training data and the Gaussian mixture of the six estimated Gaussians, the mixture curve has been lifted a little to make curves non-overlapping (middle panel). The six Gaussians forming the mixture (bottom panel).

6.2 Pulse-Coupled Neural Network and Segmentation Network

Pulse-Coupled Neural Network algorithm [57, 103, 149, 188] is an iterative algorithm in which a binary output image is produced at each iteration. The output images at different iterations typically represent some segments or edges of the input image. The PCNN has a neuron corresponding to each pixel of the input image. One PCNN processing element consists of sub-elements: the feeding element F, the linking element L, the internal activation element U, and the output element O. The input stimulus is received by the feeding element and the internal activation element combines the feeding element with the linking element. The value of the internal activation element is compared to a dynamic threshold which gradually decreases at each iteration. The internal activation element accumulates the signal until it surpasses the dynamic threshold. After that the activation element fires the output element and the dynamic threshold is simultaneously in-

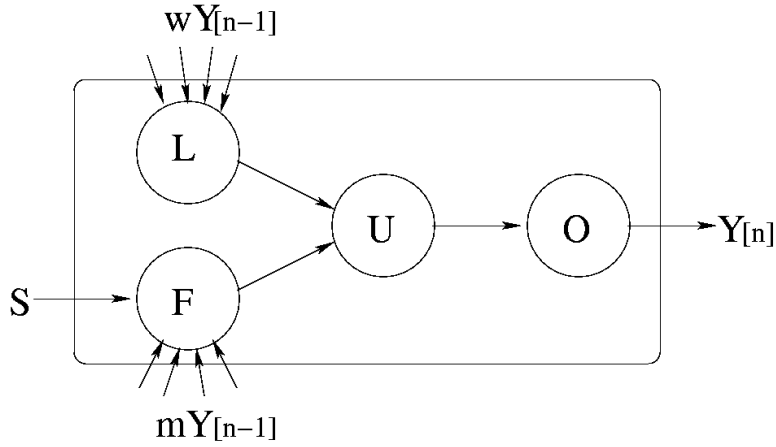

Figure 6.2: One PCNN element is connected to the neighboring elements via the linking L and feeding F.

creased by a large value. The output Y of the output neuron is then iteratively fed back to the same element with a delay of one iteration. The network can be implemented by iterating the equations [103, 149]

$$F_{ij}[n] = e^{-\alpha_F \Delta t} F_{ij}[n-1] + V_F \sum_{k,l} m_{ijkl} Y_{kl}[n-1] + S_{ij} \tag{6.6}$$

$$L_{ij}[n] = e^{-\alpha_L \Delta t} L_{ij}[n-1] + V_L \sum_{k,l} w_{ijkl} Y_{kl}[n-1] \tag{6.7}$$

$$U_{ij}[n] = F_{ij}[n](1 + \beta L_{ij}[n]) \tag{6.8}$$

$$Y_{ij}[n] = \begin{cases} 1, & \text{if } U_{ij}[n] > T_{ij}[n] \\ 0, & \text{otherwise} \end{cases} \tag{6.9}$$

$$T_{ij}[n] = e^{-\alpha_T \Delta t} T_{ij}[n-1] + V_T Y_{ij}[n-1]. \tag{6.10}$$

S_{ij} is the stimulus input i.e. the pixel intensity, $F_{ij}[n]$ the feeding portion of the neuron, $L_{ij}[n]$ is the linking, $U_{ij}[n]$ is the internal activity, $Y_{ij}[n]$ is the output and $T_{ij}[n]$ is the dynamic threshold, the indices i and j refer to the pixel row and column coordinates, indices k and l refer to the dislocation in a symmetric neighborhood around a pixel, and n refers to time (number of iteration). β is the PCNN linking parameter, α_F, α_L α_T are parameters related to the feeding, linking and thresholding, respectively. m_{ijkl} and w_{ijkl} refer to two weight functions, which are typically decreasing functions of the distance from the pixel at location (i, j). These functions are called the PCNN kernels. They can e.g. have Gaussian shapes with standard deviations σ_m and σ_w for m and w.

A simplified block diagram of one PCNN element can be seen in Fig. 6.2. There are three potentials V and decay constants α associated with F, L and T. The firing in the binary images produced by the PCNN mainly due to the primary inputs is called the *natural firing*. The second type of firing, which occurs mainly

due to the neighborhood firing at the preceding iterations, we call the *secondary firing* or *excitatory firing*.

Three of the PCNN equations above, namely the equations (6.6)–(6.8), include a contextual component, i.e. the output at a certain pixel location is dependent of the inputs from the neighboring locations in addition to the input from the pixel location itself. All these equations describe a different source mechanism for the contextual information. However, in practice the multitude of the contextual parameters complicates the determination of the parameter values, i.e. the training of the network. Hence one is tempted to simplify the PCNN equations (6.6)–(6.8) by grouping together the contextual parameters. Such re-parametrization and simplification of the PCNN equations was proposed e.g. by Ranganath et al. [181]. In their model the PCNN equations are given in the following form:

$$L_{ij}[n] = \sum_{k,l} w_{ijkl} Y_{kl}[n-1] \tag{6.11}$$

$$U_{ij}[n] = S_{ij}(1 + \beta L_{ij}[n]) \tag{6.12}$$

$$Y_{ij}[n] = \begin{cases} 1, & \text{if } U_{ij}[n] > T_{ij}[n] \\ 0, & \text{otherwise} \end{cases} \tag{6.13}$$

$$T_{ij}[n] = \begin{cases} e^{-\alpha_T \Delta t} T_{ij}[n-1], & \text{if } Y_{ij}[n] = 0 \\ V_T, & \text{if } Y_{ij}[n] = 1. \end{cases} \tag{6.14}$$

$L_{ij}[n]$ is linking from a neighborhood of the pixel at location (i, j), $U_{ij}[n]$ is internal activity at location (i, j), which is dependent on the signal value S_{ij} (pixel value) at (i, j) and linking value, β is the PCNN linking parameter, and $Y_{ij}[n]$ is the output value of the PCNN element at (i, j). $T_{ij}[n]$ is a threshold value. Ranganath et al. called their PCNN network the segmentation network. In general, the segmentation property of PCNNs and segmentation networks is based on the contextual linking.

6.3 Modified Pulse Coupled Neural Network

The PCNN model we have applied is a modification of the original PCNN [57, 149, 188], adapted slightly from the PCNN model of [181], and is implemented by applying iteratively the equations (6.11), (6.12) and (6.13). In our model, however, we use a fixed class-wise threshold value $T_{ij}[n] = T_m$ ($m = 1, ..., M$ refers to the class) instead of a time-varying threshold value. Our algorithm processes the distributions in two class pairs, starting from the class with the highest mean paired with the class with next highest mean, and then continuing to the pair consisting of the classes with second highest mean and third highest mean, and so on. All the adjacent distribution pairs representing the classes are processed pairwise using the PCNN algorithm. For each pair, based on the estimated Gaussian distributions of these two classes, the pixels belonging to the class with higher mean are found using the PCNN algorithm. Only the pixels not classified previously are included in each pairwise classification. For each pair of classes the network is initialized such that all $Y_{ij}[0]$'s are zeros. For class 1 the parameters are defined using PDF of that class only because there is no pair for it.

Because our class distributions are highly overlapping, we can not select β such that perfect segmentation can be achieved (for details, see [127]). Instead, we allow a small classification error, and first select T_m's such that only some minor percentage of the Gaussian with the lower mean are misclassified by the natural firing. In general, for a given error-level

$$T_m = \mu_{m-1} + f_g \sigma_{m-1}, \tag{6.15}$$

f_g is a factor based on the cumulative Gaussian distribution function. For example for 5 % misclassification we have $f_g \approx 1.64$ and thus $T_m \approx \mu_{\text{m-1}} + 1.64\sigma_{\text{m-1}}$, actually this seems to be a suitable value of f_g in practice. This selection must be done such that the amount of mis-classifications is reasonable small and at the same time there are still enough pixels representing the class with higher mean. This ensures that the neural network can locate the segments of the class with higher mean during the PCNN iteration.

We keep the threshold T_m the same for a given number of iterations, and also retain the previously fired values $Y_{\text{ij}}[n]$. At each iteration the pixels fired by the excitatory firing are collected. A suitable amount of iterations in practice is 10–30.

We denote the Gaussian with the higher mean with A and the Gaussian with the lower mean with B and say $A_{\min} = \mu_A - f_g\sigma_A$ and $B_{\min} = \mu_B + f_g\sigma_B$. $B_{\min}$ is also the value of T_m. Then we can select β such that the values of $A_{\min}$ are included into the class A with the minimum accepted linking. We are using the neighborhood with the radius $R = 1.5$ (i.e. a usual 3×3 neighborhood, for details see [127]), with the linking relative to the inverse of the squared distance from the mid-pixel and normalized to one. Now the minimum allowed linking would be $L_{\min} = \frac{1}{6} + \frac{1}{6} + \frac{1}{12} = \frac{5}{12} \approx 0.4167$, and the value of β is chosen to be

$$\beta = \frac{B_{\max} - A_{\min}}{A_{\min} L_{\min}}. \tag{6.16}$$

After the pixels of a class have been collected, the values of $Y_{\text{ij}}[0]$'s are set to zeros, and a new threshold T_m and linking parameter β, based on the class distributions of the next pair of classes, are used and new PCNN iteration is started. This is repeated until all the adjacent class pairs have been processed. For the class with the lowest mean value i.e. $m = 1$, there is not any pair B, so we just set $B_{\max} = \mu_A$ and compute β using this value.

There may still remain some pixels which are not mapped to any class. These pixels are just mapped according to the closest already mapped pixel value in their 8-neighborhood, iteratively if necessary. A block diagram of the algorithm is presented in Fig. 6.3. In practice the only user-adjustable parameter of the algorithm is the allowed error rate in classification defined by the factor f_g. All the other parameters are derived from the data distributions and the value of f_g.

6.4 PCNN and Perfect Segmentation of SAR Data

Perfect image segmentation by PCNN is possible on some conditions, described in detail in [127]. Assuming that we have two segment classes A and B, and the mean

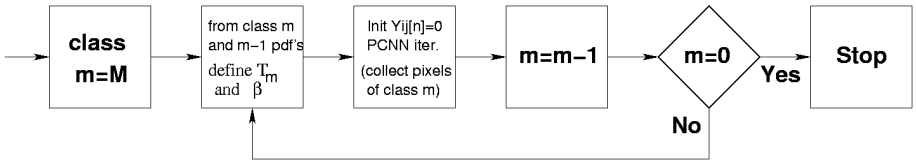

Figure 6.3: Block diagram of the algorithm for the case of M classes. The class means are increasing from class $m = 1$ to class M. The PCNN block runs the PCNN iterations described by Eqs. 6.11–6.13 after initializing $Y_{ij}[n]$'s to zeros.

of A is higher than the mean of B, a condition for selecting the PCNN parameter β for perfect segmentation can be expressed by the equations [127]:

$$A_{\min}(1 + \beta L_{A_{\min}}) \geq A_{\max} \tag{6.17}$$

$$B_{\min}(1 + \beta L_{B_{\min}}) \geq B_{\max} \tag{6.18}$$

$$B_{\max}(1 + \beta L_{B_{\max}}) < A_{\max}. \tag{6.19}$$

L refers for linking here, and the subindex of the linking refers to the maximum or minimum linking in A and B. The first two conditions come from the restriction that all the pixels belonging to the classes A and B must be classified to the class. This means that even with the minimum linking, the minimum value in each class must be classified correctly. The third condition is due to the fact that the maximum value of B even with the maximum linking is not allowed to be classified to A. So, we get limits for the value of β:

$$\beta_{\max} = \frac{\frac{A_{\max}}{B_{\max}} - 1}{L_{B_{\max}}} \tag{6.20}$$

$$\beta_{\min} = \max\left[\frac{\frac{A_{\max}}{A_{\min}} - 1}{L_{A_{\min}}}, \frac{\frac{B_{\max}}{B_{\min}} - 1}{L_{B_{\min}}}\right]. \tag{6.21}$$

Now for the 8-neighborhood case $L_{A_{\min}} = L_{B_{\min}} = 2.5V_t$ and $L_{B_{\max}} = 2V_t$ [127]. If $\beta_{\min} < \beta_{\max}$ perfect segmentation is guaranteed. In our case the classes are however so much overlapping that perfect segmentation is impossible. We can locate the limit where $\beta_{\min} = \beta_{\max}$, and by inserting the values of $L_{A_{\min}}$, $L_{B_{\min}}$ and $L_{B_{\max}}$ into the equation we get

$$\frac{\frac{A_{\max}}{B_{\max}} - 1}{2} = \max\left[\frac{\frac{A_{\max}}{A_{\min}} - 1}{2.5}, \frac{\frac{B_{\max}}{B_{\min}} - 1}{2.5}\right]. \tag{6.22}$$

Based on the assumption of normal distributions, we can set $A_{\min} = \mu_A - f_g\sigma_A$, $A_{\max} = \mu_A + f_g\sigma_A$, $B_{\min} = \mu_B - f_g\sigma_B$, $B_{\max} = \mu_B + f_g\sigma_B$, where the means and variances are estimated from the data, and solve the equation for f_g. For example for our ScanSAR narrow test image data the values of f_g between two adjacent classes varied from 0.611 to 0.918, corresponding to 45.8–60 % of the distribution mass. This shows that even nearly perfect segmentation is impossible.

6.5 Comparison of Some Segmentation Methods for SAR Data

We have tested several segmentation algorithms for our data at FIMR. However, it is impossible to know the actual ground truth, and we can only make visual judgments and comparisons between the segmentation methods. Here some comments on different segmentation methods are given, and also the segmentation results for one SAR image window are presented, to make possible for the reader to compare the segmentations. This SAR image window contains a lot of details and in this sense serves as a good example of highly textured SAR area. The image is the same used in speckle filtering test in section 4.3 and is shown in Fig. 4.6.

Segmentation results for the test image, shown in Fig. 4.6, using different segmentation methods, are shown in Figs. 6.4–6.7, and the execution times are shown in Table 6.1. Also the PCNN segmentation with parameters defined by the perfect segmentation condition are shown for comparison in Fig. 6.4, left panel. The execution times for the perfect segmentation PCNN were similar to that of our PCNN algorithm.

This experiment was performed with a set of Radarsat-1 ScanSAR narrow images using four image windows for training and four image windows for testing. The training for this material only produced four peaks and thus $M = 4$ Gaussians in the decomposition. The parameters (mean μ, and standard deviation σ) of the Gaussians for this material are $(\mu_1, \sigma_1) = (50.64, 13.55)$, $(\mu_2, \sigma_2) = (70.53, 11.16)$, $(\mu_3, \sigma_3) = (93.52, 10.04)$ and $(\mu_4, \sigma_4) = (108.36, 11.61)$. ScanSAR narrow mode data were used because at the time of developing segmentation methods, most of the SAR data were in ScanSAR narrow mode. Some later comparisons [publication 5] for the ScanSAR wide mode data, which is currently our main operational data, show that the method works well for this data too.

6.5.1 Markov Random Field Based Methods

We tested two algorithms that are based on Markov Random Fields (MRFs). These algorithms are based on the dependence of the pixel segmentation class on the neighboring pixel values and on the conditional pixel class probabilities. The neighborhood pixels are described by cliques C_i, which are groups of neighborhood pixels of different shapes and conditional probabilities of the state $s_{k,l}$ at pixel k, l on condition that the neighborhood of pixel at (k, l) has a set of states $S_{k,l}$. Then the discrete conditional probability density function $p(s_{\mathrm{k,l}}|S_{\mathrm{k,l}})$ is

$$p(s_{\mathrm{k,l}}|S_{\mathrm{k,l}}) = \frac{1}{Z_s} \exp(-\frac{1}{T} \sum_{j \in C} F_j(C_j(k, l))). \tag{6.23}$$

C is the set of cliques. Typically simple linear product potential functions F_j for the cliques C_j are used. T is a so-called temperature parameter, and Z_s is a scaling factor such that the sum of the probabilities is unity. The number of clique types grows rapidly as the neighborhood size grows. We have used a 4-pixel neighborhood and three clique types in our experiments.

In the Iterated Conditional Modes (ICM) algorithm [13] the states are initialized to maximum of $p_{s,m}(y(k,l))$, i.e. the conditional density at (k,l) with observation $y(k,l)$ given the state $s_{k,l}$. m is an index referring to the state of M possible states i.e. $m \in \{0,...,M-1\}$ Then the new state is iteratively selected to be maximum of $p_{s,m}(y(k,l))p(s_{k,l}|S_{k,l})$. This is repeated until no changes occur or the states begin to oscillate. The ICM algorithm started to oscillate between classes after some iterations, and we used 10 iterations in our test. In another MRF algorithm based on simulated annealing [69] the segmentation is optimized for the whole image using simulated annealing where the temperature parameter is slowly reduced during the optimization process. This algorithm proved to be very slow to compute.

6.5.2 Edge Detection Based Methods

An edge detection based algorithm presented in [219] by Skriver. This algorithm used gamma distribution testing for edge detection. However, this did not work well for our down-sampled images and we used a gradient-based edge detection instead. This seemed to work better, but still produced too many edges. The situation was improved by using edge thinning and then removing edge segments that were smaller than a given threshold. Then the algorithm computes for each non-edge pixel the distance to the nearest edge pixel to produce a distance image. This computation is performed using a technique known as chamfering [14], where the distance value of a non-edge pixel is computed from its neighbors by adding the neighbor distance to the neighbors' distances from edges and the smallest value is selected to be the distance image value at the pixel location. In this initial segmentation each distance maximum corresponds to a segment. Then a linking i.e. combining of segments close to each other is performed using the linking criterion

$$D_E(m_1,m_2) < \alpha(D(m_1)+D(m_2)). \tag{6.24}$$

D_E is the Euclidean distance between maxima m_1 and m_2, and $D(m_i)$ is the distance function at the location of m_i. α is a constant for which a value of 0.6 was used. Then the segments correspond to each remaining maximum and are labeled. Finally the edges are iteratively merged using a merging criteria based on the segment mean intensity differences of adjacent segments. We have used two merging iterations, which produced visually good result in our experiments. It seems that this kind of segmentation results in all too many small segments, and the merging applied to produce a more reasonable number of segments resulted in visually unsatisfactory segmentation. The algorithm behaved even worse with the original edge detection algorithm proposed in [219] and it is even still not very useful with our simpler edge detection algorithm.

6.5.3 Comparison Results

The results of the comparisons are collected here. The execution times are shown in Table 6.1, and the segmentation results for the used test image are shown in Figs. 6.4–6.7 For comparison, we also tried direct thresholding, using the Bayesian thresholds for the Gaussian distributions describing the classes derived from the

Table 6.1: Execution times of the segmentation algorithms tested. The algorithms were run on a 900 MHz AMD Athlon based computer with 512 MB RAM, and in the Linux operating system. The mean time values and standard deviations are given for a set of eight test images.

Method	Mean time (s)	Standard Dev (s)
PCNN (our method)	20.1	6.24
ICM (MRF)	42.1	0.35
Simul. annealing (MRF)	1238	16.1
Edge-based (Skriver)	314	182
Thresholding	0.25	0.02
Filter + threshold	18.2	2.98

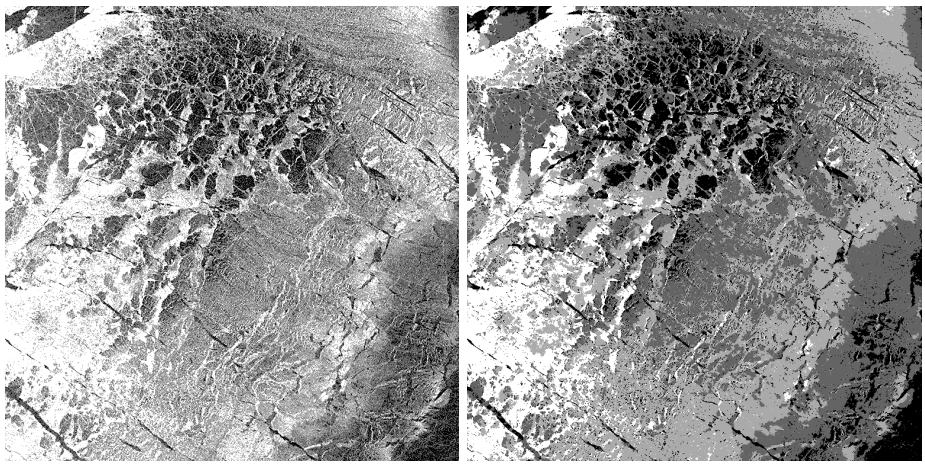

Figure 6.4: PCNN algorithm segmentation using the thresholds at which $\beta_{\min} = \beta_{\max}$, i.e. thresholds of the classes are defined by the perfect segmentation condition (left). Our PCNN algorithm segmentation (right).

training data, and also thresholding after anisotropic diffusion filtering [178]. These results can be seen in Fig. 6.7.

There are quite many possibilities how to perform an intensity-based segmentation for a SAR image. The noise present in our images either requires some filtering or a method that takes the contextual information into account. We have seen that our PCNN algorithm with properly selected parameters gives plausible segmentation results compared to subjective visual segmentations. Also the execution time was reasonable for operational use. The MRF-based models produced quite nice segmentation results, but only the ICM algorithm can be used in practice because the simulated annealing algorithm had far too long execution times for our purposes. Edge-based segmentation either produced some small segments which should have been merged with other segments or merged visually reasonable segments, and the overall segmentation result did not look very good. The adjusting of the parameters for this method proved to be very difficult. Applying anisotropic

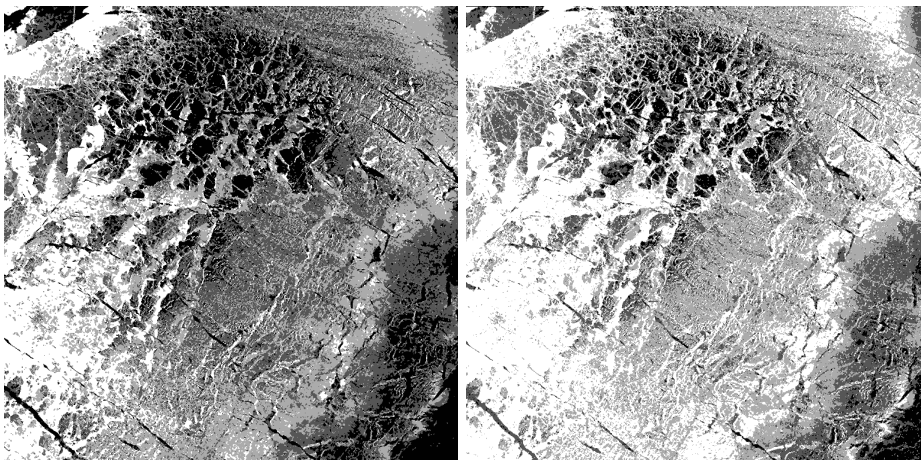

Figure 6.5: ICM (MRF) segmentation for the test image of Fig. 4.6 (left), and simulated annealing (MRF) based segmentation (right).

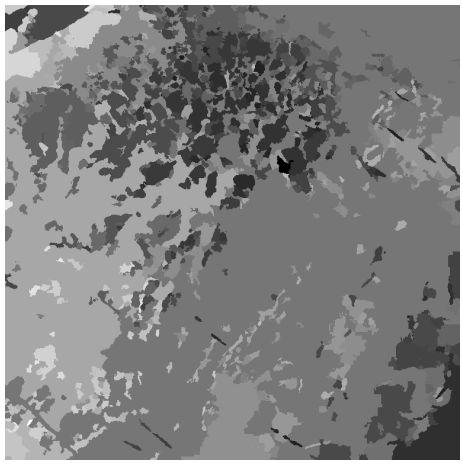

Figure 6.6: Edge-based segmentation, with heavy edge pruning.

diffusion filtering [178] and then thresholding also makes some of the smaller segment boundaries fuzzy.

6.6 Evaluation of PCNN Segmentation Based on Digitized Ice Charts and Visual Interpretation

We have made a statistical comparison between the digitized ice charts and our PCNN-based classification results with $m = 6$ classes. In our experiments with our operational data, Radarsat-1 ScanSAR Wide mode images, we used four Radarsat-1 ScanSAR Wide mode images from the winters 2001–2002 and 2002–2003 for training our algorithm and five Radarsat-1 ScanSAR Wide mode images from the

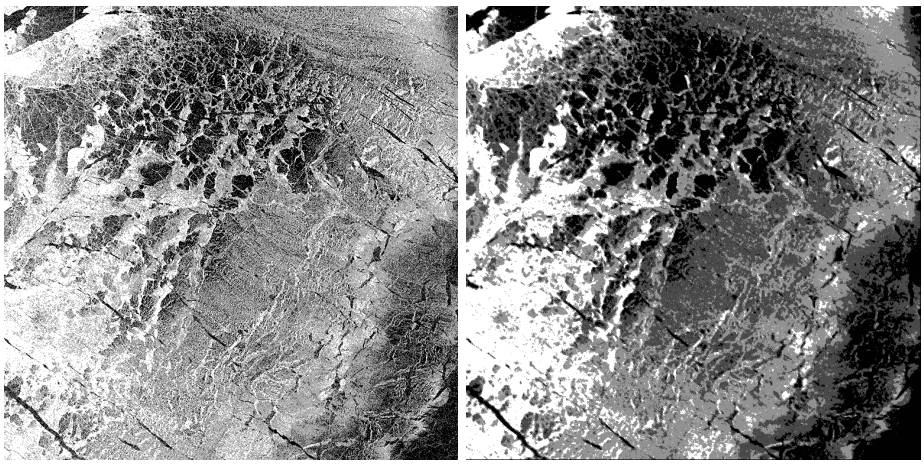

Figure 6.7: Thresholding of the test image (left), and anisotropic diffusion filtering and thresholding (right).

Table 6.2: Class characteristics based on digitized ice charts. The ice types are class-wise modes, the thickness values ($T_{\min}$, T_{mean}, $T_{\max}$) are class-wise means rounded to the closest integer centimeter.

Class	1	2	3	4	5	6
Ice type	LI	LI	LI	CI	CI	CI
$T_{\min}$ (cm)	6	8	13	19	21	19
T_{mean} (cm)	11	14	19	29	31	30
$T_{\max}$ (cm)	17	22	28	41	44	42

same two winters for testing. The digitized ice charts give us the sea ice type, minimum, mean and maximum ice thickness values in a rough scale. The ice types in digitized ice chart are mainly based on ice concentration. The ice types of the digitized ice charts are new ice (NI), level ice (LI), very open ice (VOI, concentration 1/10–3/10), open ice (OI, 4/10–6/10), close ice (CLI, 7/10–8/10), consolidated ice (CI, 9/10–10/10) and fast ice (FI).

We calculated the mode of the ice type for each PCNN-segmented class for our test set of five images. We also calculated means of the minimum, mean and maximum ice thicknesses for each class using the digitized ice charts. The results are shown in Table 6.2. Unfortunately there were only two ice types present in the ice charts for our test set, i.e. level ice and consolidated (deformed) ice.

It should be noticed that especially the ice chart consolidated ice type typically contains many different kinds of segments of different classes, including many areas with high backscattering value. In our classification these are included in class 6.

The geophysical interpretation of the classes is basically just that the degree of deformation (surface roughness) increases as the class mean intensity increases. The

darker areas are less deformed, and the light areas are more deformed ice. In [155] the signatures of different Baltic Sea ice types at C and X bands, for two different incidence angles (23 and 45 degrees), and for two different polarization combinations (HH and VH), were studied, using scatterometer data (HH-polarization class distributions for dry snow condition were shown in Fig. 2.7). The sea ice classification was visually based on the video of the flight lines, and it was compared to some surface measurements for estimating the accuracy of the method. The classes used were based on the operational Baltic Sea ice code [203]. The sea ice classes used in the study are New Ice (NI), Smooth Level Ice (SLI), Rough Level Ice (RSI), Slightly Deformed Ice (SDI), Highly Deformed Ice (HDI), Loose Brash Ice (LBI, does not appear in our test set) and Frozen Brash Ice (FBI). The backscattering intensity means of the classes are increasing in this order, except that NI and SLI have about the same mean, and also HDI and FBI have about the same mean. Because our data is not absolutely calibrated, and the incidence angle is normalized to 35 degrees, direct comparison is difficult. Based on this analysis we can only say that the classes with lowest means are likely to be NI or SLI, the classes with highest means HDI or FBI, and the classes in between RLI or SDI.

Based on visual inspection of our test set we can say some more than based on the scatterometer measurements. According to our visual interpretation and visual comparison with the ice chart for the test images the conclusion is that class 1 mostly represents new ice, class 2 represents smooth level ice, class 3 represents rough level ice. Class 4 mostly contains fast ice and areas of slightly deformed ice, classes 5 and 6 contain fast ice, highly deformed ice areas (scrub fields), and brash ice. The main characteristic that differentiates classes 5 and 6 is that class 6 contains the strongest back-scatterers, i.e. highest ridges and most of the frozen brash ice. It thus seems, based on the visual interpretation, that fast ice is classified to multiple classes. Fast ice classification can, however, be improved based on an algorithm detecting fast ice and then taking into account the probable location of fast ice (shallow coastal areas) as prior information [108]. Also frozen brash ice gives a strong backscattering and will be mixed with the deformed ice areas, and our existing algorithms can not distinguish frozen brash ice from highly deformed ice areas.

As an example, a SAR image, its classification and corresponding ice thickness mean map and ice type map, derived from the digitized ice chart, are shown in Figs. 6.8 and 6.9. The difference between the resolution of the details in SAR classification and ice chart derived maps can clearly be seen in the figure. Many of the ice chart features are only marked with point-wise symbols and it is difficult to exactly locate these manually placed features in the SAR image. For example the bright area in the SAR image of Fig. 6.8 (classified to class 6) near the open sea boundary is frozen brash ice, which is not a segment feature in digitized ice chart, but only indicated with a couple of point-wise symbols.

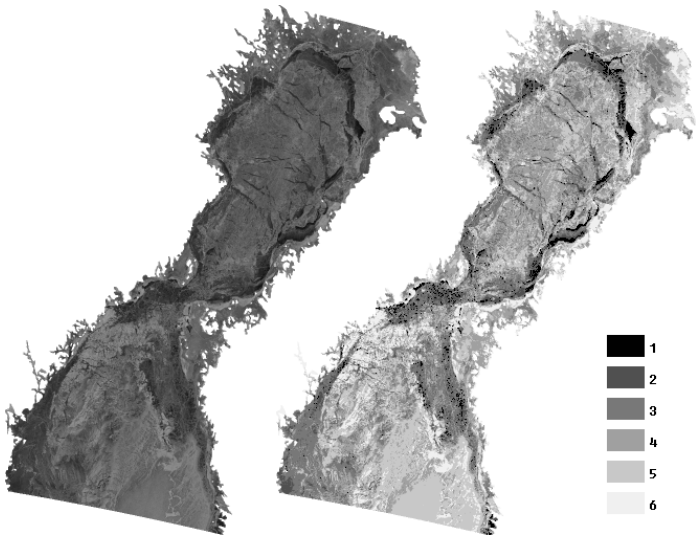

Figure 6.8: A whole SAR image, February 2nd 2003, Gulf of Bothnia, ©Canadian Space Agency, left, with incidence angle correction, and its classification (right), only large scale features are visible in these images.

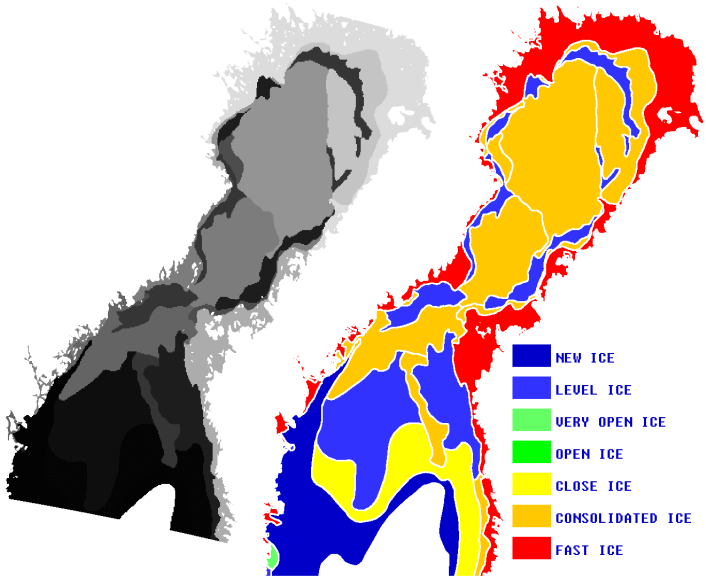

Figure 6.9: Ice mean thickness image (left) and ice type image (right) derived from the digitized ice chart, covering the SAR image in Fig. 6.8. Ice thickness varies from 1 cm (dark) to 50 cm (light), open sea and land appear as white.

6.7 Fast Ice Detection

Fast ice is sea ice which remains fast along the coast, where it is attached to the shore (land fast ice), to an ice wall or an ice front. It may also exist over shoals, or between grounded icebergs [203]. In the Baltic Sea the fast ice is mostly land fast ice connected to land. The fast ice detection [108] is currently based on SAR intensity and the probable location of fast ice. Fast ice is naturally most common in the shallow coastal areas. The PCNN classification is used as a basis for the fast ice detection. Only the areas of the highest and second highest mean are considered to be classified to fast ice. Extra conditions related to their location relative to land are used in the final decision whether a segment represents fast ice or not. The algorithm starts to look for fast ice in these areas from the coast and proceeds toward the normal direction of the coast until it reaches a noticeable edge. This approach with some filtering was tuned for the Radarsat-1 ScanSAR narrow mode images and gave acceptable results. However, a more precise algorithm, based on the ice history, has recently been developed. In this algorithm an approximation of the fast ice area is first taken from the most recent digitized ice chart and updated by the SAR segments in a similar manner as described in Section 8. This is justified because fast ice, as its name suggests, is typically quite stable by nature and the area covered by it does not usually change much in short time interval.

Chapter 7

Texture-Based Classification of Baltic Sea Ice SAR Imagery

The texture of Baltic Sea ice SAR images, excluding uniform areas, mostly contains different types of boundaries, representing ice type edges, leads, ridges and spot-like features (representing smaller details, e.g. small ice segments). To analyze the local content of these features, several methods have been tested at FIMR. We have studied the use of local autocorrelation in open water detection and the results have been promising. The method is presented in this section. Also two categories of texture classification methods based on higher-order statistics are presented. The first one is simply based on detecting edges and spot-like features based on higher than second order moments. The other category of methods consists of utilizing independent component analysis (ICA).

7.1 Open Water Detection from Baltic Sea Ice SAR Imagery

Open water can not be distinguished based on the intensity only because the backscattering from open water varies from very low to very high depending on the waves and the local radar incidence angle. According to our knowledge, the local autocorrelation seems to be a stable measure, with regard to the backscattering strength, to detect open water. By autocorrelation we here denote the estimated autocorrelation function value at a fixed distance. Areas of open water are actually noise-like areas in SAR images, and autocorrelation can be used to measure the existence of regular patterns (texture) in the image. Thus areas with random pixel distribution i.e. with low enough autocorrelation are more probably open water than areas of higher autocorrelation values. For the ideal (Gaussian) white noise the autocorrelation value at any nonzero distance would be zero.

The image to be classified is first segmented and the autocorrelation is computed for the segments rather than for small windows around single pixels. The autocor-

relation of a segment is the mean of the local autocorrelation, computed in a small window, over the segment. The segmentation is based on the SAR intensity after the incidence angle correction [154] [publication 2]. This segmentation is further refined by segmentation based on local autocorrelation.

The computation of the two-dimensional local autocorrelation, here denoted by $C(k,l)$, is carried out by using only the neighboring pixels, i.e. with 2-D lag values $(k,l) = (0,1)$, corresponding to vertical direction, $(k,l) = (1,0)$ corresponding to horizontal direction, $(k,l) = (1,1)$ and $(k,l) = (1,-1)$ corresponding to the diagonal directions. The diagonal direction values are linearly interpolated to the unit distance because their distance from the reference pixel is $\sqrt{2}$. The corrected autocorrelation for the diagonal directions at distance 1 thus becomes $C(k,l) = \frac{C'(k,l)+\sqrt{2}-1}{\sqrt{2}}$, where $C(k,l)$ is the computed diagonal autocorrelation value. The local autocorrelation values computed only from the neighboring 3×3 pixel block exhibit high random fluctuation. To obtain a more reliable estimate for $C(k,l)$, we first compute the autocorrelation in a 11×11 pixel block, here denoted by B, around the center pixel, in the four directions separately. The directional autocorrelation estimate for the lag (k,l) is computed as

$$C(k,l) = \frac{\frac{1}{|B|}\sum_{\mathrm{ij}\in\mathrm{B}} \left(I(i-k,j-l)-\mu_B\right)\left(I(i,j)-\mu_B\right)}{\sigma_B^2}, \tag{7.1}$$

where the $|B|$ denotes the size of the pixel block B, μ_B and σ_B are the sample means and standard deviation in B. Actually, only the pixels inside the segment where the center pixel lies are used in the computation of the directional block autocorrelations. The autocorrelation at the center pixel is then computed as the weighted (by the relative amounts of samples in each direction) mean of the four directional autocorrelations in the block. The autocorrelation of a segment is finally the mean of the values C over the segment.

The threshold applied in the classification for the segment-wise autocorrelation is determined on the basis of training data consisting of Radarsat-1 data and the digitized ice charts of the same days. The digitized ice charts are used as reference data, and by using this data it is possible to estimate the SAR autocorrelation distributions for the open sea and sea ice areas of the ice chart. In the estimation of the autocorrelation distributions, a Gaussian mixture model is used. The number of components in this model is selected such that the coefficient of determination R^2 exceeds a threshold (here 0.95). The expectation-maximization (EM) algorithm is used to estimate the parameters of the components. This approach suggests two components for the open water, and three components for the sea ice distributions. However, based on the small mixing proportion of the weaker open water component, one may assume that the occurrence of this component is due to the different resolutions of the SAR data (100 m) and the ice chart (1 km), i.e. the area boundaries and small details in the ice chart are not of the same precision as in the SAR image. This leads to some misclassification in the finer resolution near the boundaries as well as in the case of isolated ice floes appearing in the middle of open sea. The automated algorithm correctly identifies them as ice, but in the ice charts they are not indicated.

The threshold is chosen to optimize the Bayesian decision rule between two densities, whose prior probabilities sum to one, i.e., the threshold is the point where

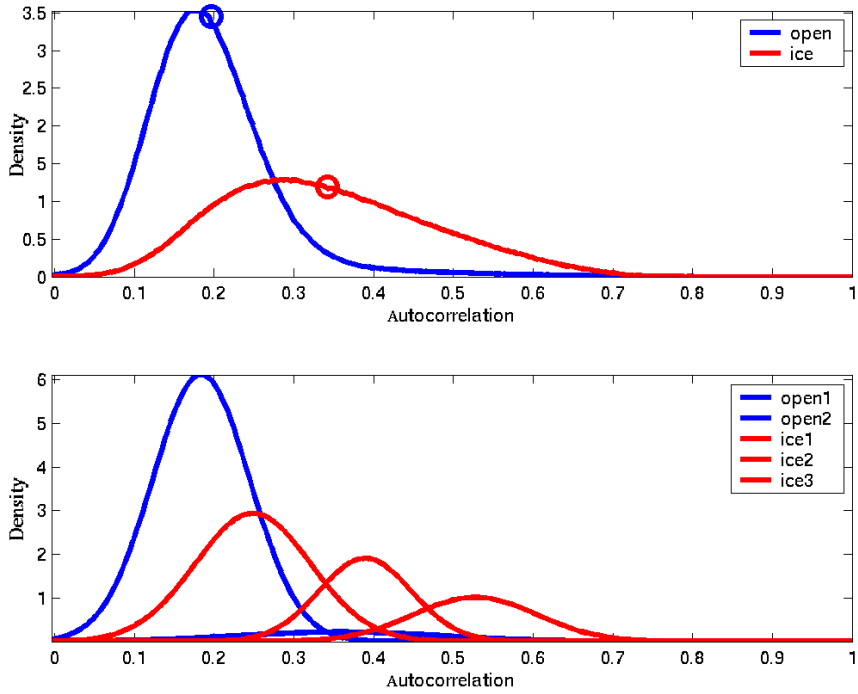

Figure 7.1: The estimated probability density functions of the local autocorrelations C. In the upper panel are shown the PDFs for the training data set, and in the lower panel the corresponding Gaussian components with the estimated mixing proportions. The mean values associated to the distributions are marked with a circle. The open water distributions are drawn with blue and ice distributions with red color.

the two posterior densities are equal. The appropriate densities in this problem are selected with the following procedure. The open water density in the threshold determination is the mixture component with the large mixing proportion. The selected component from the sea ice mixture density is the component with the lowest mean. These densities for the training data are shown in Fig. 7.1, blue color corresponds to open water and red to ice.

Determining the Bayesian threshold in this case leads to a second-order polynomial equation from which the threshold can be solved. We calculated the optimal threshold using two types of prior probabilities for the two distributions, the first type utilized the mixing proportions estimated from the training data set, and the second one the assumption of equiprobability of the distributions. The former assumption gave the threshold value $T_{\mathrm{hi}} = 0.258$ and the equiprobable case the value $T_{\mathrm{lo}} = 0.225$.

The algorithm first uses the lower threshold to define whether a segment certainly contains open water or not. Then it tests the segments adjacent (in the sense of 8-neighborhood) to these open water segments for the upper thresholds. If the neighboring values are less than the upper threshold, the open water area is

Table 7.1: Percentages of correctly classified pixels for the proposed algorithm and for direct autocorrelation thresholding with two threshold values.

Algorithm	Data set	Water (%)	Ice (%)
Proposed algorithm	Train	94.00	81.49
	Test	89.44	81.88
	Wet	91.57	81.06
Threshold T_{lo}	Train	76.09	75.13
	Test	67.10	79.12
Threshold T_{hi}	Train	79.58	68.65
	Test	71.12	74.07

expanded by these segments. The threshold values are always compared to the segment autocorrelation mean values instead of comparing the values computed for small windows around each pixel separately.

Finally a filtering step is performed, and open water segments with size less than a given threshold are set to ice, unless they are long and narrow, corresponding to the typical shape of leads. An example of the open water classification is shown in Fig. 7.2.

7.2 Evaluation of Open Sea Detection

In adjusting our algorithm parameters and testing of the algorithm we used a set of 52 ScanSAR Wide mode images processed by KSAT in Tromsø, Norway. The images were mainly acquired during the winter 2003/2004 while also some images from the winter 2002/2003 were included. The training data set consisted of 20 images from the winter 2003/2004 which mostly represented dry snow condition. Also some wet snow condition images were included. One test data set of 20 images over the winter 2003/2004 was then used to evaluate the performance of the algorithm. These images also mostly represented dry snow conditions. Another test set for wet snow conditions consisting of 12 images from the winters 2002/2003 and 2003/2004 was tested separately.

The classification performance of the algorithm for the training set, the test set, and the wet snow condition test set are shown in Table 7.1. For comparison, also the results of pixel-wise thresholding classification using the lower and upper autocorrelation thresholds T_{lo} and T_{hi} are shown for the training and test sets. Using the proposed algorithm about 90 % of the open water is correctly classified in all conditions, and over 80 % of the ice is correctly classified compared to the information of the digitized ice charts of the same day.

However, when we compare what kind of ice is misclassified in the wet and dry snow conditions, there are clear differences. In the dry snow conditions most of the ice classified to open water is thin ice, but in wet ice conditions most of the misclassified ice is rather thick, see Fig. 7.3. According to visual interpretation, the misclassified open water areas are typically areas with some floating ice producing

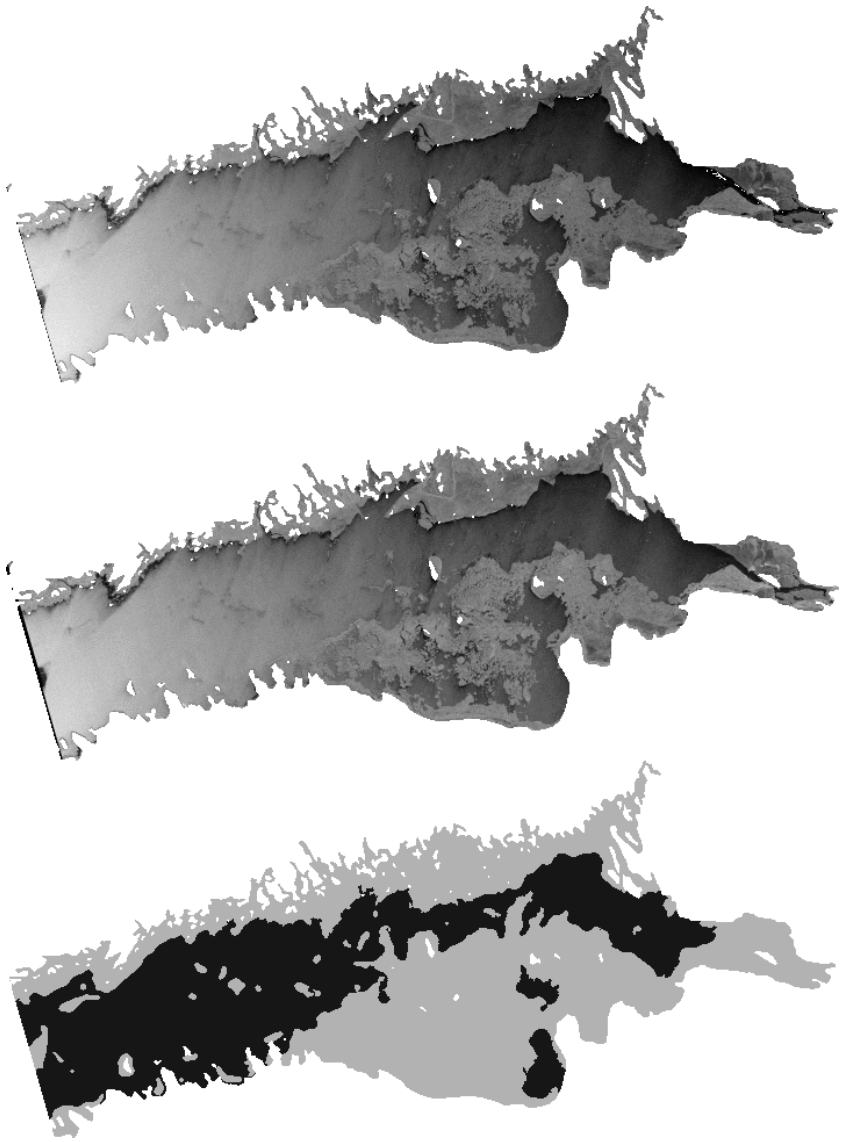

Figure 7.2: An example of open water detection (Gulf of Finland, April 1st 2004). The clear changes in open water backscattering as a function of the incidence angle can be seen in the SAR image (©European Space Agency (ESA), top), the backscattering is significantly higher at lower incidence angles. The incidence angle correction (middle) does not change this much. The classification (bottom) locates the open water areas (shown with a dark gray tone) quite well. It can also be seen that the algorithm is sensitive to small ice floats and classifies open water with floats as ice.

higher local autocorrelation. Two examples of the classification are shown in Figs. 7.4–7.7. The SAR image in Fig. 7.4 is from the ice melting period representing

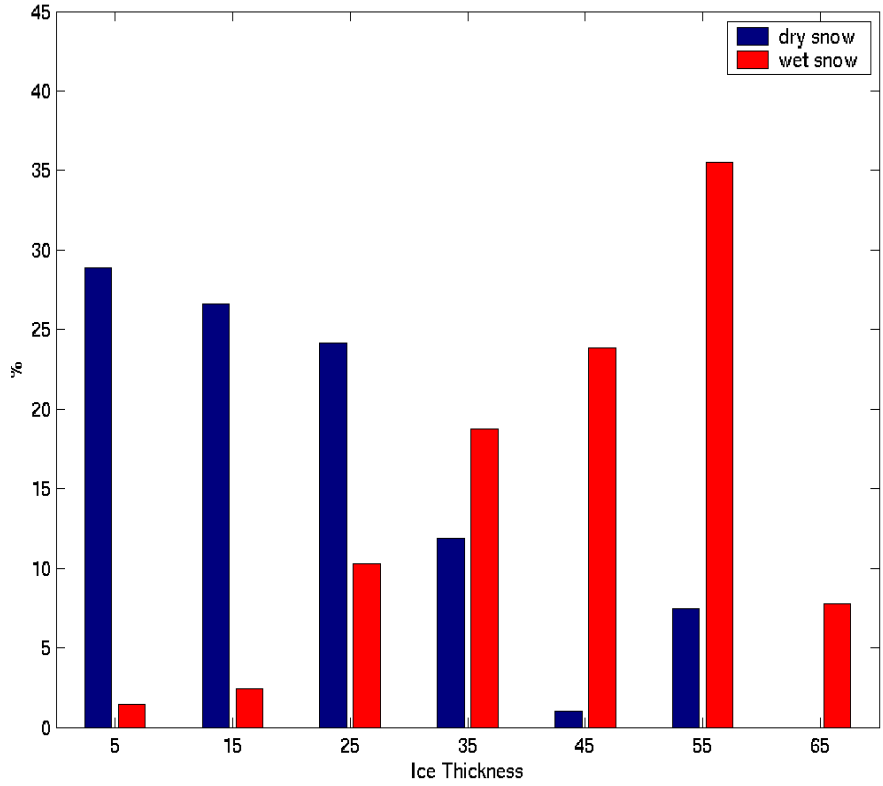

Figure 7.3: Proportions of the misclassified ice in different ice thickness classes.

wet snow conditions, the average snow cover thickness at that time was around 5–10 cm in the Finnish coastal stations of Bay of Bothnia. The SAR image of Fig. 7.6 and its classification result in Fig. 7.7 are from a colder period when the snow cover thickness in the Finnish coastal stations of Gulf of Finland was 30–45 cm.

It can be seen that the shape of the open water and sea ice edge in the classification result is more detailed, causing some difference to the ice charts. There are also some areas of thin ice, according to the ice chart, which are classified as open sea. Also the edges of the SAR beam often cause misclassification of open water as sea ice. This can be seen as the straight lines of the ice class in the open water areas of Figs. 7.4 and 7.5).

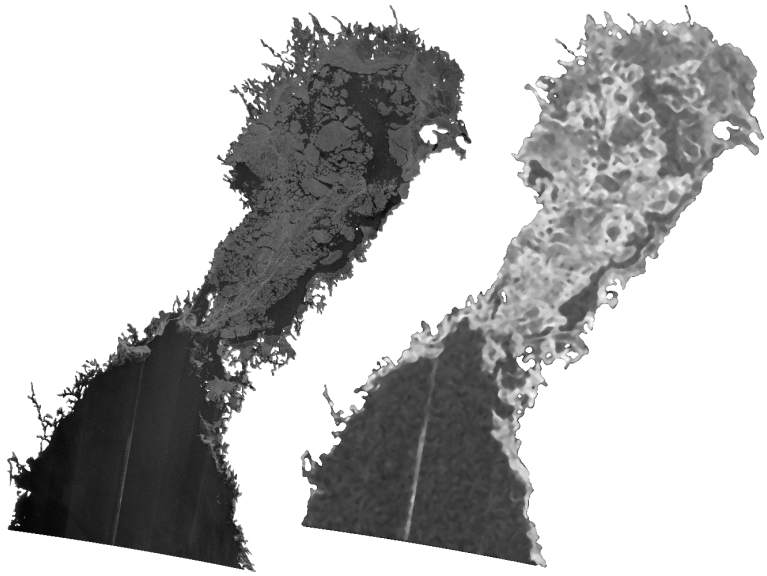

Figure 7.4: A SAR image, April 29th 2003, Gulf of Bothnia, ©Canadian Space Agency (CSA), left. Local autocorrelation (smoothed) over the SAR image, right.

Figure 7.5: Open sea (darker gray tone) and ice in the area of the SAR image in Fig. 7.4 according to the ice chart, left. Open sea and ice in the area of the SAR image in Fig. 7.4 according to our algorithm, right.

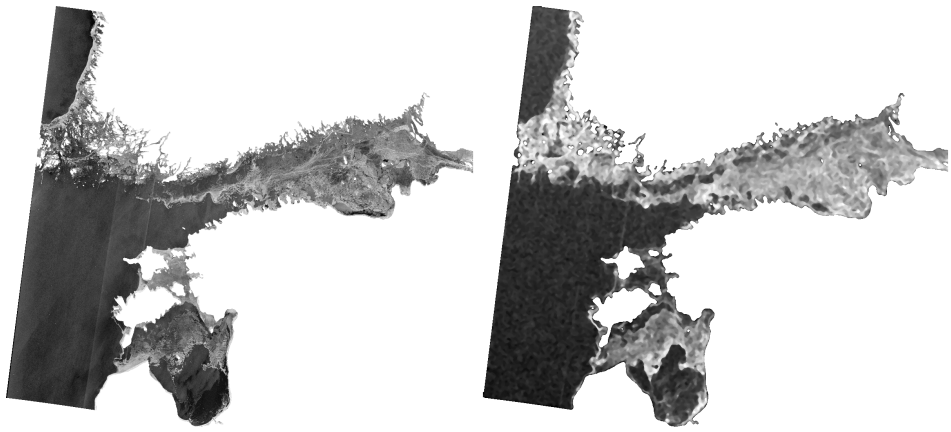

Figure 7.6: A SAR image, February 15th 2004, Gulf of Finland, ©Canadian Space Agency (CSA), left. Local autocorrelation (smoothed) over the SAR image, right.

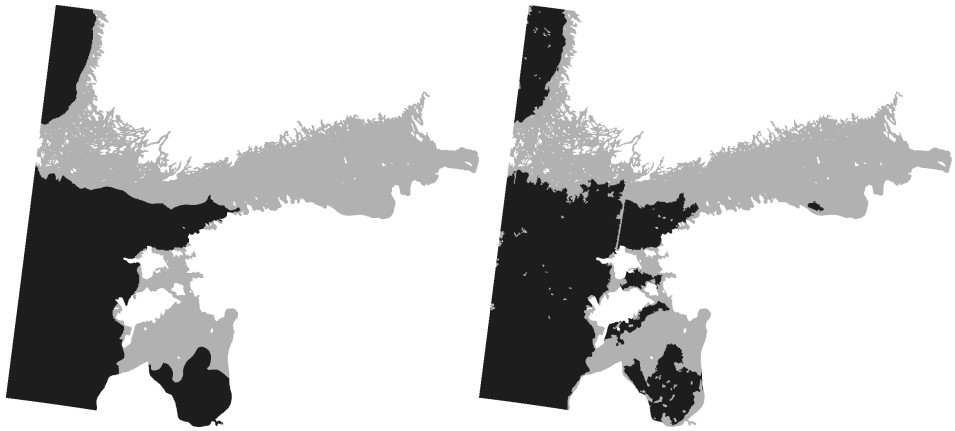

Figure 7.7: Open sea (darker gray tone) and ice in the area of SAR image in Fig. 7.6, according to the ice chart, left. Open sea and ice according to our algorithm, right.

7.3 Sea Ice SAR Texture Feature Detection Based on Higher Moments

Edges, i.e. ice deformations and boundaries of different ice types and open water are an essential feature in Baltic Sea ice SAR images. Another essential type of feature are in our SAR scale small spot-wise features typically representing local deformations or small open areas. To detect these kinds of features we have studied the use of local higher moments. Segment-wise statistics of these features can then be used for texture classification of the segments. The segmentation can be done e.g. using our PCNN segmentation algorithm.

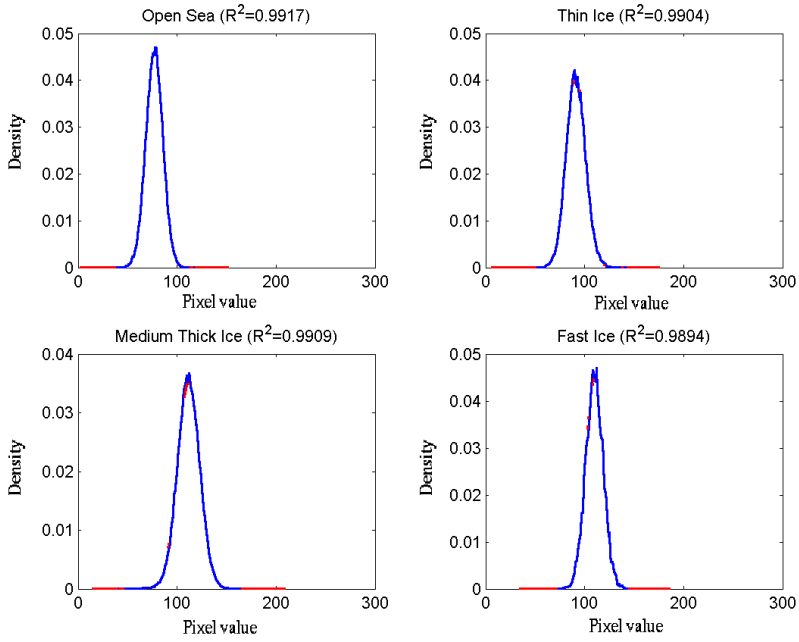

Figure 7.8: Fitting Gaussian distributions to SAR data windows from uniform image areas representing different types of sea ice, or open water. The estimated Gaussians and normalized histograms derived from the data fit very well. The distributions for filtered data are typically narrower Gaussians.

The moment-based feature detection method assumes Gaussian distributions of the SAR pixel values inside uniform image areas, image segments. We have made some experimental studies, fitting Gaussian distributions to PDFs estimated from our SAR data (100 m resolution, logarithmic intensity values), and have observed that the distributions are practically Gaussian ones. In Fig. 7.8, the blue curves are the data PDFs and the red ones are the estimated Gaussians. In these areas the Gaussian statistics gives most of the statistical information available in the SAR image. However, in deformed ice fields the statistics significantly differs from the Gaussian statistics (see Fig. 7.9). In our feature detection approach, in addition to the usual Gaussian statistics, i.e. mean and standard deviation, also higher-order statistics are computed in a round-shaped sliding window around each SAR image pixel. The values we use are the normalized skewness and kurtosis values, which are normalized versions of the third and fourth order moments, skewness M_3 and kurtosis M_4. The estimate of the k'th moment from N samples x_i is computed as

$$m_k = \frac{1}{N}\sum_{i=1}^{N}(x_i - \mu)^k. \tag{7.2}$$

The sample mean (1st moment) is denoted by $\mu = m_1$ and the sample variance (2nd moment) by $\sigma^2 = m_2$. The sample estimates for the normalized third and

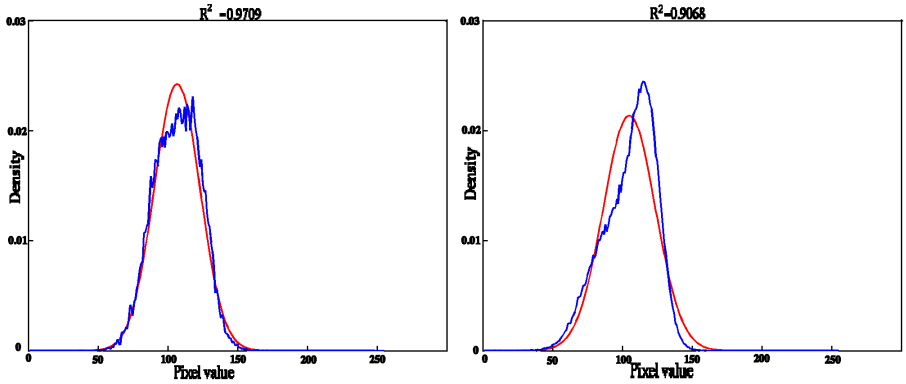

Figure 7.9: Fitting Gaussian distributions to SAR data windows from image areas representing deformed ice. The histograms significantly differ from the Gaussians fit to them.

fourth moments, skewness M_3, and kurtosis M_4, are computed as

$$M_3 = \frac{m_3}{\sigma^3} \tag{7.3}$$

$$M_4 = \frac{m_4}{\sigma^4} - 3. \tag{7.4}$$

The values x_i consist of pixel values in an image window around a pixel. The normalization is such that both skewness and kurtosis are zero-valued for a Gaussian distribution.

The detection of edges between larger uniform areas is based on the fact that the sign of the skewness of the data window changes when crossing the edge, being close to zero at the edge and having higher absolute value further away from the edge. We can think the intensity distribution of the sliding data window near an edge as a bimodal two-component distribution, consisting of the mixture of the uniform area distributions on both sides of the edge. On both sides the mixture distribution is dominated by one component, while at the edge the contribution of both components to the mixture distribution is even. The dominant distribution has a heavier tail on the side of the minority distribution. This implies that the direction of the heavier tail changes to the opposite side at the edge. Hence, the sign of the skewness changes. The skewness has zero value at the edge, but also inside a Gaussian segment this statistic mostly has a value close to zero. To avoid from including these non-edge locations, we use the fourth moment of the distribution. For an edge we require that the kurtosis is less than a given threshold $T \leq 0$, indicating a sub-Gaussian distribution, as multi-modal distributions, like the bimodal distribution at an edge, typically are sub-Gaussian ones, see Fig. 7.10.

For spot-like features, the absolute value of the skewness is required to exceed a given threshold value. This indicates a heavier tail, which results from the pixel values of the spot-like feature, on one side of the dominating Gaussian distribution, i.e. background pixels. Because the moments of a distribution can be similar to

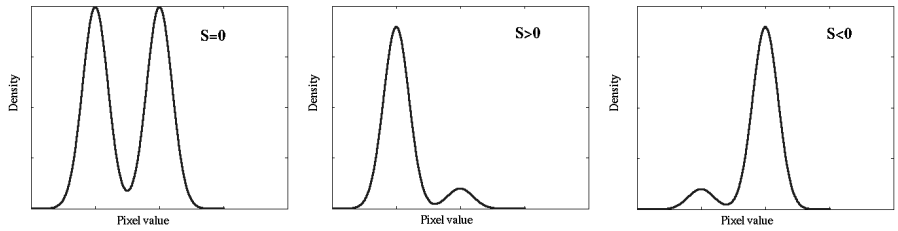

Figure 7.10: The skewness near an edge is close to zero. In the leftmost image is shown an ideal case with two Gaussian distributions, with the same variance, exactly at the edge. The middle and right images describe the distribution and skewness on both sides of the edge.

those of a point at a distance from an edge, we additionally require the local gradient magnitude to be centered close to the window center. Additional conditions for the kurtosis can be used to get more information about the feature. In practice also a threshold for the standard deviation value is used to find areas where the higher-order statistics thresholding is then applied to precisely locate the desired features. This also reduces the amount of required computation.

7.4 Some Experimental Results with Method Based on Higher Moments

Originally we intended to use the method in SAR segment classification. We tried classification based on locating the edges and spot-like features in each segment and computing edge and spot-like feature statistics per unit area. However, this approach was not very successful. We have used this kind of feature detection for two purposes. In our classification algorithm [publication 1], based on the Independent Component Analysis (ICA) [94], we need to select the training data representing non-Gaussian image windows, which are just around the features detected by the algorithm. Another application is to find candidate locations for matching areas in two successive SAR images to get information about sea ice movement. In the left panel of Fig. 7.11 we show an example of the feature detection with a relative large open sea area on the left and sea ice on the right side of the image. There is e.g. probably a ship, shown as a bright spot, in the upper open sea area, and it is detected as a spot-like feature. In Fig. 7.11 the feature detection has been applied directly to the SAR data. However, we noticed that applying e.g. anisotropic diffusion filtering before feature detection reduces the speckle-caused possible mis-detections. The filtered image and the feature detection result for it are shown in the right panel of Fig. 7.11. It can be seen that the potential ship is the only detected spot-like feature in the open see area.

A compromise must be made in the sample window size, large windows loose features, and using smaller windows leads to false detections because of the noise. For unfiltered images we have used a slightly larger window size. We have used window diameter sizes of 7–9 for the filtered data and 9–13 for the unfiltered SAR

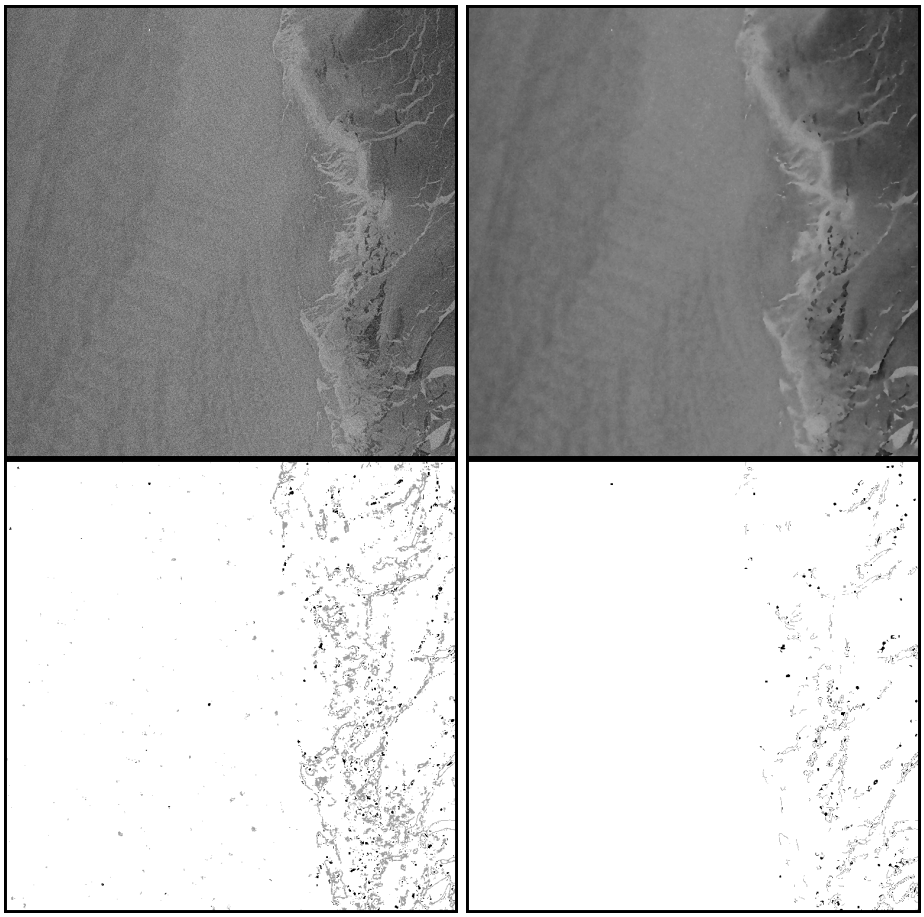

Figure 7.11: The detection of edges and spot-like features (lower left image) applied to the original SAR data (upper left image, ©Canadian Space Agency (CSA)). A filtered version of the SAR image (upper right image), and edges and spot-like features detected (lower right image). Here the parameters are selected such that only strong features are detected and very few "false alarms" occur. The ship in the upper part of the open sea area is correctly detected as a point-like target.

data. The image in Fig. 7.11 is a good example because it shows both uniform, speckled area (open sea on the left) and some deformed ice with clear features (on the right).

7.5 Independent Component Analysis

The Independent Component Analysis (ICA) is a statistical data analysis method that has gained popularity during the last decade. In ICA the measured sample vectors are thought to be linear mixtures of some underlying signals. These un-

derlying signals (basis vectors) are determined adaptively from a large collection of sample signals of interest. The only assumption is that the coordinates of a given signal in the ICA basis are statistically independent [22, 98, 99]. It has been noted that in practice the application of the ICA basis usually leads to a sparse representation of a given signal, i.e., the representation contains only relatively few basis vectors. A characteristic feature of the ICA is that the set of basis vectors used in the representation change from one sample signal to another, unlike in the Principal Component Analysis (PCA).

The ICA model can be expressed as

$$\mathbf{x} = \mathbf{A}\mathbf{s}, \tag{7.5}$$

where $\mathbf{x}$ with elements $x_1, ..., x_n$ is the measured data, $\mathbf{A}$ is the $n \times n$ unknown basis vector matrix and $\mathbf{s} = (s_i)$, $i \in 1, ..., n$ contains the unknown independent components which are the coordinates of $\mathbf{x}$ in the basis given by $\mathbf{A}$. The estimation in the model (7.5) is performed by trying to find a solution, or rather, an approximative solution, for the problem

$$\mathbf{y} = \mathbf{B}\mathbf{x}, \tag{7.6}$$

where $\mathbf{y} = (y_1, \ldots, y_n)^T$ are independent and, thus, the same as s_i's.

The mutual information I is chosen as a measure of dependence. It is defined for a vector $\mathbf{y}$ as

$$I(\mathbf{y}) = \sum_{i=1}^{n} H(y_i) - H(\mathbf{y}), \tag{7.7}$$

where H refers to the differential entropy of a random variable. A direct computation of (7.7) shows that the joint distribution of $\mathbf{y}$ and the product distribution of the marginal distributions of y_i are equal if $I = 0$. In this case the random variables y_i are independent. Hence, one can base the ICA algorithm on search of such mapping $\mathbf{B}$ that $\mathbf{y} = \mathbf{B}\mathbf{x}$ and the mutual information between y_i is minimized. It can shown [99] that to find such a mapping $\mathbf{B}$ is equivalent to maximizing the non-Gaussianity of the y_i. On this principle is built the FastICA algorithm [94] which we have been using.

Whitening of the input data is performed as a preprocessing step, making the computations much easier by removing pairwise correlations and making the separating matrix $\mathbf{W}$ in the whitened coordinate system orthogonal (thus having only $n(n-1)/2$ free parameters for an $n \times n$ orthogonal matrix).

It can be shown, e.g. by the well-known Lagrangian method, that for a function $F(\mathbf{w})$, on the condition $\mathbf{w}$ is on the unit sphere, i.e. $||\mathbf{w}|| = \mathbf{1}$, the gradient at the maximum points to the same (or opposite) direction as $\mathbf{w}$. The derivation of a family of fixed point algorithms, known as FastICA, is based on this. The algorithms simply iteratively update $\mathbf{w}$ to be the gradient of the selected measure of non-Gaussianity, and then normalizing $\mathbf{w}$ at each iteration such that $||\mathbf{w}|| = \mathbf{1}$. For maximizing negentropy the update rule becomes:

$$\mathbf{w} \leftarrow E\{\mathbf{x}g(\mathbf{w}^T\mathbf{x})\} - E\{g'(\mathbf{w}^T\mathbf{x})\}\mathbf{w}, \tag{7.8}$$

where g is a scalar function which is the derivative of a non-quadratic function G used in the estimate of negentropy [95] and g' is the derivative of g. The expectation

operations E should in practice be replaced with the corresponding sample means. This algorithm has at least a quadratic convergence and no adjustable parameters.

The algorithm presented above is a way to find one independent component (IC). To find multiple ICs we first note that for whitened data the separating vectors w_i corresponding to different ICs are mutually orthogonal. This leads to an implementation where after each iteration we orthogonalize the components w_i. In practice we do this using the symmetric orthogonalization, in which no vectors are privileged over other (which is the case in e.g. Gram-Schmidt orthogonalization [3]): let $\mathbf{A^{-1}} = \mathbf{W} = (\mathbf{WW^T})^{-\frac{1}{2}}\mathbf{W}$ where $(\mathbf{WW^T})^{-\frac{1}{2}} = (\mathbf{F\Lambda F^T})^{-\frac{1}{2}} = \mathbf{F\Lambda}^{-\frac{1}{2}}\mathbf{F^T}$ i.e. we utilize the eigenvalue decomposition $\mathbf{F\Lambda F^T}$ of $\mathbf{WW^T}$ where $\mathbf{\Lambda}$ is a diagonal matrix. Sometimes the dimension of the IC problem is reduced after the whitening phase, using only n_r ($< n$) whitened basis vectors corresponding to directions of highest variances, i.e. principal components corresponding to highest eigenvalues.

We have used two categories of methods utilizing ICA. The first one is to use predefined sea ice classes and then computing ICs for these classes separately. These classes are defined by the sea ice surface roughness, for more information about Baltic Sea ice typing see Section 2.4. In the other category of methods the sea ice classes are considered as unknown and feature vector clustering is used to generate a set of sea ice classes from the training data.

7.6 Pixel-Wise ICA-Based Classification

To measure the similarity between a basis vector $\mathbf{b_i}$ and an image window $\mathbf{x}$ we used a normalized ICA coefficient

$$S_i(x) = \frac{|\mathbf{x}^T\mathbf{b}_i|}{|\mathbf{x}||\mathbf{b}_i|} = |\cos(\alpha)|, \tag{7.9}$$

where i is an index to the set of basis vectors $\{1, ..., n\}$. Above α can be interpreted as the angle between the vectors $\mathbf{x}$ and $\mathbf{b}_i$. Then we select the basis vectors best discriminating the classes using a criterion function r to be maximized over all the basis vectors. We use the criterion r_1 of the form (adopted from [54])

$$r_1(k) = \frac{\sigma_{\text{between}}(k)}{\sigma_{\text{within}}(k)}. \tag{7.10}$$

Here $\sigma_{\text{between}}(k) = \sum_j(\overline{a}_{jk} - \overline{a}_k)^2$ is the variance of the j class means corresponding to a basis vector with index k and $\sigma_{\text{within}}(k) = \sum_j\sum_i(a_{ijk} - \overline{a}_{jk})^2$ is the sum of variances within each class. k is an index referring to the kth basis vector. The values of $r_1(k)$ are computed for the ICA coefficients. We selected 100 best distinguishing vectors by using this procedure.

Another measure to select the vectors we have used is related to the tail part of the frequency distribution of the ICA coefficients S_i. We examined the quantity

$$r_2(c, i) = \#\{S_i^c | S_i^c > T\}/N^c, \tag{7.11}$$

where c refers to the class of the learning samples, $c \in \{1, \ldots, N_C\}$ and N^c is the amount of the training samples from the class c and T is a threshold value. If the

difference $r_2(c_1, i) - r_2(c_2, i)$ is large enough for some pair of classes $\{c_1, c_2\}$, the basis vector i is regarded as a good discriminator and the vector is used in the classification. Then a larger set of vectors is generated from the selected vectors. This is done by rotating each of the selected basis vectors in multiples of a given angle, say β. For example $\beta = \pi/4$ will produce eight vectors corresponding to each initial vector. This extended set of vectors can then be used in the classification procedure. We have studied the methods described in the following three subsections.

7.6.1 KNN-Based Classification

The KNN algorithm [37] is based on collecting prototypes (typical feature vectors) representing the classes. This is the so-called training phase. In classification the data vectors to be classified are compared to the prototypes, and the class of a data vector is decided based on the k smallest distances from the class prototypes.

In our implementation, some prototype vectors are randomly selected from the data classes in the training phase, and the normalized ICA coefficients of these vectors are computed. In the classification phase, the normalized ICA coefficient with each basis vector is computed, and then compared in the Euclidean sense with the prototype vectors' coefficients. Denoting the ith prototype ICA coefficient vector with $\mathbf{a}_i$ and the ICA coefficient vector of image window with $\mathbf{b}$, we get for the Euclidean distance

$$D_E(a_i, b) = \sqrt{\sum_{j=1}^{n} (a_{\mathrm{ij}} - b_j)^2}. \tag{7.12}$$

In the algorithm we find k smallest Euclidean distances D_E, and then by voting decide the class, i.e. the class of the window is the class which occurs most frequently in the k selected prototypes. If there is a draw situation, the most deformed ice class used in the classification scheme (navigationally the most difficult of the candidates) is selected.

The other version of the KNN algorithm tested computes an estimate of the ice thicknesses, given the mean ice thicknesses of the classes. The ice thickness estimate is computed as

$$T_{ice}(b) = \frac{\sum_{i=1}^{k} \frac{T_i}{D_i^2(a_i,b)}}{\sum_{i=1}^{k} \frac{1}{D_i^2(a_i,b)}}, \tag{7.13}$$

where T_i is the mean thickness of the class of the ith best matching prototype.

In KNN-based methods, the image window intensity information (mean) is appended to the feature vector used in classification and weighted with appropriate weights to weight both the ICA coefficients and the mean value suitably for our classification task. In our experiments these weights were selected experimentally based on training data.

7.6.2 PDF-Based Classification

In PDF-based classification the probability densities of the ICA coefficients are first estimated and based on these estimated PDFs, the most probable class is selected for each data window to be classified. For every class c, the PDFs of the coefficients are estimated separately for each basis vector $\mathbf{b}_i^c$ of that class by using the set of image windows $\{\mathbf{x}\}$ drawn from the training data. The estimation is performed by applying a Gaussian kernel. The resulting PDF is denoted with $p(S_i^c(\mathbf{x}))$. To classify a vector $\mathbf{z}$ (an image window), we first find m (a predefined value) largest values of $S_i^c(z)$ separately for every class c. Then, we compute the probability $p^c(S(\mathbf{z}))$ using the estimated PDFs of the m best matching base vectors $\mathbf{b}_i^c$

$$p^c(S(\mathbf{z})) = \prod_{i=1}^{m} p(S_i^c(\mathbf{z})). \tag{7.14}$$

The class for $\mathbf{z}$ is selected as the one which has the maximum probability $p^c(S(\mathbf{z}))$ among all the classes. Also the class-wise intensity distributions are computed in the training phase, and the intensity probabilities can be used in the classification like the ICA coefficient probabilities, with an appropriate weighting between the ICA coefficient and the mean. However, in practice, a weighted sum of the probabilities seems to work better because even one almost zero probability can cause the product to be close to zero. Then the criterion becomes

$$p^c(S(\mathbf{z})) = \sum_{i=1}^{m} w_i p(S_i^c(\mathbf{z})), \tag{7.15}$$

where w_i's are weighting factors which are experimentally selected based on training data. Then the classification rule is: Select the class $\hat{c}$ where

$$p^{\hat{c}}(\mathbf{z}) = \max_c p^c(S(\mathbf{z})). \tag{7.16}$$

We have also tested some voting-based variants of the PDF methods. In these methods we compute the class-wise ICA coefficient probabilities for all the basis vectors, and increase the vote count of the class corresponding to the highest probability. The classification for the data window is then the class with the highest vote count. In another variant, instead of the votes the absolute values of the ICA coefficients are used (i.e. the votes are weighted with the absolute ICA coefficient values) for the class corresponding to the highest probability. Instead of voting, summing the probabilities, or absolute ICA coefficient values weighted by the probabilities could also be used.

7.6.3 Direct Classification Based on ICA Coefficient Magnitudes

In direct ICA coefficient magnitude based classification a data window is classified based on the absolute magnitude of the ICA coefficients by selecting the class corresponding to the largest sum of absolute ICA coefficients. The sums of the absolute values of the ICA coefficients are computed for each class (index $k =$

$1, ..., N_C$) based on the labeling of the basis vectors over all the basis vectors:

$$\Sigma_k = w_k \sum_{i=1}^{n} \{|S_i| \mid |S_i| > T, \ \text{class}(i) = k\}. \tag{7.17}$$

The method can be adjusted using the weight coefficients w_k, which can be selected experimentally based on training data, by default they are all set to ones. The class c of the image window is selected to be the class corresponding to maximum Σ_k:

$$c = \arg\max_k(\Sigma_k). \tag{7.18}$$

The image window mean intensity I can be taken into account using Σ_k^I instead of Σ_k:

$$\Sigma_k^I = \Sigma_k \ (p_k(I))^{\alpha_I}. \tag{7.19}$$

$p_k(I)$ is the intensity PDF value for class k at I and α_I is a properly selected parameter, here called as intensity factor, which is selected experimentally, based on training data.

7.7 ICA-Based Classification of Well-Known Textures

The methods were first tested by using a set of Brodatz textures from [16]. We used six different textures, numbers 17, 21, 34, 38, 77 and 93 in [16] here denoted by D17, D21, D34, D38, D77 and D93. These textures represent both very regular patterns and on the other hand also more irregular patterns. The test image used in classification tests containing all of the six textures is shown in Fig. 7.12. The size of the original texture images was 640×640 pixels, and we used one half of each image for training and the other half for testing the algorithm, i.e. 640×320 pixel images.

The results are presented here for the method directly based on ICA coefficient magnitudes. The more complex methods did not give any significant improvement. The sets of basis vectors were not expanded by rotations because the rotations in Brodatz textures are quite limited, and they did not improve the classification significantly, but only increased the amount of computation. We used one half of the textures for training and the other half for testing. An example of ICA bases generated by two of these textures is shown in Fig. 7.13.

We used round-shaped windows with a diameter of 13 pixels in our test. The length of the input vectors were $n = 145$. From the sets of basis vectors the ICA coefficient magnitude algorithm selected vectors (20 representing each texture class or basis) which were used in the classification procedure, i.e. the total number of basis vectors for six classes became $N_b = 120$. The classification results are concluded in Table 7.2 and an example of classification (with the intensity factor $\alpha_I = 0.2$) is shown in Fig. 7.14. The results for these textures were very promising, especially because two of the textures, i.e. D38 and D93 contained some similar patterns visible in our SAR images. There was one larger area in D93 misclassified

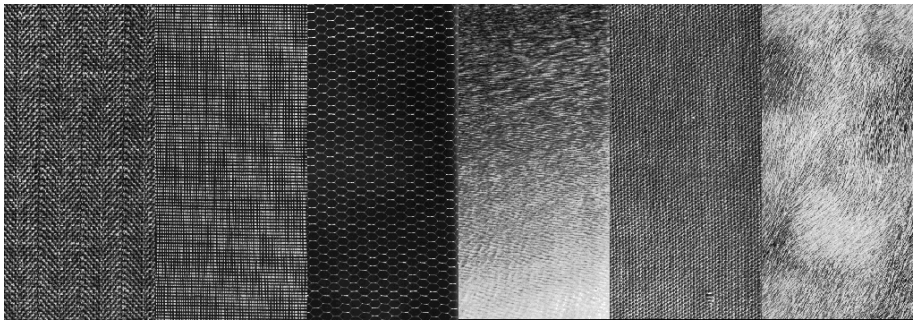

Figure 7.12: Brodatz textures used in classification tests. From left to right textures D17, D21, D34, D38, D77 and D93.

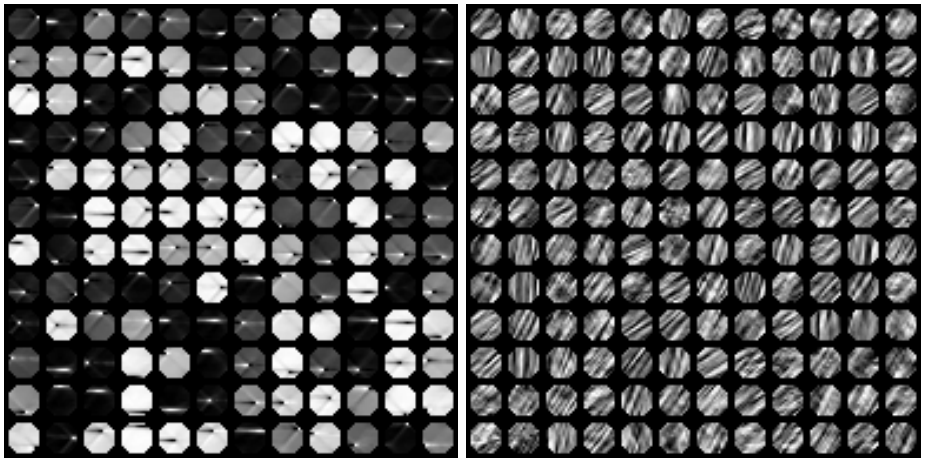

Figure 7.13: ICA bases generated by the Brodatz textures D34 (left) and D93.

Table 7.2: Classification accuracies for the Brodatz textures.

D17	D21	D34	D38	D77	D93	Overall
89.6 %	99.8 %	96.4 %	89.7 %	98.7 %	70.1 %	90.7 %

to D38, but they are also visually close to each other, both in intensity and their texture pattern.

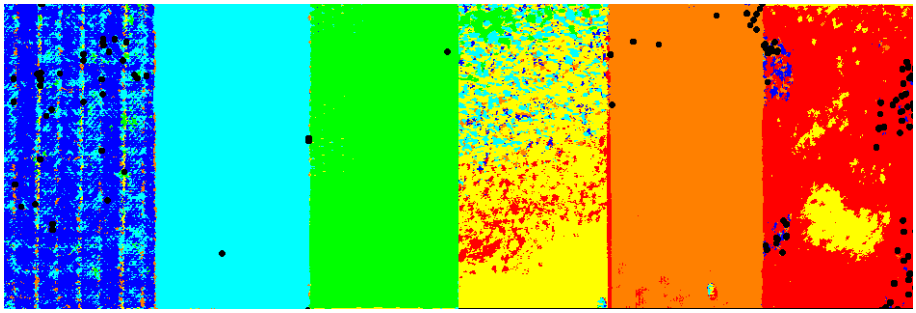

Figure 7.14: Classification of the textures in Fig. 7.12 with the intensity factor $\alpha_I = 0.2$.

7.8 Segment-Wise ICA-Based Sea Ice SAR Classification

Because the Baltic Sea ice varies very much, it is difficult to define pixel-wise sea ice classes accurately, and thus we can not use class-wise bases, i.e. generate sets of basis vectors corresponding to each predefined sea ice class. That kind of an approach is very easy e.g. for Brodatz textures and gives good classification results as was seen in the previous section. However, we can first segment SAR images and compute some ICA-based statistics giving information about the texture of each segment. We can perform a clustering of the ICA statistics computed for a training set, and produce a set of classes this way. Then we can use these classes to classify SAR segments by texture.

7.8.1 Training

In the training phase the ICA basis vectors representing areas of interest, which we here call featured areas in the images, are selected. Then the ICA basis vectors are automatically grouped to present different local feature classes. For each featured pixel of a segment in a segmented SAR image we compute the distribution of the ICA-based local feature classifications. This distribution is then used to classify the texture within the segment. The training procedure consists of the following steps:

1. Perform incidence angle normalization for the SAR image.
2. Find featured areas in the image i.e. areas containing edge-like or spot-like features, e.g. non-Gaussian data with reasonable variance, detected by the algorithms represented in Section 7.3, or pixels detected by an edge detection algorithm.
3. Create ICA bases using the windows located in the areas found in the previous step. Bases can be computed in multiple resolutions.

4. If multiple bases were computed, combine the bases into one set.

5. Prune duplicates that are very similar to some other vector(s) and also prune some small features located at the edge of the 2-D window corresponding to a basis vector. The matching is done by cross-correlation, first locating the center of mass for thresholded gradient window of each window. The cross-correlation between two vectors is computed by rotating another of the vectors in increments of α_1 (a parameter) and using the largest cross-correlation of these as the cross-correlation value.

6. Select basis vectors from the combined set that best fit a large number of samples drawn from the training data. The criterion is based on the sum of the absolute ICA coefficient values cumulated to each basis vector. In the coefficient cumulation only those values exceeding a threshold T are taken into account. Also here each basis vector is rotated in increments of α_2 and the largest ICA coefficient for each vector is used. The basis vectors that have sum larger than a given percentage of the largest sum are selected.

7. Cluster the basis vectors based on a large number of features. We just use a k-means type algorithm [145] for that, with $k \approx 10$.

8. Expand the basis by rotating each basis vector in increments of α_3.

9. Classify each featured pixel location. The class is defined by the cluster of the best matching basis vector, or if the cross correlation is less than a threshold, the class is set to an "undefined" class, i.e. there are $k+1$ classes.

10. Segment the SAR image. We use the PCNN-based segmentation presented in Section 6.3.

11. For each SAR segment attach the distribution of the featured pixel classes computed in the previous stage. The pixels at the segment edges are not used in the computation as segment edges may contain similar features which exist inside segments and can thus have effect on the classification. The distributions are normalized to sum to one, and the number of featured pixels in each segment is used as a separate feature in the classification.

12. The segment-wise normalized distributions and counts of featured pixels per unit area, i.e. segment-wise numbers of featured pixels divided by the segment areas. The counts of featured pixels per unit area and the normalized distributions are then clustered, e.g. using the ISODATA algorithm, producing two sets of cluster centers. We call these features *roughness* and *texture*. This is performed for the segments of the whole training material, i.e. several images.

7.8.2 Classification

The classification uses the count of featured pixels per unit area and the local feature distribution to classify the segments. Each segment is simply classified to correspond to the class of the nearest cluster center created in the training phase. The classification procedure consists of the following steps:

1. Perform incidence angle normalization for the SAR image.
2. Find the featured areas (as in training) for the image.
3. Classify each featured pixel location using the basis vector classes computed in the training.
4. Segment the SAR image, as in the training phase.
5. For each SAR segment attach a distribution of the featured pixel classes.
6. Classify each segment such that the class corresponds to the shortest Euclidean distance between the segment features and the cluster centers. We get two classifications, one simply based on the number of featured segments in the segment divided by the segment size, and the other based on the normalized distribution of the features.

7.8.3 A Practical Example

We used a large set (27 scenes) of Radarsat-1 ScanSAR wide mode data for the ICA training. As a result we got a set of vectors mapped into $k = 6$ categories shown in Fig. 7.15. The vector length is 145, corresponding to a round-shaped image window with a diameter of 13 pixels.

We here use the SAR scene of Fig. 4.6 in Section 4.3 as an example. The segmentation of this image, based on the PCNN-segmentation is shown in Fig. 7.16. The classification was applied to the same SAR image window (containing many edge-like and spot-like features), which has also been used as an example earlier. The featured areas were here located using the Canny edge detection algorithm (see Fig. 7.17) and filtering out very small edge segments, assuming they are due to speckle. The result of the roughness and texture classifications are shown in Fig. 7.18, and the final combined classification in Fig. 7.19.

The texture classification can better distinguish the deformed areas, based on the type of deformation, making difference between smaller features and longer edge-like features. In general, by visual comparison of the ICA-based classification results and ice charts, it can be seen that the textures of fast ice and new ice are rather similar. Also, the texture of consolidated close ice pack and compact or very close ice pack are similar to each other, but different from the previous two. In addition, the texture of level ice differs from these two main classes. The texture of open ice and open sea depends on the amount of ice floes among the open sea and on wind conditions (waves).

The roughness value is lowest for level ice, higher for close ice and even higher for consolidated, compact or very close ice. By combining the texture and roughness classifications we get a classification describing the ice surface inside segments as seen by the C-band SAR instrument. This description is usually in finer resolution than the symbols and segments drawn on the ice chart, making the verification difficult, especially for small segments.

We have also ordered the set of basis vectors by their orientation. The edge-like filters were selected by first generating a gradient image of the ICA filters, then

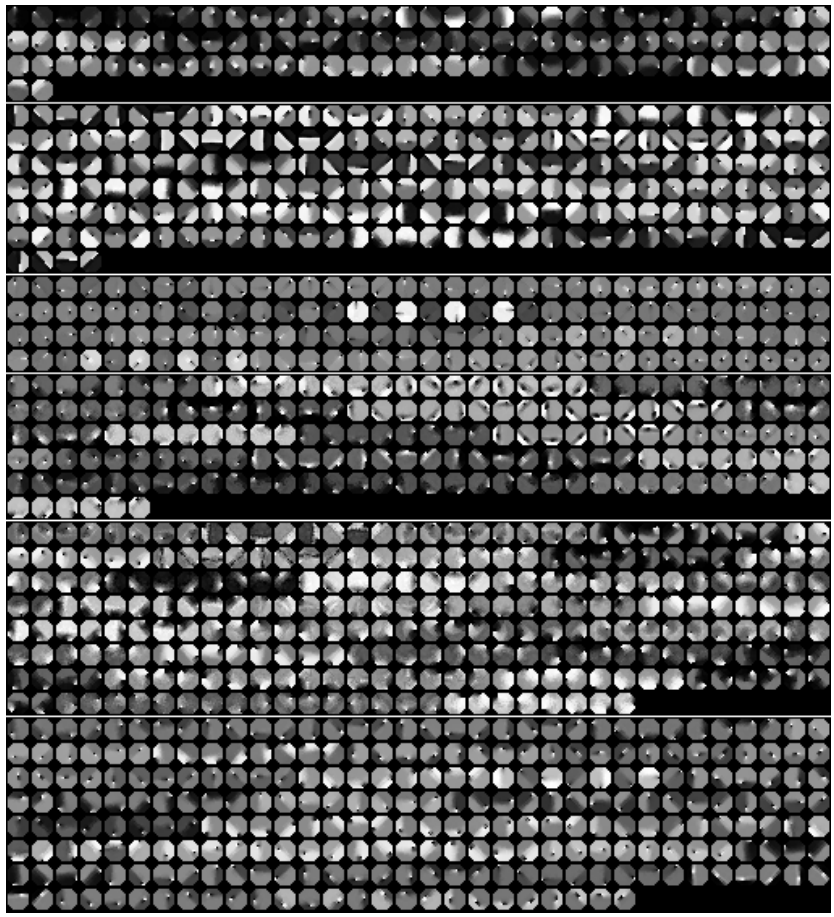

Figure 7.15: Extended set of ICA vectors, ordered in 6 classes. The class number increases from top (class 1) to bottom (class 6), the classes are separated by horizontal lines.

thresholding this gradient image and generating binary images to locate edges in the filters. The two principal components λ_1 and λ_2 of the binary edge images were ordered such that $|\lambda_1| > |\lambda_2|$ for the filter edges were computed. If the value $e = \sqrt{|\lambda_1|/|\lambda_2|}$ exceeded a given threshold T, that window was decided to be an edge filter. The direction for each selected filter was defined based on the direction of the first eigenvector.

A set of ICA vectors automatically ordered according to their direction is shown in Fig. 7.20. This set was used in defining local edge direction distributions for SAR data. Such distributions can be useful in navigation in the Baltic Sea ice. This has been tested to generate ridge direction distributions over high-resolution Envisat ASAR images to aid navigation, but it has not been in operational use.

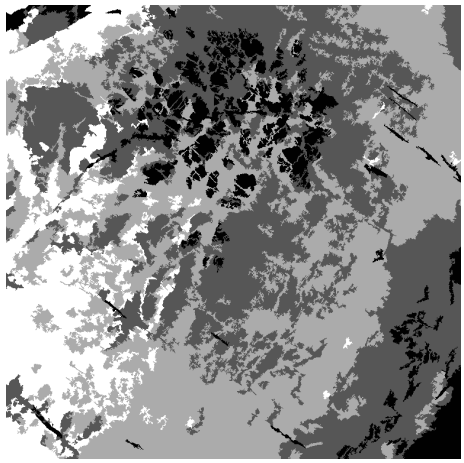

Figure 7.16: Segmentation result for the SAR image of Fig. 4.6, based on PCNN and segments smaller than a threshold (100 pixels) joined to the neighboring segments.

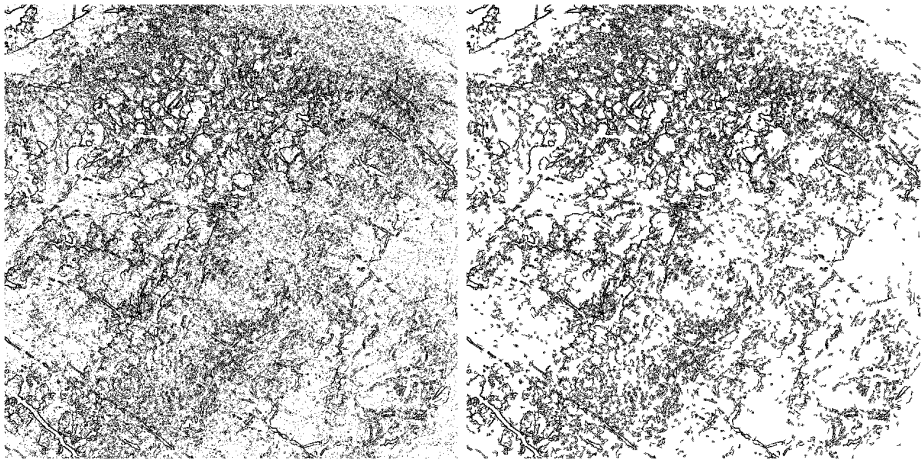

Figure 7.17: Edge detection (Canny [21]) applied to the SAR image in Fig. 4.6, left. Edge image with small edge segments (less than 10 adjacent pixels) filtered out, right.

7.9 Discussion

It seems that the proposed ICA-based classification method can distinguish between some elementary types of sea ice. By combining this method with segment mean intensity classification and local autocorrelation classification, we can get an improved classification scheme compared to our earlier classifier [108]. It is also obvious that the texture, i.e. the classification based on the relative distribution of the feature types inside a segment, gives extra information compared to the

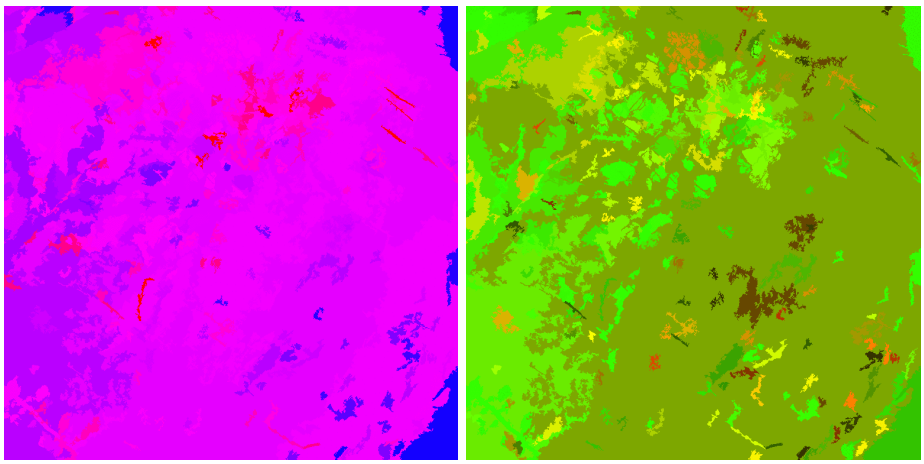

Figure 7.18: Roughness classification of the segments. Blue represents low and red high roughness (left). Texture classification of the segments (right). The light green areas mostly represent new ice (no fast ice present), the green areas level ice, and the colors from dark green to red more deformed ice types with leads or ridges.

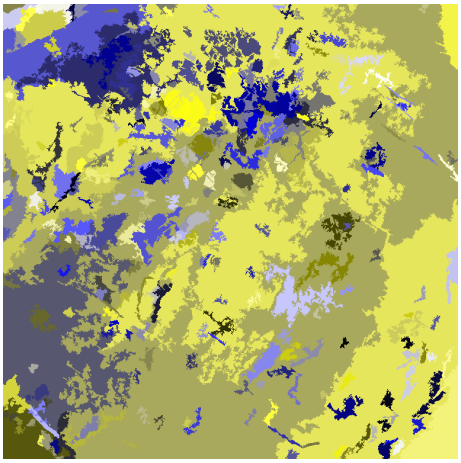

Figure 7.19: Combined roughness and texture classification of the segments.

roughness feature only. However, the exact geophysical interpretation of the texture information is very difficult and combining it with the ice types currently in use in our operational classifier [108] or with the ice types described in Section 2.4 seems to be very difficult.

The training of the ICA with Radarsat-1 ScanSAR data requires selection of the input data, e.g. based on the location of the edges. However, the training results were better for the ERS SAR-data which has better contrast (i.e. higher signal

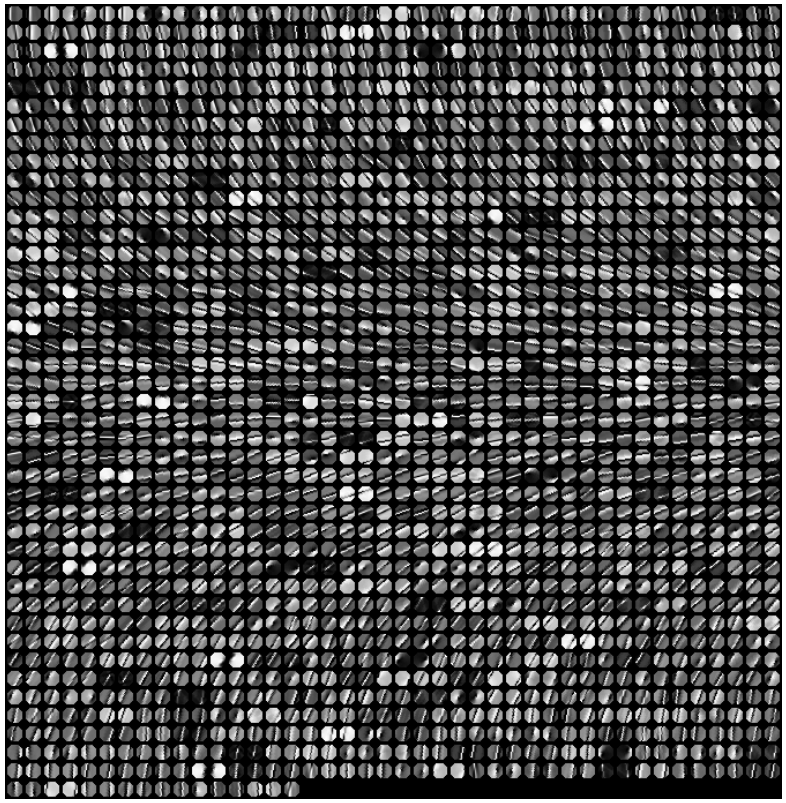

Figure 7.20: Selected edge-like ICA basis vectors ordered by their computed direction.

to noise ratio) compared to our Radarsat-1 data. We also tested training ICA with filtered Radarsat-1 data, but most of the tested filtering techniques seem to emphasize the spot-like features making most of the ICA basis vectors to describe these spot-like features. Also the use of the noisy ICA [97] was tested for Radarsat-1 data, but the results were not very promising. Possibly a combination of careful automated selection of the training data set and noisy ICA could improve the training.

The edge and spot-like feature detection based on higher-order statistics works for our noisy data rather well, but the accuracy is dependent on the selection of the window size and possible pre-filtering. The speckle has stronger effect for small windows and weaker for large windows (or for pre-filtered images), while large window size and pre-filtering reduce the local accuracy. We have used window sizes of 7–11 pixels in diameter and in some cases also applied anisotropic diffusion-based pre-filtering. These settings give reasonable results for our data, based on visual judgment. In the future we are going to study adding of a corner pixel detector into the pixel classification and then detecting three classes of pixels, i.e. edges, spot-like and corner pixels.

Chapter 8

Estimation of Ice Thickness Based on Baltic Sea Ice SAR Data and Thickness History

Ice thickness is one of the most important parameters for the navigation in sea ice, and the ice charts produced by FIS include ice thickness values for each chart area (segment). However, the manually drawn segments are typically large and spatially more accurate information about the sea ice thickness would aid the navigation. Additionally the information in digitized ice charts is based on visual interpretation of remote sensing data and on sparse ice thickness measurements and approximations coming from coastal stations and ships. In this work an algorithm which refines the ice thickness information available in the latest available digitized ice chart based on our operational Radarsat-1 SAR data has been developed. The ice charts are drawn daily by FIS personnel on duty. For each area in the ice chart an ice thickness interval and mean ice thickness value are given. An example of an ice chart in vector graphics is shown in Fig. 8.1, however, the digitized ice charts we use are converted into raster graphics.

8.1 Preprocessing

One operational product delivered to the end-users are the SAR-refined ice thickness charts. In this product the most recent available digitized ice chart, derived from the daily ice chart made at FIS, is refined based on a newly arrived SAR image. The steps of the operational algorithm are described here.

First, our incidence angle normalization algorithm developed for Baltic Sea ice [154] is applied to the SAR data. Then the incidence angle corrected images are segmented using a slightly modified ISODATA clustering algorithm [6]. The ISODATA algorithm is a variant of the k-means algorithm [145]. Instead of a predefined number of cluster of the k-means algorithm, ISODATA algorithm produces a

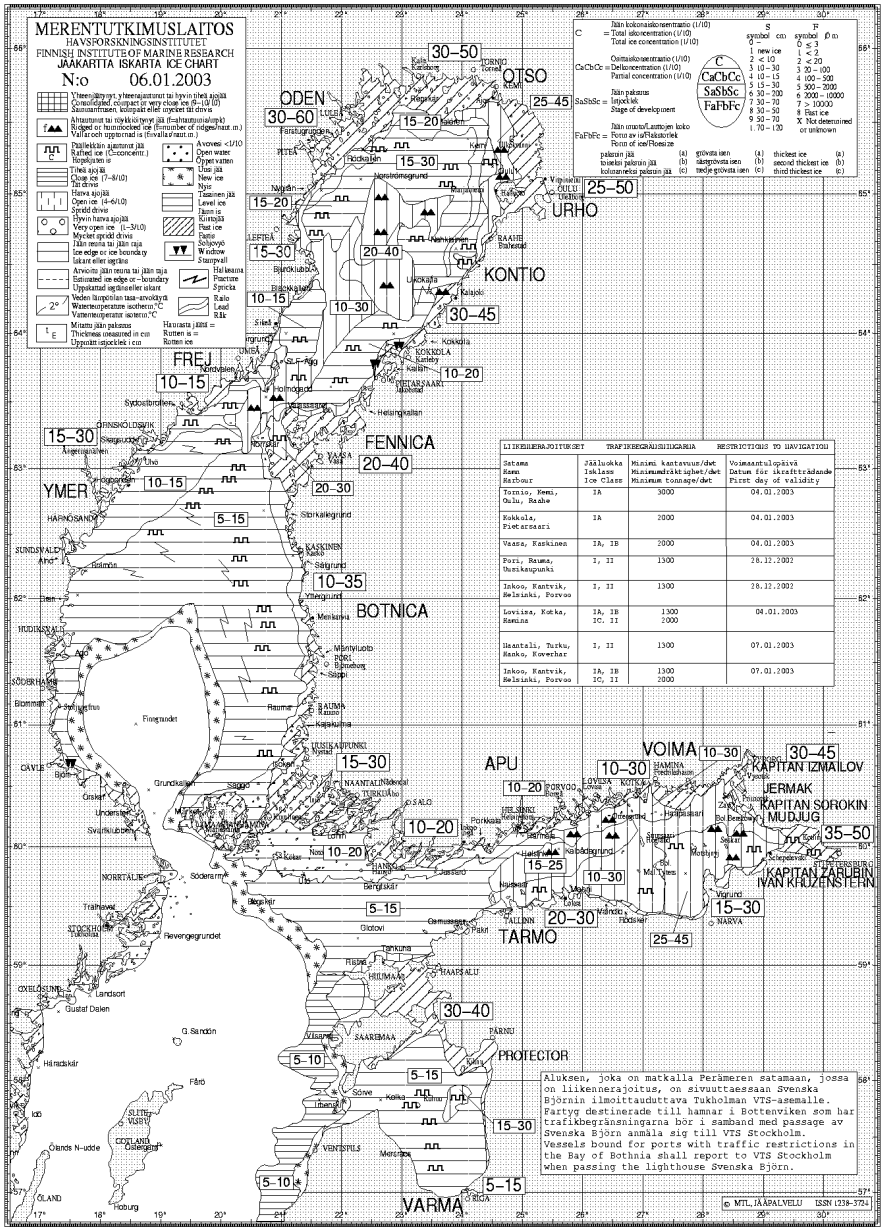

Figure 8.1: Ice chart (©Finnish Ice Service) of January 6th 2003.

data-dependent number of clusters adjusted by some input parameters (minimum distance between cluster, maximum variance inside a cluster, minimum number of samples in a cluster). In the ISODATA algorithm the clusters are merged and split according to these criteria during the iteration. In our ISODATA algorithm the

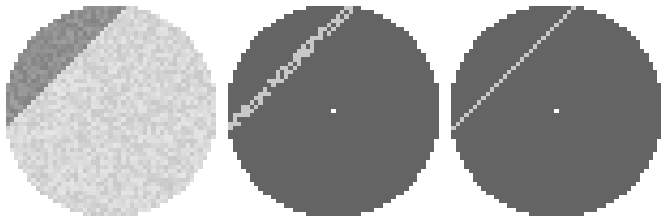

Figure 8.2: An example of a round-shaped image window with an edge (left), finding the edge pixels by gradient thresholding (middle) and showing the estimated edge direction and location (right). For visual purposes this window size is larger than the size used in the actual algorithm. Only the pixels lying on the same side of the detected gradient line as the mid-pixel (shown bright) are used in computing the mean value used in the segmentation.

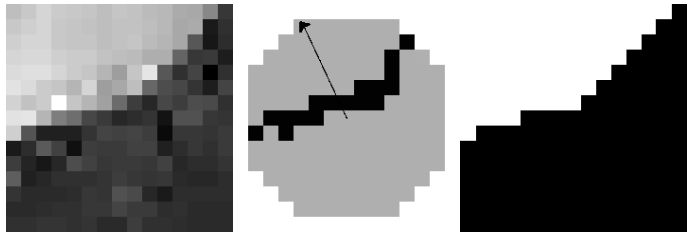

Figure 8.3: A small piece of a SAR image with a segment edge (left). The detected edge pixels in a 13×13 pixel window and gradient direction shown as an arrow (middle). Final segmentation result (right).

split and merge procedures slightly differ from those of the standard ISODATA algorithm. Our variant does the splitting by applying 2-means (k-means with k=2) inside the cluster to be split, and merging is done by merging each sample separately to the cluster corresponding to the closest cluster center.

The values used in the ISODATA segmentation are not the pixel values, but means computed in a round-shaped window with a diameter D around each pixel. For each such window the gradient inside the window is computed and thresholded with a threshold relative to the maximum and minimum gradients inside the window, $T = g_{\min} + \alpha(g_{\max} - g_{\min})$, where $0 < \alpha < 1$ is a coefficient. The locations of the gradient values exceeding T are considered as (linear) edge pixel locations. The connected edge contour is formed as follows. The direction of the edge is defined to be the first principal component of the edge pixel locations. The location of the edge is determined by assigning the principal component vector to the center of mass of the gradient pixel locations, see Figs. 8.2 and 8.3. Finally, the mean in the window is computed only including those pixels which are on the same side of the edge as the mid-pixel of the window, and if the mid-pixel happens to be at the edge, the mean is computed for the edge pixels only.

8.2 Combining Ice Thickness History and SAR Data

After segmentation each SAR segment is compared to the segments in the ice thickness map. If over 50 % of a SAR segment is covered by one chart thickness segment, this chart thickness segment is extended to cover the whole SAR segment, otherwise the chart thickness segment remains unchanged. This step defines anew the boundaries of the chart thickness segments. Naturally, one can also apply some other threshold than 50 % coverage currently in use. Smaller percentages change the digitized ice chart more and higher percentages less. After this updating of the ice thickness segment boundaries the thickness values are linearly mapped such that the minimum thickness is mapped to correspond to the minimum SAR segment intensity mean and the maximum thickness to correspond to the maximum SAR segment intensity mean inside the same thickness map segment. This procedure is applied to a thickness map and a SAR image of the same day, producing a map which we call an *augmented ice thickness map*. If we have at our disposal a new SAR image and the ice thickness map of the previous day, this procedure can be utilized to give an estimate for the current ice thickness distribution. The estimation works well if only minor changes in the ice conditions between the time of the SAR acquisition and the time of making the ice chart have occurred.

However, due to the dynamic nature of drift ice fields, the changes in ice conditions can be radical. Especially this is true if the time gap between the SAR data and ice history is larger than one day. For this purpose we have developed an algorithm which tries to correct the ice thickness map generated from the ice history with the aid of the SAR data. The empirical observations guiding the correction procedure are that the areas with low spatial autocorrelation are often open water areas and the areas with high intensity and higher autocorrelation have often higher mean ice thickness. By utilizing these observations, certain changes (e.g. identification of open water areas) to the existing segmentation can be made. To ensure that these changes mostly lead to corrections instead of misinterpretations, certain thresholds for autocorrelation and intensity statistics need to be defined. These thresholds were estimated from a training data set containing simultaneous SAR and ice thickness data. In the training phase 10 different intensity classes were determined. In the updating algorithm the image is then classified by utilizing these fixed class centers, shown in Table 8.1.

The features used in the classification are the local autocorrelation computed in an 11×11 pixel window around each pixel and the SAR segment intensity mean. The segments are further divided if the autocorrelation segments do not match with the intensity segmentation with a required accuracy. As a result, we have a segmentation with two values, intensity mean and autocorrelation, for each segment. These segments are then classified to four probable open sea classes and six ice classes. The thickness is changed to zero (open sea) if the class of the segment is one of the open sea classes and the thickness in the previous ice thickness map is less than a threshold. The remaining six ice classes have values for minimum thickness associated to each of them, and if the ice chart thickness value is less than this minimum value, it is set to a mode value in a neighborhood of the segment. This mode value is computed only for values greater or equal than the given class-wise minimum thickness. The mode computing neighborhood is defined as the area of

Table 8.1: Segment classification for ice thickness map correction. The SAR intensity and autocorrelation are used to correct segment thickness values for such segments that could probably be misclassified without any correction. The segment minimum thicknesses deviating from the values given here are changed to these values.

Object type	Class	Intensity	AC mean	Assigned min tck (cm)
Open water	1	63.4	< 0.29	0
	2	84.9	< 0.29	0
	3	99.6	< 0.29	0
	4	113.7	< 0.29	0
Ice	5	56.5	$0.29 \ldots 0.44$	1
	6	59.6	> 0.44	2
	7	69.9	$0.29 \ldots 0.44$	5
	8	83.0	$0.29 \ldots 0.44$	10
	9	79.9	> 0.44	15
	10	94.9	$0.29 \ldots 0.44$	5

the bounding box of the segment enlarged by a constant factor into directions of its four sides.

The segments are classified to the class corresponding to the nearest class centre using the 2-dimensional Euclidean distance. The autocorrelation is normalized to be in the interval $(0, 255)$ before the classification. These values shown in Table 8.1 were defined based on a small set of experimental data, and in practice they make cautious corrections to the right direction. To define more precise correction values an analysis of larger data set would be required. An example of some steps of the algorithm are shown in Figs. 8.4–8.6. The original SAR image, the segmentation result for the image and the resulting ice thickness chart are shown.

It is also possible to generate mosaics of several successive thickness images to cover larger areas of the Baltic Sea in the same image. This kind of a product is not operational, but could be made such depending on the interests of the end-users. The operational mosaics would always be updated after arrival of a new SAR image. An example of a SAR mosaic and SAR-refined thickness chart is shown in Figs. 8.7 and 8.8. These can be compared to the ice chart of January 6th 2003 shown in Fig. 8.1.

8.3 Comparisons between FIMR Ice Thickness Products and EM Measurements

The maximum daily temperatures during the HEM measurement campaign in the winter 2003 were typically above zero degrees, probably making the ice surface and snow on the ice wet in the daytime, and thus attenuating the SAR backscattering from the sea ice. This data set mainly describes the statistics of wet snow or frozen

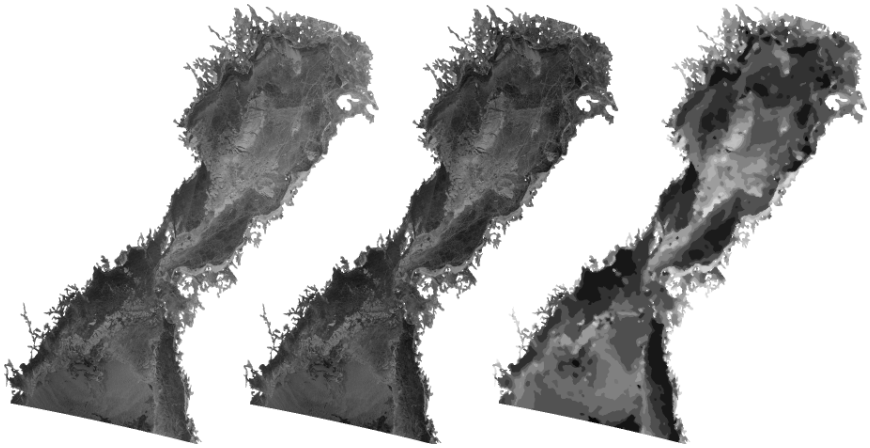

Figure 8.4: A Radarsat-1 ScanSAR wide mode image over the Bay of Bothnia, January 2nd 2003, ©Canadian Space Agency (left). The image after our incidence angle correction algorithm has been applied (middle). And a segmentation image (right), where the segments have been filled with the segment mean intensity value. This is a filtered version of the original SAR image. For visual purposes the mean values in the figure have been scaled between black and white.

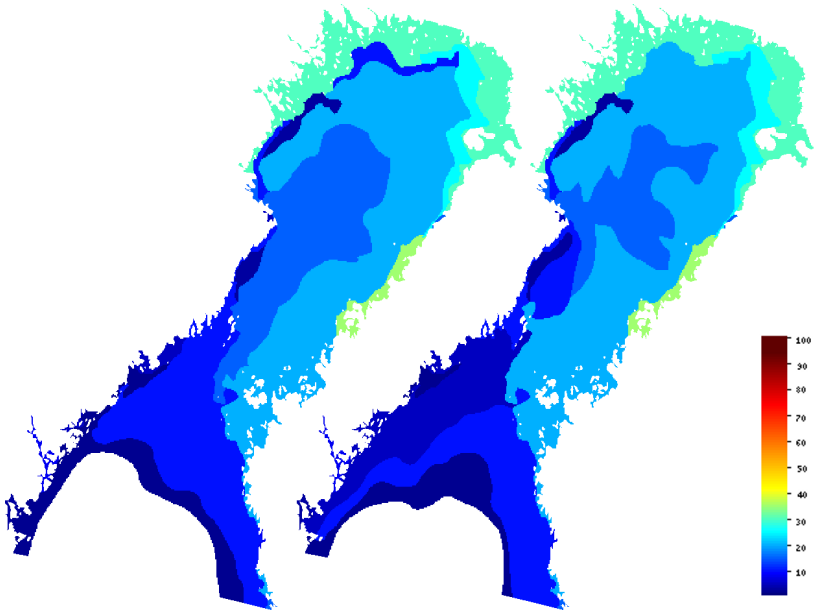

Figure 8.5: The ice thickness chart of January 1st 2003 (left) and January 2nd 2003 (right).

snow-surface conditions, and a similar study for dry snow conditions would also be useful. The time gap between the SAR image and the HEM measurement varied from about 2 hours to about 9.5 hours, and the wind speeds between the SAR

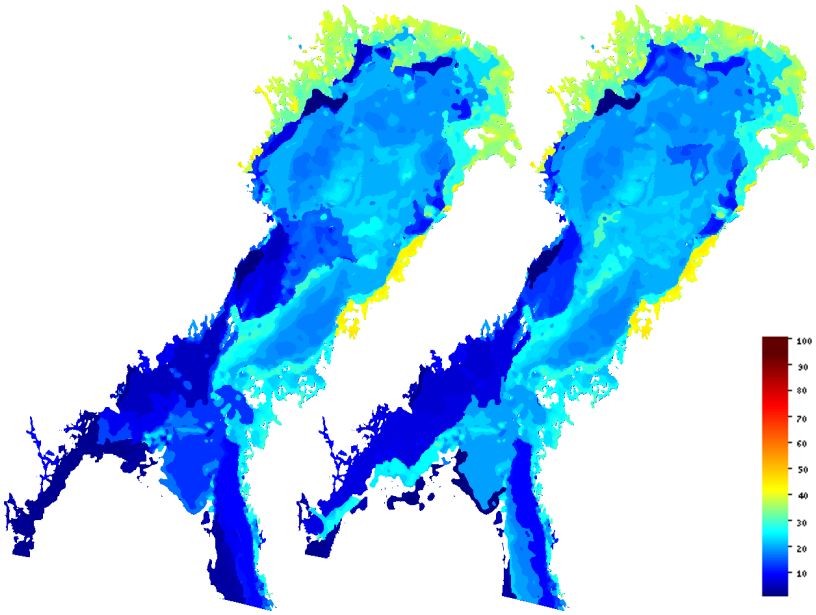

Figure 8.6: The SAR-refined ice thickness chart of January 2nd 2003 (left) based on the previous day ice thickness chart, with the correction procedure applied. The SAR-refined ice thickness chart (right) of January 2nd 2003 based on the same day ice thickness chart.

acquisition and the HEM measurement were relatively low (in maximum about 4 m/s in the coastal stations). The data are in different resolutions, the sampling rate of the HEM measurement is 3–4 m and the HEM measurement resolution is around 20–30 m, while the Radarsat-1 images are in 100 m resolution. The nominal resolution of digitized ice thickness charts is about 1 km, and the resolution of our operative SAR-refined ice thickness chart is 500 m. In 100 m resolution the HEM flight line in maximum covers about 20 % of the pixel area (assuming straight flight line over the pixel center), and in 500 m resolution this area is only 4 %. The only reasonable way to compare these kind of data is to make statistical comparisons. The material covers five SAR images from 4 days, and about 1000 km of HEM flight lines in total. The measurements were conducted in highly ridged drift ice area during February 17th and February 23rd 2003 in Gulf of Finland and Gulf of Bothnia. Before the comparisons the incidence angle correction [154] [publication 2] was applied to the SAR data, normalizing the SAR pixel values to correspond an incidence angle of 35 degrees.

For each SAR or product pixel in the HEM measurement lines, we first determined a distribution of the measured HEM thicknesses. From this histogram several statistics can be extracted, we computed e.g. the relative amounts of three ice classes, the mean thickness and the thickness mode over each 500 m pixel. To analyze our data, we coarsely divided the sea ice into three categories, the first representing level ice corresponding to the thermal growth, the second representing rafted ice, and the third representing ridged ice. Additionally there appear also

Figure 8.7: A SAR mosaic of three Radarsat-1 ScanSAR wide mode images, from Jan 6th 2003 (2 images) and Jan 7th 2003 (1). The image boundaries have been drawn in the image.

open water. The level ice, is ice with the HEM thickness less than 50 cm (representing the estimated maximal thermal growth until late February, being about 50–60 cm), rafted ice is the HEM thickness measurement range from 50 to 100 cm (corresponding to doubles of the level ice), and the ridged ice is the ice with HEM thickness over 100 cm (including higher multiples of the level ice).

In our statistical analysis, the most expressive statistical relationship between the incidence angle corrected SAR pixel values and the HEM thickness distribution was established as follows. The range of the amplitude values was first divided into 15 equal-sized bins. Then, given a fixed bin, we computed the conditional distribution of the three ice thickness categories based on the HEM thickness values. It was observed that the fraction of small ridges (rafted ice) remained relatively constant independent of the SAR pixel value. In this data set with these thickness limits, this fraction remained about the level of 30 %. On the other hand, the area covered by large ridges grows almost linearly from 0–10 % at very low amplitude values to 90–100 % at the highest amplitude values. The fraction of level ice decreased from 70 % at low amplitudes to less than 10 % at high amplitude values, see Fig. 8.9.

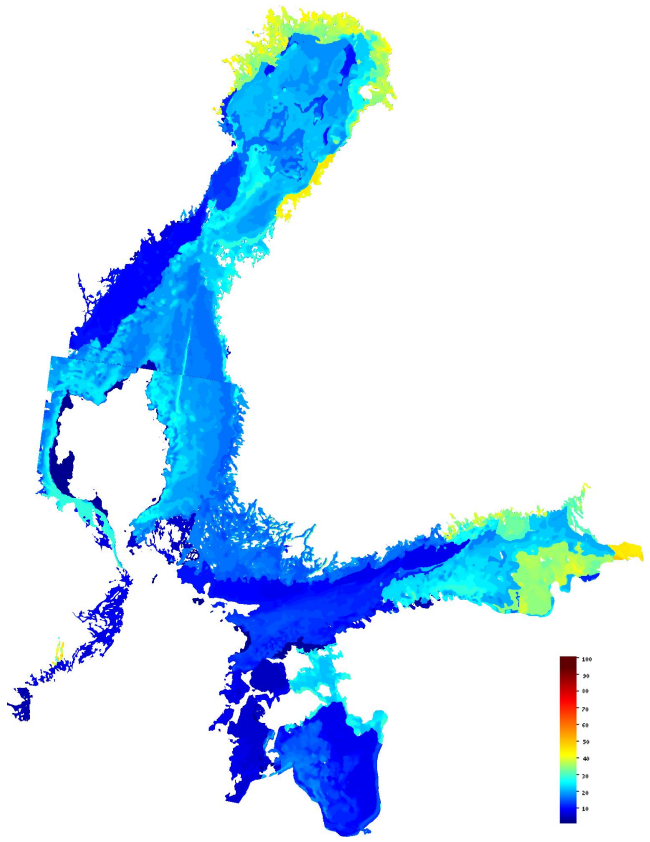

Figure 8.8: The refined thickness map mosaic corresponding to the mosaic of Fig. 8.7. Some minor differences on opposite sides of image boundaries can be seen. They can be due to improper image co-calibration at KSA or due to changes in ice conditions during the time gap between the images.

If the limits in the three ice categories are changed, the figures of relative fraction change accordingly, but qualitatively they exhibit the same kind behavior.

We also examined the (cross-)correlations between the incidence angle corrected SAR pixel values, ice thickness of the ice charts, the SAR enhanced ice thickness charts and values computed from the HEM measurements. The correlations are shown in Table 8.2. The trends seen in these correlations are consistent with the results presented in Fig. 4.6. The correlation between the SAR pixel value and the relative amount of level ice is negative, for rafted ice the correlation is practically zero and for ridged ice positive. Also it can be seen that the correlations between the HEM measurement values describing the thickness (mean, mode) and the refined thickness chart are slightly higher than the corresponding values for the refined ice chart.

The digitized ice chart has three thickness values for each segment, i.e. the level ice minimum, mean and maximum thicknesses. In our data along the flight lines,

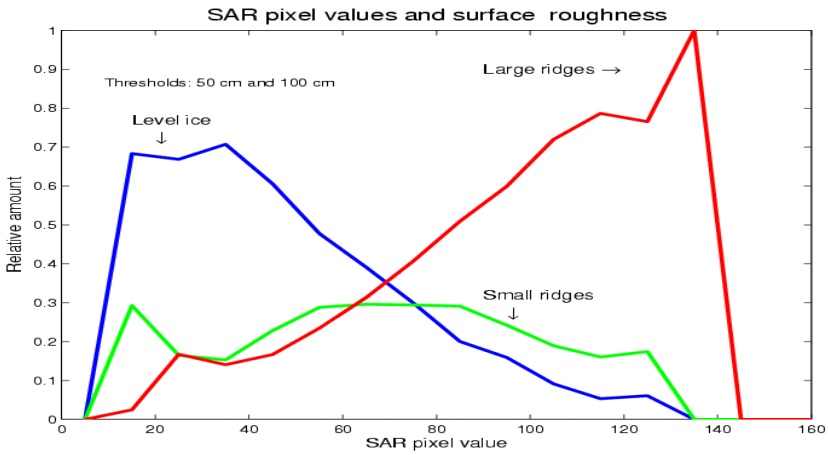

Figure 8.9: The relative amounts of the three ice types as a function of incidence angle corrected SAR intensity. The tails of the curves have been set to zero because at those pixel values levels the number of samples was too small for making reliable statistical conclusions.

Table 8.2: Correlations between the products and pixel-wise values derived from the HEM measurements. The pixel resolution is 500 m.

Variable	SAR	Thickn.	Refined thickn.
level	-0.32	-0.18	-0.21
rafted	0.02	0.16	0.12
ridged	0.30	0.07	0.12
mean	0.25	0.11	0.14
mode	0.16	0.14	ă 0.20

we could find the following different classes described by the triplet thickness minimum-mean-maximum: 5-5-5, 5-5-10, 5-15-30, 10-15-30, 10-20-30, 20-25-40, 20-30-50, 20-35-50, 10-40-50, 30-40-60, 30-45-60 and 40-50-70.

The accuracy of the estimates given by different ice thickness charts is assessed as follows. First, the digitized ice charts are divided into classes based on the triplets described above. The SAR refined ice charts are divided into 30 bins with a fixed bin width of 2 cm. Second, the class-wise ice chart distributions for open water and the three ice types are calculated for each bin. In the ideal case, the amount of deformed ice types increases with the estimated level ice thickness. For the digitized ice charts this seems not to be the case. There occurs random-like fluctuation in the fraction of highly ridged ice areas up to the estimated mean level of about 35 cm. Above that the amount of highly deformed ice area remains high and, approximately, at the same level, i.e., the higher bins are not significantly different from each other, see Fig. 8.10 upper panel.

For the SAR refined thickness chart the results are more satisfactory. Excluding the thin ice case (estimated thickness less than 4 cm), the amount of deformed ice types increases as a function of the level ice thickness estimate until about

35 cm. Then a state is reached, where the fraction of deformed ice type remains approximately at the same level independent of the thickness estimate. This is illustrated in Fig. 8.10 lower panel. This is explicable because the initial data has this same deficiency and in the forming of the SAR refined thickness chart some very restrictive rules are applied [publication 5]. These rules are necessary because one can not make any confident statement about the degree of ice deformation on the basis of single pixel value. As a result, correlations based on pixel-wise computations are very low, see Table 8.2.

In the areas estimated by the SAR-refined ice chart to represent very thin ice, 1 to 4 cm, there occurred also relatively high fractions of deformed ice. To find out the explanation for this peculiar behavior, we checked the location of measurements where the SAR-refined ice chart thickness is less than 10 cm and more than half of the HEM thickness measurements inside the pixel have thickness values more than 50 cm. We found that these measurements typically were made at the edges of thin ice or leads (open water areas), according to the SAR-refined ice chart. In addition these erroneous pixels typically appear in relatively short segments. Such errors can be reasoned to be (1) due to the time gaps between the SAR images and HEM measurements, and (2) sea ice movement and reformation during the time gaps. Probably a larger number of HEM measurements over areas with thin ice and even larger open water areas, not just narrow leads, would have yielded more representative statistics for the areas interpreted as thin ice according to the SAR-refined ice charts.

We have also studied the mean ice thickness and ice concentration as a function of the incidence angle corrected SAR pixel value. These comparisons were also made for the winter 2003 Radarsat-1 ScanSAR wide mode data and the HEM measurements. According to these statistical comparisons the mean ice thickness increases as the SAR pixel value increases (see Fig. 8.11, left panel) and is saturated at the high SAR pixel values. The ice concentration, computed from the HEM measurements as complement of the relative amount of ice thickness values less than 1 cm, clearly increases as a function of the SAR intensity (see Fig. 8.11, right panel), and finally saturates at SAR pixel intensity of about 120.

If we study the standard deviation of the laser altimeter measurements of the HEM instrument, over a short period, we can see clear positive correlation with the HEM thickness measurement. We can interpret the short time changes in the altitude from the sea ice surface to be mainly due to the sea ice surface roughness, and this indicates positive correlation between the sea ice surface roughness and sea ice thickness in the Baltic Sea. This correlation is at highest for small number of measurements and decreases as the number of included samples is increased (see Fig. 8.12, left panel). The dependence of surface roughness on SAR pixel value is shown in Fig. 8.12, right panel. It can be seen that the surface roughness is clearly increasing at the low SAR intensity values, then very slowly increasing in the midrange and at the high SAR intensity values the surface roughness is also very high.

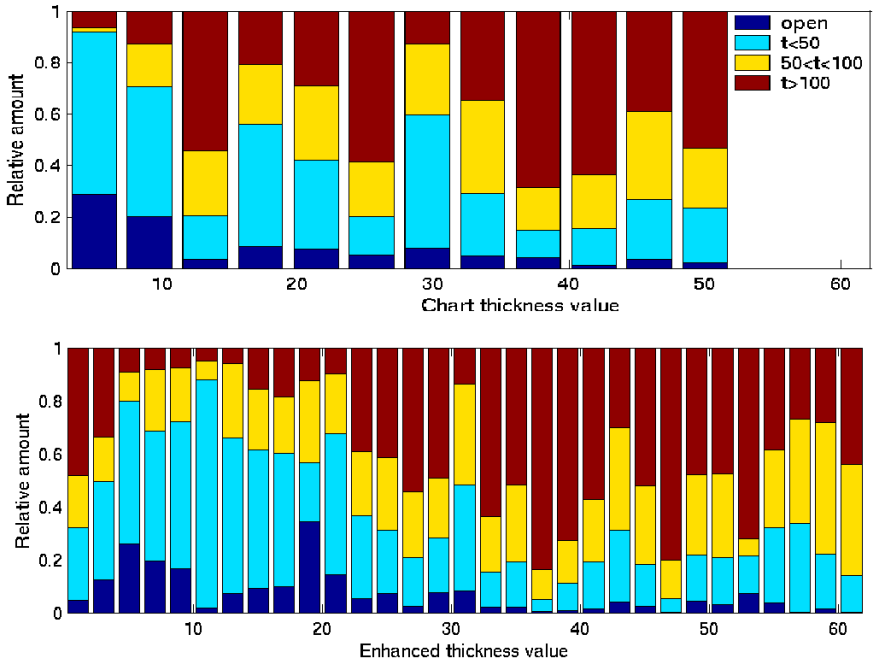

Figure 8.10: The relative amounts of the three ice types and open water for the ice types present in the ice chart (upper figure), and for the SAR-refined ice chart (lower figure).

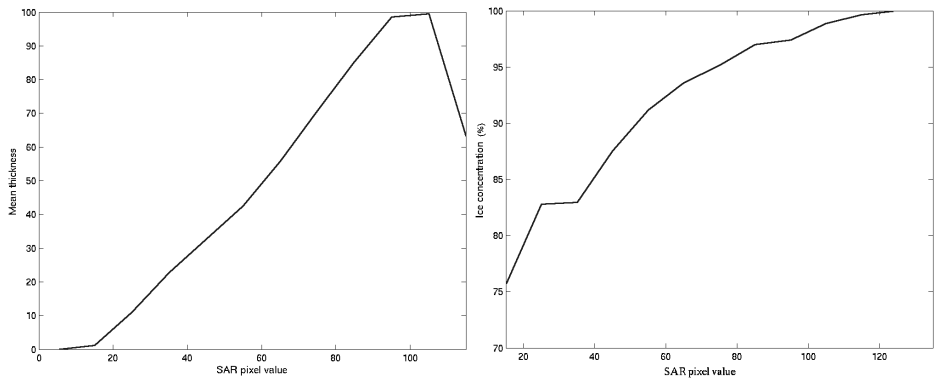

Figure 8.11: Ice thickness as a function of the SAR pixel value computed for the Radarsat-1 data with incidence angle correction applied (left) and HEM measurements for the winter 2003 data set. The drop in the high SAR pixel value range is probably due to the very few samples available at the high pixel value range and the effect of speckle. Ice concentration (%, right) derived from the HEM measurements as a function of SAR intensity.

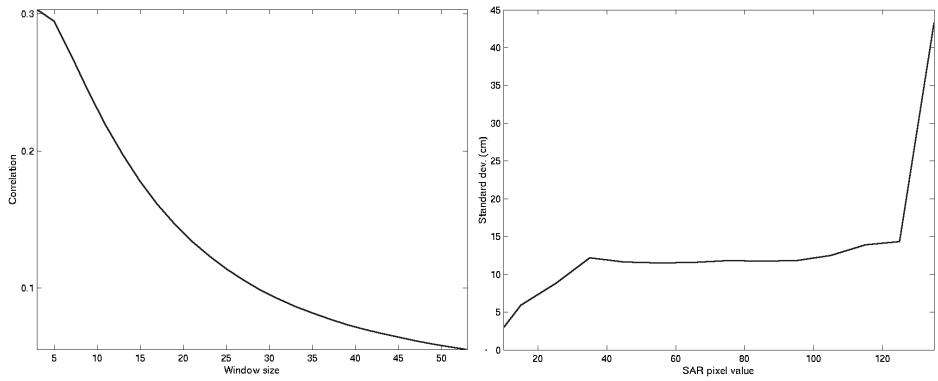

Figure 8.12: Correlation between the HEM thickness measurements and altitude standard deviation, measured by the HEM instrument laser altimeter, as a function of the sample window length, left. Surface roughness (laser altimeter standard deviation over one SAR pixel) as a function of the SAR intensity, right.

Chapter 9

Summary and Conclusions

The aim of this work has been to improve the operational SAR ice products for winter navigation purposes in the Baltic Sea. The main objective has been to produce sea ice information in compact and informative form to the end-users, and to produce and deliver this information automatically after a SAR image has been received at FIS. As a result, an improved, both in resolution and accuracy, sea ice classification scheme has been developed, and a new sea ice product, the SAR-refined ice thickness chart has been created and made operational. We have received positive feedback about the data products from the end-users on ships. Our operational ice typing algorithm has been updated based on these results, and the SAR-refined ice thickness chart is also currently in operational use. The main results of the work are:

- The operational sea ice SAR classification system, developed at FIMR by the author with colleagues, has been updated using the methods developed and tested in this work. These methods include the incidence angle normalization, improved segmentation, computation of new segment-wise features and improved open sea classification.

- A new sea ice product, the SAR-refined ice thickness chart, has been developed. This product is delivered operationally to FMI and Finnish and Swedish ice breakers, and is also available via Internet (at polarview.fimr.fi).

- For SAR image preprocessing an iterative incidence angle correction algorithm, based on statistical comparisons made at HUT/LST, has been developed. This is a necessary step before classifying typical operational SAR scenes with a relatively large incidence angle range. This algorithm performs an iterative normalization and classification into two sea ice classes, level ice and deformed ice. This is because the backscattering properties for these two classes as a function of the incidence angle are slightly different from each other [154]. We have also compared several speckle filtering algorithms and found the anisotropic diffusion based filtering suitable for our operational SAR data.

- Compression of SAR data has been developed significantly from the earlier and has been integrated in the user-program run on board the vessels, making delivery of higher-resolution SAR data to the end-users possible.

- Pulse-Coupled Neural Network (PCNN) based segmentation algorithm has been developed as a part of the work and it gives reasonable segmentations in applicable execution time for our data. Its performance for our Radarsat-1 data is comparable or better than some other segmentation methods typically used and compared in this work.

  One advantage is that the PCNN-based segmentation also gives a preliminary intensity-based classification based on the training data. The data-driven approach was necessary because we do not have absolute calibration of the data and can not directly compare the pixel values to calibrated measurements or values produced by a model. We can only indirectly reason the possible interpretation for the classes yielded by the data-driven training, based on relative comparisons, i.e. the order of the sea ice class means.

  After a segmentation it is possible to compute segment-wise features rather than use either pixel-wise features or features computed in a fixed-size window. Segmentation makes possible to use several statistical segment-wise features, including features based on segment shape, in classification.

- Distinguishing open water and sea ice from each other has been developed from the earlier pixel-wise method to a segment-wise classification. According to our tests this improves the open sea classification performance compared to the earlier, pixel-based algorithm in use at FIMR and FIS.

- Higher-order statistical methods have been developed and tested for sea ice SAR classification. The Independent Component Analysis (ICA) based texture classification gives extra information about the SAR texture compared to the standard SAR texture statistics (mean, variance) approach or the roughness statistics (relative number of edges in a segment). In the ICA-based classification some typical features present in the image are computed from a training data set and then automatically classified into a few feature classes. For each segment the relative amounts of these feature classes in the segment are used as classification information, in addition to the segment mean intensity and roughness. The geophysical interpretation and combining it to certain sea ice classes seems, however, to be a difficult task and still requires further research. The ICA method presented is a novel method in SAR texture classification.

- The evaluation and validation of SAR-based sea ice products has been developed. The evaluation of the classification products is very difficult because of the large area and dynamic nature of the Baltic Sea ice. Typically the classification results are only compared either to very few point-wise field measurements or visual interpretation of the SAR data. We use digitized ice charts from FIS and electromagnetic induction based ice thickness measurements by the HEM instrument to evaluate and validate our algorithms. Digitized ice charts are drawn by FIS sea ice experts based on many data sources, including field observation and multiple remote sensing data sets. This kind of an evaluation scheme covers large areas and makes statistical comparison of the data sets feasible. The comparisons between SAR

backscattering and the HEM instrument were the first in the area of the Baltic Sea.

Still a lot more data would be required for more detailed algorithm evaluation and validation. However, it can be said that the evaluation and validation has been significantly improved by the digitized ice charts and especially by the HEM measurements, which will be an important part of the future field campaigns. One problem in comparing our Radarsat-1 data to scatterometer measurements and backscattering models for Baltic Sea ice has been that most of our data is uncalibrated and we can only make relative comparisons of the sea ice classes. Another practical problem has been that the resolutions of the SAR image and validation data are typically quite different from each other.

An example of a SAR image and the FIMR sea ice products can be seen in Figs. 9.1 and 9.2. The SAR image is from the first of May 2006, i.e. from the melting period. For comparison also an optical RGB image captured by a passive spaceborne instrument operating at optical and infrared frequencies is shown in Fig. 9.1. This image was generated from data of the NASA's MODIS instrument (Moderate Resolution Imaging Spectroradiometer). The MODIS RGB image is generated from three MODIS bands (1: 620-670nm, 4: 545-565nm, 3: 459-479nm). Typically open sea and ice can be distinguished based on MODIS data, especially because there are also infrared channels available and surface temperatures can be estimated based on MODIS data. Also new ice can typically be distinguished in MODIS images. The major problems with MODIS data in sea ice monitoring are clouds, darkness and snow. In cloudy weather MODIS can not see the ice surface, and if the sky is partially cloudy, a cloud mask algorithm is required to locate the regions where the data can be used. Because MODIS is a passive instrument, only the infrared bands are useful during the dark hours, and the days in wintertime are quite short in the area of the Baltic Sea. MODIS is capable to measure the snow surface only and thus can not see the ice surface structure under the snow cover. In Fig. 9.2 are shown the segmentation result (segment means computed for the segments) using the PCNN algorithm, open sea classification, SAR-based ice thickness chart, and ,for comparison, the result of the old operational classification algorithm [108]. It can be seen that the old operational algorithm overestimates the open water areas. This is because of the wet snow cover and the wet ice surface smoothing and attenuating the backscattering and the pixel-wise autocorrelation thresholding used in the old algorithm.

The techniques and methods described in this work make possible to deliver more detailed SAR-based sea ice classification maps over the Baltic Sea and in higher spatial resolution. On a modern personal computer even the full SAR resolution of 100 m can be used in the products. Currently the classification procedure (incidence angle correction, segmentation, texture classification, open water and fast ice detection) takes a few hours for one SAR scene. With e.g. 200 m resolution the amount of computations and execution time are reduced roughly to a quarter and the time needed is then less than an hour for one SAR scene, which is a reasonable delivery time for these products. The different parts of the algorithm work as independent modules exchanging data in a predefined way, thus making module updating and replacement easy.

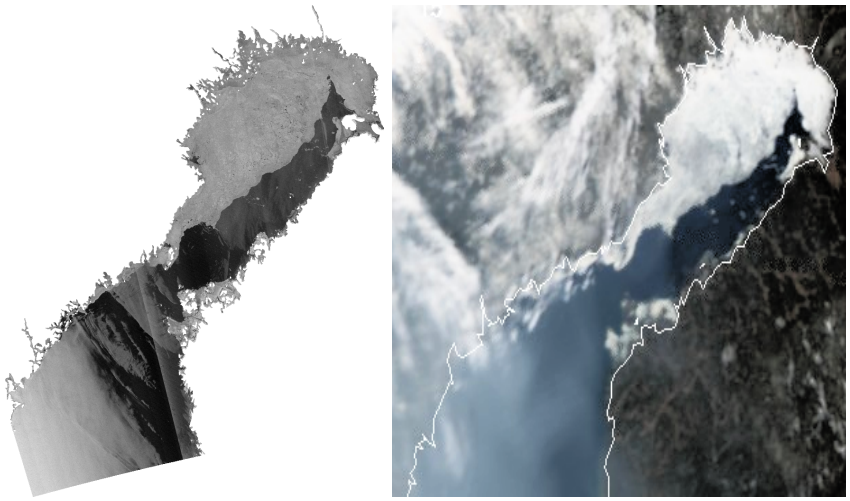

Figure 9.1: A SAR image, May 1st 2006 (left), and a MODIS RGB image from the same day (right).

The classification methods developed here are mainly for dry snow conditions. For wet snow conditions different parameters would typically be required. Also, fewer sea ice classes can be distinguished during wet snow conditions because the wet snow cover attenuates backscattering from the underlying sea ice strongly. In the future we are going to update the algorithms so that the snow condition is recognized based on the temperature history of a few recent days, and different parameters for dry and wet snow conditions will be applied accordingly.

In the future, space-borne SAR instruments will be improved and also dual-polarized and fully-polarized data suitable for operational use will be available. This will improve the sea ice classification significantly, but also the algorithms will require updating to fully utilize the polarimetric data. Also more geophysical information (temperature, wind etc.) will be included in the future classification schemes. In addition, the classification will be compared to the operational ice (forecasting) models at FIMR and efforts to assimilate the SAR classification with ice models will be made. In the near future we are also expecting to have absolutely calibrated Radarsat-1 and Radarsat-2 SAR data from KSAT. Then we can better compare the algorithm results to scatterometer measurements and backscattering model outputs. Also some simultaneous HEM and SAR data over polar areas will be collected and the suitability of our algorithms for these areas with multi-year ice will be studied. The algorithm parameters will be adjusted better suitable for polar area data. Depending on the results with the existing algorithms, algorithms better suitable for polar areas will possibly be developed.

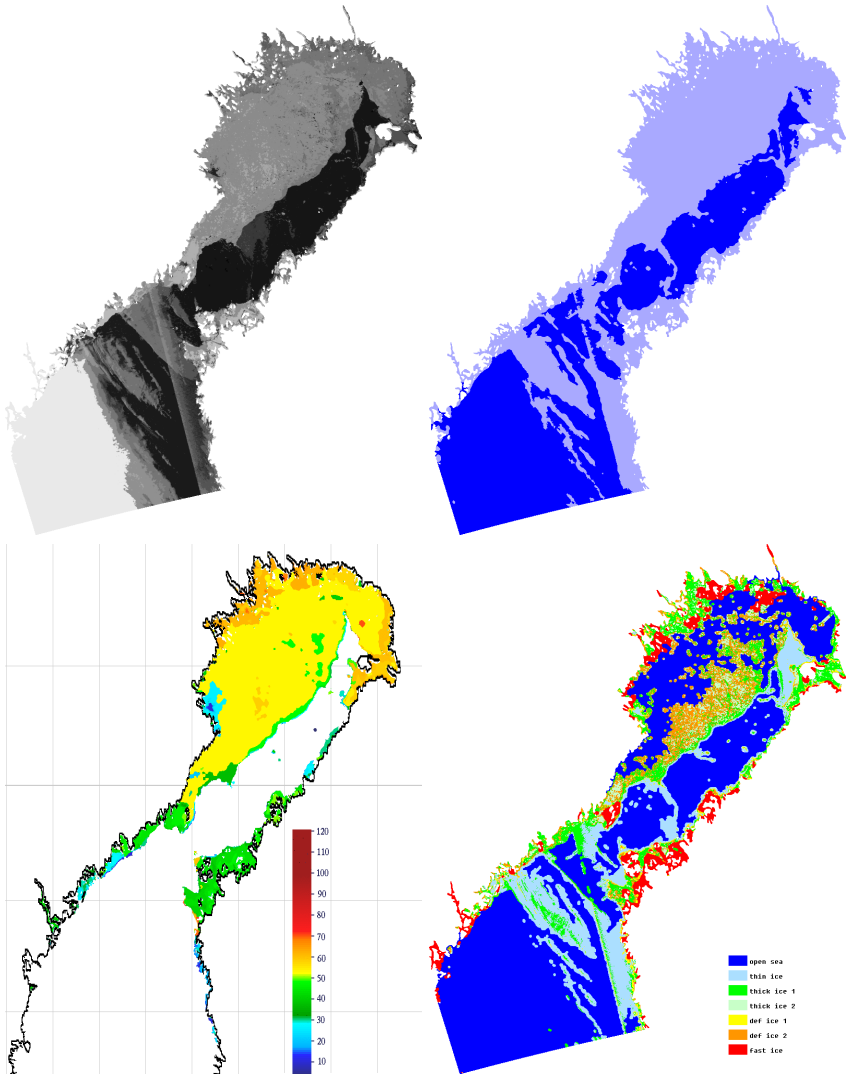

Figure 9.2: Segmentation result (upper left) corresponding to the SAR in Fig. 9.1, the segments are filled with the segment mean values, open water classification (upper right), SAR-based ice thickness chart (lower left), and ice classification based on the old operational algorithm (lower right).

Bibliography

[1] S. Ahmed, H. R. Warren, M. D. Symonds, R. P. Cox, The Radarsat System, IEEE Trans. Geoscience and Remote Sensing, v. 28, n. 4, pp. 598-602, 1990.

[2] M. Antonini, M. Barlaud, P. Mathieu, I. Daubechies, Image coding using wavelet transform, IEEE Trans. Image Proc., v. 1, n. 2, pp. 205-220, April, 1992.

[3] G. Arfken, Gram-Schmidt Orthogonalization, §9.3 in Mathematical Methods for Physicists, 3rd ed, Academic Press, pp. 516-520, 1985.

[4] H. H. Arsenault, G. April, Properties of speckle integrated with a finite aperture and logarithmic transformation, Opt. Soc. Amer., v. 66, n. 11, pp. 1160-1163, 1976.

[5] Atlantis Scientific Inc., Theory of Synthetic Aperture Radar, available at URL http://eos1.snu.ac.kr/~djkim/k_page/remote/sar/sar_theory/sar_theory.html, 1997.

[6] G. H. Ball, D. J. Hall, ISODATA, an Iterative Method of Multivariate Analysis and Pattern Recognition, Proc. IEEE Int. Communications Conference, 1966.

[7] D. G. Barber, E. F. LeDrew, SAR Sea Ice Discrimination Using Texture Statistics: A Multivariate Approach, Photogrammetric Engineering & Remote Sensing, v. 57, n. 4, pp. 385-395, 1991.

[8] D. G. Barber, D. Johnson, E. F. LeDrew, Measuring Climatic State Variables from SAR Images of Sea Ice: The SIMS SAR Validation Site in Lancaster Sound, Arctic, v. 44, supp. 1, pp. 108-121, 1991.

[9] D. G. Barber, M. E. Shokr, R. A. Fernandez, E. D. Soulis, D. G. Flett, E. F. LeDrew, A Comparison of Second Order Classifiers for SAR Sea Ice Discrimination, Photograametric Engineering and Remote Sensing, v. 59, n. 9, pp. 1397-1408, 1993.

[10] R. A. Baxter SAR image compression with the Gabor transform, IEEE Trans. Geoscience and Remote Sensing, v. 37, n. 1, pp. 574-588, 1999.

[11] A. J. Bell, T. J. Sejnowski, The Independent Components of Natural Scenes Are Edge Filters, Vision Research, v. 37, n. 23, pp. 3327-3338, 1997.

[12] C. Bertoia, M. R. Keller, D. Gineris, L.-K. Soh, C. Tsatsoulis. Operational Evaluation of a Knowledge-Based Sea Ice Classification System, World Meteorological Organization (WMO) Steering Group for Global Digital Sea Ice Data Bank - Eighth Session and WMO Workshop on Mapping and Archiving Sea Ice Data Derived from Radar Data Processing, Ottawa, Canada, 2000.

[13] J. Besag, On the Statistical Analysis of Dirty Pictures, J. R. Statis. Soc. B, v. 48, n. 3, pp. 259-302, 1986

[14] G. Borgefors, Chamfering: A Fast Method for Obtaining Approximations of the Euclidean Distance in N Dimensions, Proc. of the 3rd Scandinavian Conference on Image Analysis, pp. 250-255, 1983.

[15] J. N. Bradley, Storage and Retrieval of Large Digital Images, U.S. Patent No. 5710835. Online http:/patft.uspto.gov, 1998.

[16] P. Brodatz, Textures - A Photographic Album for Artists and Designers. Dover Publications, New York, 1966.

[17] R. W. Buccirossi, E. P. Simoncelli, Image compression via joint statistical characterization in the wavelet domain, IEEE Trans. Image Processing, v. 8, n. 12, pp. 1688-1701, 1999.

[18] D. Wei, H. Guo, J. Odegard, M. Lang, and C. Burrus, Simultaneous speckle reduction and data compression using best wavelet packet bases with application to SAR based ATD/R, in Proc. SPIE, v. 2491, Orlando, FL., Apr., 1995.

[19] P. J. Burt, E. H. Adelson, The Laplacian pyramid as a compact image code, IEEE. Trans. Communications, v. 31, n. 4, pp. 532-540, 1983.

[20] E. Candes and D. Donoho, Ridgelets: a key to higher-dimensional intermittency?, Phil. Trans. R. Soc. Lond., Ser. A, v. 357, pp. 2495-2509, 1999.

[21] J. Canny, A Computational Approach to Edge Detection, IEEE Trans. Pattern Analysis and Machine Intelligence, v. 8, n. 6, pp. 679 - 698, 1986.

[22] Jean-Francois Cardoso, Blind signal separation: statistical principles. Proc. IEEE, v. 9, n. 10, pp. 2009-2025, 1998.

[23] A. Carlström, Simulation of Synthetic-Aperture Radar Images of Baltic Sea Ice, Research Report 168, Dept. of Radio and space Science, Chalmers Univ. of Technology, Sweden, 1992.

[24] A. Carlström, L. M. H. Ulander, C-Band Backscatter Signatures of Old Sea Ice in the Central Arctic During Freeze-Up, IEEE Trans. Geoscience and Remote Sensing, v. 31, n. 4, pp. 819-829, 1993.

[25] A. Carlström, L. M. H. Ulander, W. Dierking, Radar Backscattering Models and ERS-1 Data Inversion for Baltic Sea Ice, Baltic Experiment for ERS-1 (BEERS), Winter Navigation Research Board, Research Report 51, Göteborg, 1994.

[26] A. Carlström, L. M. H. Ulander, Validation of Backscatter Models for Level and Deformed Sea Ice in ERS-1 SAR Images, Int. J. Remote Sensing, v. 16, n. 17, pp. 3245-3266, 1995.

[27] A. Carlström, Modelling Microwave Backscatter from Sea Ice for Synthetic-Aperture Radar Applications, Technical Report 271, Chalmers University of Technology, Sweden, 1995.

[28] A. Carlström, L. M. H. Ulander, W. Dierking, Radar Scattering Models and ERS-1 SAR Data Inversion for Baltic Sea Ice, in Baltic Experiment for ERS-1 (BEERS), Winter Navigation Research Board, Research Report 51, National Maritime Administration, Sweden, 1995.

[29] A. Carlström, A Microwave Backscattering Model for Deformed First-Year Sea Ice and Comparisons with SAR Data, IEEE Trans. Geoscience and Remote Sensing, v. 35, n. 2, pp. 378-391, 1997.

[30] G. Celeux, J. Diebolt, The SEM Algorithm: A Probabilistic Teacher Algorithm Derived from the EM Algorithm for the Mixture Problem, Computational Statistics Quarterly, v. 2, n. 1, pp. 73–82, 1985.

[31] G. Celeux, D. Chauveau, J. Diebolt, On Stochastic Versions of the EM Algorithm, Institut National de Recherche en Informatique et en Automatique (INRIA) report 2514, France. Available online at http://www.inria.fr/rrrt/rr-2514.html, 1995.

[32] D. Cheng, Q. Pu, K. Cheng, H. Burkhardt, Possibilistic Hopfield Neural Network on CT Brain Hemorrhage Image Segmentation, Proceedings of the 4th Asian Conference on Computer Vision, pp. 871-876, 2000.

[33] D. A. Clausi, Comparison and Fusion of Co-Occurrence, Gabor and MRF Features for Classification of Sea Ice SAR Imagery, ATMOSPHERE-OCEAN, n. 3, v. 39, pp.183-194, 2001.

[34] S. R. Cloude, E. Pottier, Concept of Polarization Entropy in Optical Scattering, Optical Engineering, v. 34, n. 6, pp. 1599-1610, 1995.

[35] A. Cohen, I. Daubechies, O. Guleryuz, and M. Orchard, On the importance of combining wavelet-based non-linear approximation with coding strategies, submitted to IEEE Trans. Image Processing, 2000.

[36] R. Cook, I. McConnell, C. J. Oliver, MUM (Merge Using Moments) Segmentation of SAR Images, Europto Conf. on SAR Data Processing for Remote Sensing, Proc. SPIE, v. 2316, pp. 92-103, 1994.

[37] T. M. Cover, P. E. Hart, Nearest neighbor pattern classification, IEEE Trans. Inform. Theory, v. IT-13, pp. 21-27, 1968.

[38] M.S. Crouse, R.D. Nowak, R.G. Baraniuk Wavelet-based Statistical Processing Using Hidden Markov Models, IEEE Trans. Signal Processing, v. 46, n. 4, pp. 886-902, 1998

[39] T. M. Cover and J. A. Thomas, Elements of Information Theory, John Wiley & Sons, 1991.

[40] Foreign Trade Transportations 2001, Statistics by the Finnish Customs, 2002.

[41] P. B. G. Dammert, M. Leppäranta and J. Askne, SAR interferometry over Baltic sea ice, Int. J. Remote Sensing, n. 16, v. 19, pp. 3019-3037, 1998.

[42] I. Daubechies, Ten Lectures on Wavelets, Society for Industrial and Applied Mathematics (SIAM), 1992.

[43] M. Davison, Development of Neural Network Techniques for the Classification of Multi-Temporal ERS-1 SAR Imagery with respect to Agricultural Applications, Proceedings of the First ERS-1 Pilot Project Workshop, ESA Publications, 1994.

[44] A. P. Dempster, N. M. Laird, D. B. Rubin, Maximum Likelihood from Incomplete Data via the EM Algorithm, Journal of the Royal Statistical Society Series, v. 39, n. 1, pp. 1-38, 1977.

[45] S. Derrode, G. Mercier, J-M. Le Caillec, R. Garello, Estimation of Sea-Ice SAR clutter statistics from Pearson's system of distributions, IEEE Int. Conf. on Geoscience and Remote Sensing 2001 (IGARSS'01), Sydney (Australia), 2001.

[46] S. Derrode, W. Pieczynski, SAR Image Segmentation Using Generalized Pairwise Markov Chains, Proc. SPIE International Symposium on Remote Sensing, 2002.

[47] W. Dierking, A. Carlström, L. M. H. Ulander, The Effect of Inhomogeneous Roughness on Radar Backscattering from Slightly Deformed Sea Ice, IEEE Trans. Geoscience and Remote Sensing, v. 35, n. 1, pp. 819-829, 1997.

[48] W. Dierking, J. Askne, M. Pettersson, Baltic sea ice observations during EMAC-95using multifrequency scatterometry and EMISAR data. EMAC 94/95 Final Results, Noordwijk, WPP-136 (ESA), pp. 171-177, 1997.

[49] W. Dierking, J. Askne, Polarimetric L- and C-band SAR signatures of Baltic sea ice observed during EMAC-95. In Future Trends in Remote Sensing, edited by P. Gudmandsen, A.A. Balkema, Rotterdam, pp. 329-336, 1998.

[50] W. Dierking, Quantitative Roughness Characterization of Geological Surfaces and Implications for Radar Signature Analysis, IEEE Trans. Geoscience and Remote Sensing, v. 37, n. 5, pp. 2397-2412, 1999.

[51] W. Dierking, Multifrequency Scatterometer Measurements of Baltic Sea Ice During EMAC-95, International Journal of Remote Sensing, v. 20, n. 2, pp. 349-372, 1999.

[52] W. Dierking, H. Skriver, P. Gudmandsen, SAR Polarimetry for Sea Ice Classification, Proc. of the ESA POLinSAR Workshop, 2003.

[53] S.T. Dokken, B. Håkansson, J. Askne, Inter-comparison of arctic sea ice concentration using Radarsat, ERS, SSM/I and in-situ data. Canadian Journal of Remote Sensing, v. 26, n. 6, pp. 521-536, 2000.

[54] G.Donato, M. S. Bartlett, J. C. Hager, P. Ekman, T. J. Sejnowski, Classifying Facial Actions, IEEE Trans. PAMI, v. 21, n. 10, 1999.

[55] D. Donoho, De-noising by Soft-Thresholding, IEEE Trans. Information Theory, v. IT-41, n. 3, pp. 613-627, May 1995.

[56] M. R. Drinkwater, D. P. Winebrenner, E. Rignot, Multifrequency Polarimetric Synthetic Aperture Radar Observations of Sea Ice, Journal of Geophysical Research, v. 96, n. C11, pp. 20679-20698, 1991.

[57] R. Eckhorn, H. J. Reitboeck, M. Arndt, P. Dicke, Feature Linking via Synchronization among Distributed Assemblies : Simulations of Results from Cat Visual Cortex, Neural Computation, v. 2, pp. 293-307, 1990

[58] L. Eriksson, M. Drinkwater, O. Nortier, SIR-C Polarimetric Results from the Weddell Sea, Antarctica, Trans. Trans. IEEE International Conference on Geoscience and Remote Sensing 1998 (IGARSS'98), 1998.

[59] G. Fan, X.-G. Xia, A Joint Multi-context and Multi-scale Approach to Bayesian Image Segmentation, IEEE Trans. Geoscience and Remote Sensing, v. 39, n. 12, 2001.

[60] H. G. Feichtinger, T. Strohmer (ed.), Gabor Analysis and Algorithms, Birkhauser, 1997.

[61] F. M. Fetterer, D. Gineris, R. Kwok, Sea Ice Type Maps from Alaska Synthetic Aperture Radar Facility Imagery: An Assessment, Journal of Geophysical Research, v. 99, n. C11, pp. 22443-22458, 1994.

[62] S. Fiori, Overview of Independent Component Analysis Technique with an Application to Synthetic Aperture Radar (SAR) Imagery Processing, Neural Networks, v. 16, n. 3-4, pp. 453-467, 2003.

[63] R. Fjortoft, Y. Delignon, W. Pieczynski, M. Sigelle, F. Tupin Unsupervised classification of radar images using hidden Markov chains and hidden Markov random fields IEEE Trans. Geoscience and Remote Sensing, v. 41 n. 3 , pp. 675-686, 2003.

[64] D. L. Donoho, A. G. Flesia, Can recent innovations in the harmonic analysis 'explain' the key findings in natural image statistics, Preprint, Stanford University, Statistics Department, 2001.

[65] F. L. Van Nes, M. A. Bouman, Spatial modulation in the human eye, Journal of the Optical society of America, v 57, n 3, pp 401-406, March, 1967.

[66] G. Franchescetti, A. Iodice, M. Migliaccio, D. Riccio, Scattering from Natural Rough Surfaces Modeled by Fractional Brownian motion Two-Dimensional Processes, IEEE Trans. Antennas and Propagation, v. 47, n. 9, pp. 1405-1415, 1999.

[67] A. K. Fung, Z. Li, K. S. Chen, Backscattering from a Randomly Rough Dielectric Surface, IEEE Trans. Geoscience and Remote Sensing, v. 30, n. 2, pp. 356-369, 1992.

[68] D. Gabor, Theory of Communication. The Journal of the Institute of Electrical Engineers, v. 93, n. 21 (Part III), pp. 429–457, 1946.

[69] S. Geman, D. Geman, Stochastic Relaxation, Gibbs Distributions, and the Bayesian Restoration of Images, IEEE Trans. Pattern Analysis and Machine Intelligence, v. PAMI-6, p. 721-741, 1984

[70] S. Ghael, A. Sayeed, R. Baraniuk, Improved Wavelet Denoising via Empirical Wiener Filtering, Proc. SPIE 3169, pp. 389-399, 1997.

[71] R. S. Gill, SAR Ice Classification Using Fuzzy Screening Method, Proc. Workshop on SAR polarimetry and polarimetric interferometry, Frascati, Italy, 2003.

[72] B. Girod, Psychovisual aspects of image communication, Signal Processing, v 28, pp 239-251, 1992.

[73] K. M. Golden, D. Borub, M. Cheney, E. Cherkaeve, M. S. Dawson, K.-H. King, A. K. Fung, D. Isaacson, A. Johnson, A. K. Jordan, J. A. Kong, R. Kwok, S. V. Nghiem, R. G. Onstott, J. Sylvester, D. B. Winebrenner, I. H. H. Zabel, Inverse electromagnetic Scattering Models for Sea Ice, IEEE Trans. Geoscience and Remote Sensing, v. 36, n. 5, pp. 1675-1704, 1999.

[74] C. H. Graham ed., Vision and Visual Perception, 2nd edition, John Wiley & Sons, 1966.

[75] P. J. Green, Reversible Jump Markov Chain Monte Carlo Computation, and Bayesian Model Determination, Biometrika, v. 82, pp. 711-732, 1995.

[76] H. Grönvall, A. Seinä, M. Similä, The Finnish Ice Service and Real-Time Automatic Classification of SAR Data, Nordic space activities v. 4, n. 4, pp. 28–29, 33–35, 1996.

[77] H. Grönvall, A. Seinä, The IMSI Results in the Baltic Sea: Digital Sea Ice Products to the Users at Sea, Proc. POAC'99 (Proceedings of the 15th International Conference on Port and Ocean Engineering under Arctic Conditions, Espoo, Finland), v. 1, pp 210-219, 1999.

[78] H. Grönvall, A. Seinä, 2000. Toward Optimal Sea-Ice Monitoring in the Baltic Sea, Proc. of ICES Symposium, Helsinki, 1998, ICES Journal of Marine Science 56(suppl), pp 165-171, 2000.

[79] C. Haas, W. Dierking, M. Lensu, Airborne Measurements of Baltic Ice Thickness in February 2003: The Campaign, Report of the EU-project IRIS (EVK3-CT-2002-00833), 2003.

[80] C. Haas, IRIS Data Report: Airborne EM Measurements of Baltic Ice Thickness in February 2003, Report of the EU-project IRIS (EVK3-CT-2002-00833), 2003.

[81] C. Haas, Airborne EM Sea-Ice Thickness Profiling over Brackish Baltic Sea Water, in Proc. of the International Symposium on Ice St. Petersburg, 2004.

[82] M. Hallikainen, F. T. Ulaby, M. Abdelrazik, Dielectric Properties of Snow in the 3 to 37 GHz Range, IEEE Trans. Antennas and Propagation, v. AP-34, n. 11, pp. 1329-1340, 1986.

[83] M. Hallikainen, Review of the Microwave Dielectric and Extinction Properties of Sea Ice and Snow, Trans. of the IEEE Geoscience and Remote Sensing Symposium (IGARSS'92), pp. 961–965, 1992.

[84] M. Hallikainen, J. Hyyppä, J. Haapanen, T. Tares, P. Ahola, J. Pulliainen, M. Toikka, A Helicopter-Borne Eight-Channel Ranging Scatterometer for Remote Sensing - Part I: System Description, IEEE Trans. Geoscience and Remote Sensing, v. 31, pp. 161-169, 1993.

[85] M. Hallikainen, M. Nikulainen, H. Taskinen, E. Panula-Ontto, L. Kurvonen, M. Kemppinen, EMAC-95 Snow and Ice Airborne Campaign, Proceedings of the IEEE International Geoscience and Remote Sensing Symposium 1995 (IGARSS'95), pp. 1811-1813, 1995.

[86] M. Hallikainen, P. Ahola, K. Rautiainen, J. Pihlflyckt, T. Tirri, M. Mäkynen, J. Lahtinen, H. Servomaa, P. Makkonen, J. Grandell, M. Kemppinen, Overview of EMAC'95 snow and ice airborne campaign in Finland. Proceedings of the International Geoscience and Remote Sensing Symposium 1996, (IGARSS'96), pp. 1998-2001, 1996.

[87] R. M. Haralick, K. Shanmugam, I. Dinstein, Textural features for image classification, IEEE Trans. Syst. Man and Cybern., v. SMC-3, pp. 610–621, 1973.

[88] D. Harwood, M. Subbarao, H. Hakalahti, L.S. Davis, A New Class of Edge-Preserving Smoothing Filters, Pattern Recognition Letters, v. 6, pp. 155-162, 1987.

[89] D. Haverkamp, L.-K. Soh, C. Tsatsoulis, A Comprehensive Automated Approach to Determining Sea Ice Thickness from SAR Data, IEEE Trans. Geoscience and Remote Sensing v. 33, n. 1, pp. 46-57, 1995.

[90] E.-A. Herland, R. Berglund Demonstration of Operational Sea-Ice Monitoring in the Baltic Sea with ERS-1 SAR Int. J. Remote Sensing, v. 16, n. 17, pp. 3427-3439, 1995.

[91] E. Hoekman, Speckle ensemble statistics of logarithmically scaled data, IEEE Trans. Geoscience and Remote Sensing, v. 29, n. 1, pp. 180-182, 1991.

[92] J. J. Hopfield, Neural Networks and Physical Systems with Emergent Collective Computational Abilities, Proceedings of the National Academy of Sciences, pp. 2554-2558. National Academy of Sciences, 1982.

[93] P. G. Howard, J. S. Vitter, Practical Implementations of Arithmetic Coding, Image and Text Compression, pp. 85-112, Kluwer Academic Publishers, 1992.

[94] A. Hyvärinen and E. Oja, A Fast Fixed-Point Algorithm for Independent Component Analysis. Neural Computation, v. 9, n. 7, pp. 1483-1492, 1997.

[95] A. Hyvärinen, New Approximations of Differential Entropy for Independent Component Analysis and Projection Pursuit, Advances of Neural Information Processing Systems, v. 10, pp. 273-279, MIT Press, 1998.

[96] A. Hyvärinen, Fast and Robust Fixed-Point Algorithms for Independent Component Analysis. IEEE Trans. Neural Networks, v. 10, n. 3, pp. 626-634, 1999.

[97] A. Hyvärinen, Gaussian Moments for Noisy Independent Component Analysis. IEEE Signal Processing Letters, v. 6, n. 6, pp. 145-147, 1999.

[98] A. Hyvärinen and E. Oja, Independent Component Analysis: Algorithms and Applications. Neural Networks, v. 13, n. 4-5, pp. 411-430, 2000.

[99] A. Hyvärinen, J. Karhunen, E. Oja, Independent Component Analysis, John Wiley & Sons, 2001.

[100] IEEE Trans. Geoscience and Remote Sensing, v. 36, n. 5. Special Issue on Sea Ice Electromagnetics, 1999.

[101] N. Jayant, J. Johnston, R. Safranek, Signal compression based on models of human perception, Proc. of the IEEE, v 81, n 10, pp 1385-1422, October, 1993.

[102] R. Jenssen, T. Eltoft, ICA Filter Bank for Segmentation of Textured Images, Proceedings of the International Symposium on Independent Component Analysis and Blind Signal Separation (ICA2003), pp. 827-832, 2003.

[103] J. L. Johnson, Pulse-Coupled Neural Nets: Translation, Rotation,Scale, Distortion, and Intensity Signal Invariances for Images, Applied Optics, v. 33(26), pp. 6239-6253, 1994

[104] D. S. Jones, Acoustic and Electromagnetic Waves, Oxford Science Publications, 1989.

[105] L. Kaleschke, S. Kern, ERS-2 SAR Image Analysis for Sea Ice Classification in the Marginal Ice Zone., Proc. International Geoscience and Remote Sensing Symposium 2002 (IGARSS'02), p. 3038-3040, 2002.

[106] P. Kankaanpää, Distribution, Morphology, and Structure of Sea Ice Pressure Ridges in the Baltic Sea, doctoral Thesis, Department of Geography, University of Helsinki, 1998.

[107] J. Karvonen, M. Similä, Classification of Sea Ice Types from ScanSAR Radarsat Images Using Pulse-Coupled Neural Networks, Proc. IEEE International Conference on Geoscience and Remote Sensing (IGARSS'98), pp. 2505-2508, 1998

[108] J. Karvonen and M. Similä, Pulse-Coupled Neural Networks for Sea Ice SAR Image Segmentation and Classification. Proc. Workshop on Virtual Intelligence - Dynamic Neural Networks 1998 (VI-DYNN'98), Proc. SPIE v. 3728, pp. 333-350, 1999.

[109] J. Karvonen, Fractal coding of SAR images, Technical Report, Finnish Institute of Marine Research, 2000.

[110] J. Karvonen, M. Similä and M. Mäkynen, An Iterative Incidence Angle Normalization Algorithm for Sea Ice SAR Images, Proc. IEEE International Geoscience and Remote Sensing Symposium 2002 (IGARSS'02), v. III, pp. 1524-1528, 2002.

[111] J. Karvonen, M. Similä, A wavelet transform coder supporting browsing and transmission of sea ice SAR imagery, IEEE Trans. Geoscience and Remote Sensing, v. 40, n. 11, pp. 2464- 2485, 2002.

[112] J. Karvonen, M.Similä, ICA-Based Classification of Sea Ice SAR Images, Proceedings of the 23rd European Association of Remote Sensing Laboratories (EARSeL) Annual Symposium, Gent, Belgium, pp. 211-217, 2003.

[113] J. Karvonen, M. Similä, I. Heiler, Ice Thickness Estimation Using SAR Data and Ice Thickness History, Proceedings of the IEEE International Geoscience and Remote Sensing Symposium 2003 (IGARSS'03), v. I, pp. 74-76, 2003.

[114] J. Karvonen, Feature Detection from Preprocessed Sea Ice SAR Data Based on Higher-Order Statistics, Proceedings of the IEEE International Geoscience and Remote Sensing Symposium 2003 (IGARSS'03), v. VI, pp. 3450-3452, 2003.

[115] J. Karvonen, Baltic Sea Ice SAR Segmentation and Classification Using Modified Pulse Coupled Neural Networks, IEEE Trans. Geoscience and Remote Sensing, v.42, n. 7, pp. 1566-1574, 2004.

[116] J. Karvonen, M. Similä, J. Haapala, C. Haas, M. Mäkynen, Comparison of SAR Data and Operational Sea Ice Products to EM Ice Thickness Measurements in the Baltic Sea, Proc. IEEE International Geoscience and Remote Sensing Symposium (IGARSS'04), v. V, pp. 3021-3024, 2004.

[117] J. Karvonen, M. Similä, M. Mäkynen, Open Water Detection from Baltic Sea Ice SAR Imagery, Proc. IEEE International Geoscience and Remote Sensing Symposium (IGARSS'04), v. VII, pp. 4382-4385, 2004.

[118] J. Karvonen, Comparison of Some Speckle Filtering Methods for Radarsat-1 Sea Ice Data, Internal Report, Finnish Institute of Marine Research, 2004.

[119] L. Kaufman, Sight and Mind, an Introduction to Visual Perception, Oxford university Press, 1974.

[120] H. Kemppainen, The applicability of Synthetic Aperture Radar in Studying Ice Properties in the Gulf of Bothnia (in Finnish), M. Sc. thesis, Helsinki University of Technology, Department of Land Survey, 1989.

[121] B. Kerman, Fusion of dual-frequency sar imagery of sea ice. Atmosphere-Ocean, v. 37, n. 4, pp. 417-438, 1999.

[122] B. S. Kim, R. K. Moore, R. G. Onstott, S. Gogoneni, Towards Identification of Optimum Radar Parameters for Sea-Ice Monitoring, Journal of Glaciology, v. 31, n. 109, pp. 214-219, 1985.

[123] T. Kohonen, Self-Organization and Associative Memory, 3rd edition, Springer-Verlag, 1989.

[124] D. Kovacevic, S. Loncaric, Radial Basis Function-Based Image Segmentation Using a Receptive Field, Proc. of the IEEE Symposium on Computer-Based Medical Systems, pp. 126-130, 1997.

[125] D.T. Kuan, A.A. Sawchuk, T.C. Strand, and P. Chavel, Adaptive restoration of images with speckle, IEEE Trans. Acoustics, Speech and Signal Proc., v. 35, n. 3, pp. 373-383, 1987.

[126] R. Kuittinen, M. Leppäranta, Real-Time System for Transmitting Satellite Data Products to Icebreakers, Advances in Space Research, v. 9, n. 7, pp. 393-397, 1989.

[127] G. Kuntimad, H. S. Ranganath, Perfect Image Segmentation Using Pulse Coupled Neural Networks, IEEE Trans. Neural Networks, v. 10, n. 3, pp. 591-598, 1999.

[128] M. Kuwahara, Processing of RI-angiocardiographic images, in Digital Processing of Biomedical Images, ed. K. Preston and M. Onoe, Plenum Press, New York, pp. 187-203, 1976.

[129] R. Kwok, G. F. Cunningham, Backscatter characteristics of the Winter Ice Cover of the Beaufort Sea, Journal of Geophysical Research, v. 99, n. C4, pp. 7787-7802, 1994.

[130] M. Laakso, SFT - Smart File Transfer, ERCIM News, n. 37, pp. 31-32, http://www.ercim.org/publication/Ercim_News/enw37, 1999.

[131] A. Labbi, H. Bosch, C. Pellegrini, Higher Order Statistics for Image Classification, Int. Journal of Neural Systems, v. 11, n. 4, pp. 371-377, 2001.

[132] P. Lacomme, J-P. Hardange, J-C. Marchais, E. Normant, Air and Spaceborne Radar Systems: An Introduction, SciTech Publishing Inc., 2001.

[133] G. G. Langdon, Jr., An introduction to arithmetic coding, IBM Journal Res. Develop., n. 2, pp. 135-149, 1984.

[134] J. S. Lee, Refined filtering of image noise using local statistics, Computer Vision, Graphics and Image Processing, V. 15, pp. 380-389, 1981.

[135] J.-S. Lee, I. Jurkevich, Segmentation of SAR Images, IEEE Trans. Geoscience and Remote Sensing, v. 27, n. 6, pp. 674-680, 1989.

[136] J.-S. Lee, M. Grunes, R. Kwok, Classification of Multi-look Polarimetric SAR Imagery Based on Complex Wishart Distribution, Int. J. of Remote Sensing, v. 15, n. 11, pp. 2299-2311, 1994.

[137] T.-W. Lee, M. S. Lewicki, T. J. Sejnowski, ICA Mixture Models for Unsupervised Classification of Non-Gaussian Classes and Automatic Context Switching in Blind Signal Separation, IEEE Trans. Pattern Analysis and Machine Intelligence, v.22, n. 10, pp. 1078-1089, 2000.

[138] M. Leppäranta, T. Thompson, Sea Ice Remote Sensing with Synthetic Aperture Radar in the Baltic Sea, Earth Observation System (EOS), Trans. of American Geophysical Union, v. 70, n. 28, pp. 698-699, 708-709, 1989.

[139] M. Leppäranta, T. Thompson, On the Potentials of SAR in ice mapping in the Baltic Sea, Proc. of the EARSeL 1990, pp. 381-385, 1990.

[140] M. Leppäranta, R.Kuittinen, J. Askne, BEPERS Pilot Study : an Experiment with X-band Synthetic Aperture Radar over Baltic Sea Ice, Journal of Glaciology, v. 38, n. 128, pp. 23-35, 1992.

[141] M. Lewicki, B. Olshausen, Inferring Sparse Overcomplete Image Codes Using an Efficient Coding Framework, Advances in Neural Information Processing Systems 10, pp. 556-562, 1998.

[142] A. S. Lewis, G. Knowles, Image compression using the 2-D wavelet transform, IEEE Trans. Image Proc., v. 1, n. 2, pp. 244-256, April 1992.

[143] J. E. Lewis, M. Leppäranta, and H. B. Granberg, Statistical properties of sea ice surface topography in the Baltic Sea, Tellus, v. 45A, pp. 127-142, 1993.

[144] A. Li, P.B.G. Dammert, G. Smith, and J. Askne, Fuzzy C-Means Clustering Algorithm for Classification of Sea Ice and Land Cover from SAR Images, Proc. of European Symposium on Aerospace Remote Sensing: Image Processing, Signal Processing and Synthetic Aperture Radar for Remote Sensing, Proc. SPIE, v. 3217, pp. 86–97, 1997.

[145] Linde, Y., Buzo, A., and Gray, R. M. (1980). An algorithm for vector quantizer design. IEEE Trans. Communication, v 28, n 1, pp 84-95, 1980.

[146] A. Lopes, R. Touzi, E. Nezry, Adaptive Speckle Filters and Scene Heterogeneity, IEEE Trans. Geoscience and Remote Sensing, V. 28, No. 6, November 1990.

[147] M. Lundhaug, ERS SAR Studies of Sea Ice Signatures in the Pechora Sea and Kara Sea Region, Canadian Journal of Remote Sensing, v. 28, n. 2, pp. 114-127, 2002.

[148] M. Lundin, M.Sc. Remote Sensing of Snow Covered Sea Ice in Brackish Water - Investigations from the Baltic Sea, Licentiate Thesis, Chalmers University of Technology, Technical Report No. 395L, Department of Radio and Space Science, Sweden, 2001.

[149] T. Lindblad, J. M. Kinser, Image Processing using Pulse-Coupled Neural Networks, Springer-Verlag, 1998.

[150] K. Mäkisara, R. Berglund, Y. Rauste, T. Tikkanen, J. Savola, R. Kuittinen, M. Leppäranta, J. Pohjola, Digital Transmission of Satellite Images to Ice Breakers (in Finnish), VTT Research Note No. 1165, 1990.

[151] K. Mäkisara, Adaptive Laplacian pyramid compression of remote sensing images, IEEE Proc. on Int. Conf. on Geoscience and Remote Sensing Symposium (IGARSS'91), pp. 1439-1442, 1991.

[152] M. Mäkynen, M. Hallikainen, C-Band Backscattering Signatures of Baltic Sea Ice, Proc. of the IEEE Int. Conf. on Geoscience and Remote Sensing (IGARSS'98), pp. 983-985, 1998.

[153] M. Mäkynen, Investigation of Passive and Active Microwave Signatures of the Baltic Sea Ice, Lic. Tech. Thesis, Helsinki University of Technology, 1999.

[154] M. Mäkynen, T. Manninen, M. Similä, J. Karvonen, M. Hallikainen, Incidence Angle Dependence of the Statistical Properties of C-Band HH-Polarization Backscattering Signatures of the Baltic Sea Ice, IEEE Trans. Geoscience and Remote Sensing, v. 40, n. 12, pp. 2593-2605, 2002.

[155] M. Mäkynen, M. Hallikainen, Investigation of C-Band and X-Band Backscattering Signatures of the Baltic Sea Ice, International Journal of Remote Sensing, v. 25, n. 11, pp. 2061-2086, 2004.

[156] M. Mäkynen, ESSI-2, ENVISAT and the Baltic Sea Ice Conditions, Final Report, Helsinki University of Technology / Laboratory of Space Technology, 2005.

[157] D. H. Maling, Coordinate Systems and Map Projections, London: George Philip and Son Ltd, 1973

[158] S. Mallat and S. Zhong, Characterization of signals from multiscale edges, IEEE Trans. Pattern Analysis, v. 14, n. 7, pp. 710-732, July 1992.

[159] S. G. Mallat and W. L. Hwang, Singularity detection and processing with wavelets, IEEE Trans. Information Theory, v. 38, n. 2, pp. 617-643, March 1992.

[160] S. Mallat, A Wavelet Tour of Signal Processing, 2nd edition, Academic Press, 1999.

[161] A. T. Manninen, Effects of Ridge Properties on Calculated Surface Backscattering in BEPERS-88, Int. Journal of Remote Sensing, v. 13, n. 13, pp. 2469-2487, 1992.

[162] A. T. Manninen, Backscattering from a dielectric surface with a continuous roughness spectrum, Meri, Report series of FIMR v. 23, pp. 1-26, 1996.

[163] A. T. Manninen, Microwave Surface Backscattering and Surface Roughness of Baltic Sea Ice, Dr. Tech. Dissertation, Finnish Marine Research, n. 265, 1996.

[164] A. T. Manninen, Multiscale Surface roughness and Backscattering, Progress in Electromagnetic Research, v. 16, pp. 173-201, 1997.

[165] A. T. Manninen, Multiscale Surface roughness and Backscattering - Summary, Journal of Electromagnetic Waves and Applications, v. 11, pp. 471-475, 1997.

[166] M. Miyahara, K. Kotani, V. R. Algazi, Objective picture quality scale (PQS) for image coding, IEEE Trans. Communications, v. 46, n. 9, pp. 1215-1226, 1998.

[167] A. B. Lee, K. S. Pedersen, and D. Mumford, The nonlinear statistics of high-contrast patches in natural images, Brown University, Division of Applied Mathematics, Preprint, 2001.

[168] NOAA, Observers' Guide to Sea Ice, National Oceanic and Atmospheric Administration (NOAA), National Ocean Service, Office of Response and Restoration, draft. Online at http://response.restoration.noaa.gov/oilaids/seaice/seaice.html, 2001.

[169] J. A. Nystuen, F. W. Garcia, Sea Ice Classification Using SAR Backscatter Statistics, Trans. Geoscience and Remote Sensing, v. 30, n. 3, pp. 502-509, 1992.

[170] C. Oliver, Information from SAR Images, J. Phys. D: Appl. Phys. v. 24, pp. 1493-1514, 1991.

[171] C. Oliver, S. Quegan Understanding Synthetic Aperture Radar Images, Artech-House, 1998.

[172] B. Olshausen, D. Field, Emergence of Simple-Cell Receptive Field Properties by Learning a Sparse Code for Natural Images, Nature, v. 381, pp. 607-609, 1996.

[173] J. R. Orlando, R. Mann, S. Haykin, Classification of sea-ice images using a dual-polarized radar, IEEE Journal of Oceanic Engineering, v. 15 n. 3, pp. 228-237, 1990.

[174] N. Otsu, A Threshold Selection Method from Gray-Level Histograms, IEEE Trans. Systems, Man, and Cybernetics, V. SMC-9, No. 1, pp.62-66, 1979.

[175] N. R. Pal, S. K. Pal, A Review on Image Segmentation Techniques, Pattern Recognition, v. 26, n. 9, pp. 1277-1294, 1993.

[176] J. Park, J. W. Sandberg, Universal Approximation Using Radial Basis Functions, Neural Computation, v. 3, n. 2, pp. 246-257, 1991.

[177] W. B. Pennebaker, J. L. Mitchell, JPEG Still Image Data Compression Standard, New York : Van Nostrand Reinhold, 1993.

[178] P. Perona, J. Malik, Scale-Space and Edge Detection using Anisotropic Diffusion, IEEE Trans. Pattern Analysis and Machine Intelligence, v. 12, pp. 629-639, 1990.

[179] W. Pieczynski, Statistical Image Segmentation, Mach. Graph. and Vis., v. 1, n. 1/2, pp. 261-268, 1992.

[180] Radarsat Data Product Specifications, Document number RSI-GS-026, Radarsat International, 1997.

[181] H. S. Ranganath, G. Kuntimad, Image Segmentation Using Pulse Coupled Neural Networks, Proc. IEEE International Conference on Image Processing (ICIP'94), pp. 1285-1290, 1994

[182] C. C. Reyes-Aldasoro, A. L. Aldeco, Image Segmentation and Compression using Neural Networks, Proc. Advances in Artificial Perception and Robotics 2000, 2000.

[183] E. Rignot, R. Kwok, Characterization of Spatial Statistics of Distributed Targets in SAR Data, Int. Journal of Remote Sensing, v. 14, n. 2, pp. 345-363, 1992.

[184] E. Rignot, R. Kwok, Characterization of Spatial Statistics of Distributed Targets in SAR Data, Int. Journal of Remote Sensing, v. 14, n. 2, pp. 345-363, 1993.

[185] E. Rignot, M. R. Drinkwater, Winter Sea-Ice Mapping from Multi-Parameter Synthetic-Aperture Radar Data, Journal of Glaciology, v. 40, n. 134, pp. 31-45, 1994.

[186] J. Rissanen and G. G. Langdon, Jr., Arithmetic coding, IBM Journal Res. Develop., n. 2, pp. 149-162, 1979.

[187] J. Ruiz-del-Solar, D. Kottow, Neural-based Architectures for the Segmentation of Textures. Proc. of the 15th Int. Conf. on Pattern Recognition, ICPR 2000, v. 3, pp. 1092-1095, 2000.

[188] I. A. Rybak, N. A. Shevtsova, V. A. Sandler, The Model of Neural Network Visual Processor, Neurocomputing, v. 4, pp. 93-102, 1992

[189] R. J. Safranek, J. D. Johnston, A perceptually tuned sub-band image coder with image dependent quantization and post-quantization data compression, IEEE Proc. ICASSP'89, v. 3, pp. 1945-1948, 1989.

[190] A. Said, W. A. Pearlman, A New Fast and Efficient Image Codec Based on Set Partitioning in Hierarchical Trees, IEEE Trans. Circuits and Systems for Video Technology, v. 6, pp. 243-250, 1996.

[191] S. Sandven, A. Seinä, H. Grönvall, H. H. Valeur, H. S. Andersen, OSIMS: Operational Sea Ice Monitoring by Satellites in Europe, Proc. POAC'99, v. 2, p 508-517, 1999.

[192] S. Sandven, M. Mäkynyn, M. Hallikainen, H. Grönvall, A. Seinä, M. Similä, J. Karvonen, M. Nizovsky, A. Cavanie, R. Ezraty, R. Gill, H. H. Valeur, L. T. Pedersen, V. Alexandrov, A. Bogdanov, R. Tonboe, M. Lundhaug, O. Dalen, K. Kloster, IMSI (Integrated Use of New Microwave Satellite Data for Improved sea Ice Observation) Final Report, NERSC (Nansen Environmental and Remote Sensing Center) Technical Report 170, European Commission Environmental and Climate Program 1994-1998, contract No. ENV4-CT96-0361, 1999.

[193] B. Scarlett, End to End Scenario for Compressed SAR Imagery, Report of the Canadian Ice Service, 1999.

[194] B. Scheuchl, M. Grunes, R. Kwok, I. Cummins, Automated Sea Ice Classification Using Space-borne Polarimetric SAR Data, Proc. IEEE International Geoscience and Remote Sensing Symposium (IGARSS'01), pp. 3117–3119, 2001.

[195] B. Scheuchl, I. Hajnsek, I. Cumming, Model Based Sea Ice Classification Using Polarimetric SAR Data, Proc. IEEE International Geoscience and Remote Sensing Symposium (IGARSS'02), 2002.

[196] B. Scheuchl, I. Hajnsek, I. Cumming, Sea Ice Classification Using Multi-Frequency Polarimetric SAR Data,Proc. IEEE International Geoscience and Remote Sensing Symposium (IGARSS'02), 2002.

[197] B. Scheuchl, I. G. Cumming, Potential of Radarsat-2 for Sea Ice Classification,, Proc. IEEE International Geoscience and Remote Sensing Symposium (IGARSS'02), 2002, pp. 2185–2187.

[198] B. Scheuchl, I Hajnsek, I. G. Cumming, Model-Based Classification of Polarimetric SAR Sea Ice Data, Proc. IEEE International Geoscience and Remote Sensing Symposium (IGARSS'02), 1521–1523, 2002.

[199] B. Scheuchl, D. Flett, R. Caves, I. G. Cumming, Potential of Radarsat-2 for Operational Sea Ice Monitoring, Canadian Journal of Remote Sensing, v. 30, n. 3, pp. 448–461, 2004.

[200] B. Scheuchl, R. Caves, D. Flett, R. De Abreu, M. Arkeet, I. G. Cumming, The potential of Cross-Polarization Information for Operational Sea Ice Monitoring, Proc. Envisat Symposium, Salzburg, Austria, 2004.

[201] B. Scheuchl, R. Caves, D. Flett, R. De Abreu, M. Arkeet, I. G. Cumming, Envisat ASAR Data for Operational Sea Ice Monitoring, Proc. IEEE International Geoscience and Remote Sensing Symposium (IGARSS'04), v. III, pp. 2142–2145, 2004.

[202] B. Scheuchl, I. G. Cumming, I. Hajnsek, Classification of Fully Polarimetric Single- and Dual-Frequency SAR Data of Sea Ice Using the Wishart Statistics, Canadian Journal of Remote Sensing, v. 31, n. 1, pp. 61–72, 2005.

[203] A. Seinä, H. Grönvall, S. Kalliosaari, J. Vainio, P. Eriksson, J.-E. Lundqvist, WMO Sea ICE Nomenclature: Terminology for the Baltic Sea in English, Finnish and Swedish, MERI Report n. 43, Finnish Institute of Marine Research, 2001.

[204] S. G. Servetto, K. Ramchandran, M. T. Orchard, Image coding based on a morphological representation of wavelet data, IEEE Trans. Image Proc. v. 8, n. 9, pp. 1161-1174, 1999.

[205] J. M. Shapiro, Embedded image coding using zerotrees of wavelet coefficients, IEEE Trans. Signal Processing, v. 41, n. 12, pp. 3445-3462, December 1993.

[206] M. E. Shokr, Evaluation of Second Order Texture Parameters for Sea Ice Classification from Radar Images, Journal of Geophysical Research, v. 96, n. C6, pp. 10625-10640, 1991.

[207] M. E Shokr, R. Jessup, B. Ramsay, An Interactive Algorithm for Derivation of Sea Ice Classifications and Concentrations from SAR Images, Canadian Journal of Remote Sensing, v. 25, n. 1, pp. 70-79, 1999.

[208] M. Simard, G. DeGrandi, K. P. B. Thomson, G. B. Benie, Analysis of speckle noise contribution on wavelet decomposition of SAR images, IEEE Trans. Geoscience and Remote Sensing, v. 36, n. 6, pp. 1953-1962, 1998.

[209] M. Similä, The Evaluation of Two Classification Algorithms to Discriminate Open Water and Sea Ice from SAR Image, Proc. 2nd WMO Operational Ice Remote Sensing Workshop, v. 1, pp. 89-103, 1991.

[210] M. Similä, SAR image segmentation by a two-scale contextual classifier, in Desachy, J. (ed.), Image and signal processing for remote sensing, Proc. SPIE v. 2315, pp. 434-443, 1994.

[211] M. Similä, J. Helminen, The Identification of the Deformed Sea Ice Fields from ERS-SAR Image by Wavelets, Proc. International Geoscience and Remote Sensing Symposium (IGARSS'95), v. II, pp. 868–870, 1995.

[212] M. Similä, SAR Image Classification According to the Ice Deformation, Proc. of the Second International Workshop on ERS Applications, London 1995, pp. 211–214, 1996.

[213] M. Similä, I. Heiler, M. Mäkynen, M. Hallikainen, Observations about the Discrimination properties of polarimetric SAR data over the Baltic Sea ice, SPIE Proceedings V. 3496, pp.150-165, 1998.

[214] M. Similä, J. Karvonen, Classification of First-Year Sea Ice Using Pulse-Coupled Neural Network, Information Processing for Remote Sensing, ed. C. H. Chen, World Scientific Publishing, 1999.

[215] M. Similä, E. Arjas, M. Mäkynen, M. Hallikainen, Bayesian classification model for sea ice roughness from scatterometer data, IEEE Trans. Geoscience and Remote Sensing v. 39, n. 7, pp. 1586-1595, 2001.

[216] M. Similä, I. Heiler, J. Karvonen, EMAC-95 Sea Ice Campaign, Final Report, internal report, Finnish Institute of Marine research, 2004.

[217] A. Skodras, C. Christopoulos, T. Ebrahimi, The JPEG 2000 Still Image Compression Standard, IEEE Signal Proc. Magazine, v. 18, n. 5, pp. 36-58, 2001.

[218] A. N. Skourikhine, L. Prasad, B. R. Schlei, Neural Network for Image Segmentation, Applications and Science of Neural Networks, Fuzzy Systems and Evolutionary Computation III, Proc. of SPIE, v. 4120, 2000.

[219] H. Skriver, Extraction of Sea Ice Parameters from Synthetic Aperture Radar Images, Lic. Thesis, Technical university of Denmark, 1989.

[220] D. M. Smith, E. C. Barrett, J. C.ăScott, Sea Ice Type Classification from ERS-1 SAR Data, Based on Grey Level and Texture Information, Polar Record, v. 31, n. 177, pp. 135-146, 1995.

[221] P. C. Smits, S. G. Dellepiane, Synthetic Aperture Radar Image Segmentation by a Detail Preserving Markov Random Field Approach, IEEE Trans. Geoscience and Remote Sensing, v. 35, n. 4, pp. 844-857, 1997.

[222] P. C. Smits, S. G. Dellepiane, Discontinuity-adaptive Markov Random Field Model for the Segmentation of Intensity SAR Images, IEEE Trans. Geoscience and Remote Sensing, v. 37, n. 1, pp. 627-631, 1999.

[223] L.-K. Soh, C. Tsatsoulis, Multisource Data and Knowledge Fusion for Intelligent SAR Sea Ice Classification, Proc. of the International Geoscience and Remote Sensing Symposium 1998 (IGARSS'98), v. I, pp. 68-70, 1998.

[224] ARKTOS: An Intelligent System for SAR Sea Ice Image Classification, IEEE Trans. Geoscience and Remote Sensing, v. 42, n. 1, pp. 229-248, 2004.

[225] K. Steffen, J. Heinrichs, Feasibility of Sea Ice Typing with Synthetic Aperture Radar (SAR) Merging of Landsat Thematic Mapper and ERS 1 SAR Satellite Imagery, Journal of Geophysical Research, v. 99, n. C11, pp. 22413-22424, 1994.

[226] Y. Sun, A. Carlstrom, J.Askne, SAR image classification of ice in the gulf of Bothnia, Int. Journal of Remote Sensing, v. 13, n. 13, pp. 2489-2514, 1992.

[227] Y. Sun, SAR Remote Sensing of Sea Ice : Towards Automatic Extraction of Geophysical Information, DR. Tech dissertation, Chalmers University of Technology, Sweden, Technical Report n. 275, 1995.

[228] C. T. Swift, D. J. Cavalieri, Passive microwave remote sensing for sea ice research. EOS. v. 66 n. 49, pp. 1210-1212, 1985.

[229] P.N. Topiwala (ed.), Wavelet Image and Video Compression, Kluwer Academic Publishers, 1998.

[230] S. Tjuatja, A. K. Fung, J. Bredow, Scattering Model for Snow-Covered Sea Ice, IEEE Trans. Geoscience and Remote Sensing, v. 30, n. 4, pp. 804-810, 1992.

[231] F.T. Ulaby, R. K. Moore, A. K. Fung, Microwave Remote Sensing, Active and Passive, v. I : Microwave Remote Sensing Fundamentals and Radiometry, Addison-Wesley, 1981.

[232] F.T. Ulaby, R. K. Moore, A. K. Fung, Microwave Remote Sensing, Active and Passive, v. II : Radar Remote Sensing and Surface Scattering and Emission Theory, Addison-Wesley, 1982.

[233] F. T. Ulaby, R. K. Moore, and A. K. Fung, Microwave Remote Sensing, V. III. Norwood, MA: Artech House, 1986.

[234] F. T. Ulaby, C. Elachi (ed.), Radar Polarimetry for Geoscience Applications, Artech House, 1990.

[235] F. T. Ulaby, D. Held, M. C. Dobson, K. C. McDonald, T. B. Senior., Relating Polarization Phase Difference of SAR Signals to Scene Properties, IEEE Trans. Geoscience and Remote Sensing, v. GE-25, n. 1, pp. 83-92, 1987.

[236] L. M. H. Ulander (ed.), Baltic Experiment for ERS-1, Research Report n. 51, Winter Navigation Research Board, Sweden, 1994.

[237] L. M. H. Ulander, A. Carlström, J. Askne, Effect of the frost flowers, Rough Saline Snow, and Slush on the ERS-1 SAR Backscatter, Int. Journal of Remote Sensing, v. 16, n. 17, pp. 3287-3306, 1995.

[238] J. Vainio, H. Grönvall, Operational Use of Radarsat SAR Data in the Baltic Sea During the Winter 1997/98, Proc. POAC'99, v. 1, pp 166-171, 1999.

[239] J. Vainio, M. Similä, H. Grönvall, Operational Use of Radarsat SAR Data as Aid to Winter Navigation in the Baltic Sea, Canadian Journal of Remote Sensing, v. 26, n 4, pp 314-317, 2000.

[240] J. Vainio, A. Seinä, P. Backman, Sea Ice Nomenclature, English-Finnish-Swedish-Estonian-Russian, Finnish Maritime Administration, 2002.

[241] J. D. Villasenor, B. Belzer, J. Liao, Wavelet filter evaluation for image compression, IEEE Trans. Image Proc., v 4, n 8, pp 1053-1060, August, 1995.

[242] N. A. Weiss, Introductory Statistics, 7th ed., Addison-Wesley, 2005.

[243] T. A. Welch, A Technique for High-Performance Data Compression, IEEE Computer, v. 17 n. 6, pp. 8-19, 1984.

[244] S. A. Werness, S. C. Wei, and R. Carpinella, Experiments with wavelets for compression of SAR data, IEEE Trans. Geoscience and Remote Sensing, v. 32, n. 1, pp. 197-201, 1994.

[245] R. G. White, Change Detection in SAR Imagery, Int. J. Remote Sensing, v. 12, pp. 339-360, 1991.

[246] I. H. Witten, R.M. Neal, J. G. Cleary, Arithmetic coding for data compression, Comm. of the ACM, v. 30, n. 6, pp. 520-540, June 1987.

[247] Y. Yu, S. T. Acton, Speckle Reducing Anisotropic Diffusion, IEEE Trans. Image Processing, v. 11, n. 11, pp. 1260-1270, 2002.

[248] B. Yue, SAR Sea Ice Recognition Using Texture Methods, M. Sc Thesis, University of Waterloo, Ontario, Canada, 2002.

[249] J. Ziv, A. Lempel, A Universal Algorithm for Sequential Data Compression, IEEE Trans. Information Theory, v. IT-23, n. 3, pp. 337-343, 1977.

[250] Z. Zeng and I. G. Cumming, SAR image data compression using a tree-structured wavelet transform, IEEE Trans. Geoscience and Remote Sensing, v. 39, n. 3, pp. 546-552, 2001.